Dissertation
submitted to the
Combined Faculty of Mathematics, Engineering and Natural Sciences
of Heidelberg University, Germany
for the degree of
Doctor of Natural Sciences

Put forward by
Philipp Maximilian Lunt
Born in: Tübingen
Oral examination: 03.07.2024

Rotating few-fermion systems

Referees: Prof. Dr. Selim Jochim
Prof. Dr. Markus Oberthaler

Abstract

This thesis reports on the first realization of a two-particle Laughlin state – the quintessential building block of fractional quantum Hall states – in a rotating ultracold quantum gas. Utilizing a single atom and spin resolved imaging technique, we probe the Laughlin wavefunction and reveal its microscopic signatures: the suppression of interparticle interactions by incorporating angular momentum into the particles' relative motion.

In order to rotate few-fermion systems we develop a novel all-optical approach based on the interference of the optical trapping potential of the atoms with Laguerre-Gaussian beams. Since this method requires high quality optical light fields, we implement an advanced optical phase aberration correction technique by using the quantum gas itself as the wavefront sensor. We verify the imprint of the angular momentum from the rotating trap onto the atoms by transferring a single atom in an angular momentum eigenstate of the harmonic potential. To realize a Laughlin state, we prepare two repulsively interacting, spinful fermions in the ground state of the tweezer and subsequently turn on the trap rotation which coherently populates a state with angular momentum in the atoms' relative motion. We identify the state as the Laughlin state based on the reconstructed density distribution and the second-order correlation functions.

This work establishes the foundation for assembling bosonic and fermionic fractional quantum Hall states in rotating atomic gases.

Zusammenfassung

Im Rahmen dieser Arbeit wurde ein aus zwei Teilchen bestehender Laughlin Zustand – der essentielle Grundbaustein fraktionaler Quanten-Hall-Zustände – in einem rotierenden ultrakalten Quantengas realisiert. Unter Verwendung einer atom- und spinaufgelösten Abbildungsmethode, wurden die mikroskopischen Signaturen der Laughlin Wellenfunktion beobachtet: die Unterdrückung der Wechselwirkung durch die Aufnahme des Drehimpulses in der Relativbewegung der Teilchen.

Um Systeme mit wenigen Fermionen zu rotieren, entwickeln wir einen neuen, rein optischen Ansatz, der auf der Interferenz des optischen Potentials der Atome und Laguerre-Gaußscher Strahlen basiert. Da für diese Methode qualitativ hochwertige optische Strahlen notwendig sind, implementieren wir eine progressive Technik zur Korrektur der optischen Phasenaberration, indem wir das Quantengas selbst als Wellenfrontsensor verwenden. Wir verifizieren die Aufnahme des Drehimpulses von der rotierenden Falle auf die Atome, indem wir ein einzelnes Atom in Drehimpulseigenzustände des harmonischen Potentials transferieren. Um einen Laughlin-Zustand zu realisieren, präparieren wir zwei stark abstoßend wechselwirkende, spinbehafteten Fermionen im Grundzustand der Falle, um anschließend die Falle zu rotieren, wodurch wir kohärent einen Zustand populieren, welcher Drehimpuls in der Relativbewegung der Atome besitzt. Wir identifizieren den Zustand als Laughlin-Zustand, basierend auf der rekonstruierten Dichteverteilung und der zweiten Ordnung Korrelationsfunktionen.

Diese Experimente schaffen die Grundlage für die Zusammensetzung bosonischer und fermionischer fraktionaler Quanten-Hall-Zustände in rotierenden atomaren Quantengasen.

Acknowledgements

Writing a thesis demands a rather dense and concise language, always prioritizing the precise transfer of the content. In this preface, I now have the chance to describe the Odyssey of my thesis in a more poetic manner. Fortunately, my journey wasn't as long as that of Homers' protagonist. However, it might have taken forever and a day if I hadn't received the support from numerous inspiring people, with an infectious excitement on an endless list of topics.

Selim, thank you for your trust and your generosity. Your enthusiasm was always a great motivator to keep exploring into the (yet) unknown. I could not have asked for more.

Philipp Preiss, certainly without your original ideas on the rotating few-fermion systems, I would not have become that interested in the topic. I appreciate your courage for suggesting to try something novel – there is no reward without risk.

I had the chance to still enjoy some overlap with the "old" generation of the group, in particular Jan Hendrik Becher, Ralf Klemt, Luca Bayha, Keerthan Subramanian, and Marvin Holten.

In particular Marvin, your LabView knowledge remains impressive to me to this day, and it is crazy that you basically wrote the experimental control for the entire group. I would also like to mention our shared love for Techno, to the (let's call it) amusement of our roommates during last years DPG conference, who were certainly enjoying our music taste as well.

To the people from the *Old* experiment, it was a great pleasure to share the office with bright minds like you, where one can ask a seemingly random question into the room and you end up discussing for an hour.

Paul, It may sound like an oxymoron, but selfishly, I do consider you my *in-lab theorist*. One of the most valuable aspects in the lab are that the different skills interfere constructively to maximize productivity. I've always felt that we made a good team. I learned from you during the work on the optical aberration corrections that at the end of the day "you don't catch atoms with pretty traps, you trap atoms with light." On that regard, I would add that atoms need to be trapped gently, but firmly. One thing I must correct you on, though, is that you (misleadingly) suggest that the only book I've ever read is "The Process." I might have read one or two more.

Maciej, once you started as a PostDoc in our group, you infused it with a fresh sense of energy. I learned from you that ultimately the atoms decide whether something is engineered well or not. That was very valuable lesson for the motional control of the angular momentum states. One of the most thrilling experiences during my PhD was when you, Paul and I were looking at the data of the Laughlin state (which was yet unclear at that time). Initially, we were unsure whether there was a mistake in the evaluation of the data, but the theory was not matching. At some point, we realized that we have to include a factor of $\sqrt{2}$ in the theory. Upon re-plotting the theory curve, we all burst into laughter, when seeing that the theory curve and the experimental data coincided perfectly. Sharing this excitement in that moment made it even more valuable.

Johannes, your sharp eye to the details and sense for consistency is an invaluable skill. I admire your critical thinking and your determination to drive progress in the lab. You shocked me not only once where your quick response to the alarm of the fire brigade caught me by surprise, as you jumped off and disappeared within seconds.

Daniel, I admire your willpower in completing the installation of the objective mount into the experiment, even during late hours. Sometimes, it is impossible to stop and one has to push through until the task is done.

Jonas, I am happy that you came back to do your master thesis on the experiment, you are certainly an enrichment to the team. I still have the cup with a printed $\varphi-$symbol on it, which you gave me after your Bachelor thesis. My black tea tastes even better in that one!

Thanks to the people from the *New* experiment, Sandra and Carl, with whom I worked on the *elliptic flow* project, it was a real pleasure to be involved in these measurements as well.

Sandra, presenting together the emergence of collective behaviour in a church to a broad audience was certainly a once-in-a-lifetime experience, made even more valuable by sharing it with you. I also need to mention the countless bouldering sessions, which often included beer and pizza afterwards. These sessions were valuable not only for staying active during the PhD, but also for providing a fun environment to discuss the status of the experiment and random ideas that came to mind when falling off the wall.

Carl, even though your billiard club is right next to the Boulder gym, we never managed to grab a beer afterwards. That might be a good resolution to make for the future.

Tobi, sharing a room (and a double bed) at the DPG conferences was hilarious, though endlessly reciting scenes from Lord of the Rings certainly didn't help me falling asleep. Even though my consumption of coke increased rapidly and beyond a healthy level (is there even a healthy level of coke consumption?) at the final stage of my PhD, I cannot even compete with your consumption of *Schwip Schwap*. The list of quotations I started to collect from you grows larger everyday, and makes me laugh clangorously every time I look at them. One which I find funny and true at the same time is: "I don't want to live in a world with crooked breadboards".

Max, our success with the team *ABC Tag des offenen Tores II* would not have been possible without the football shoes you generously provided me. The fact that I had to use tape to hold them together for the last game either tells me that I should stop playing or to get some new shoes myself.

Johanna, your inclusion in the *bouldering team* has been a great addition. While I might have a biased opinion on that topic, it is clear that you should prioritize bouldering over your other sports activities and join more often.

Lauriane Chomaz, I must highlight your french cheese recommendations and the privilege to taste your delicious self-made baguette. Thanks as well for the (slightly) embarrassing e-mails from you, that point out that there is free food somewhere at the institute – even though I still go there to grab a bite. Obviously, I also have to mention the bouldering and climbing sessions that helped me to free the mind from the lab and to think about solving another problem on the wall. I am grateful for the advice and support in times when I truly needed it.

Nathan Goldman, there is no other physicist who sparks my excitement more on topologically ordered phases of matter and at the same time about (as of yet) undiscovered musicians and their concerts. Thank you for these lively and inspiring discussions. Now that I have some free time again, I must pay a visit to a few concerts.

On the subject of this thesis, I thank Markus Oberthaler for accepting to be the second referee, as well as Richard Schmidt, and José R. Crespo López-Urrutia to be part of my committee. Furthermore, I am indebted to the people who have helped increasing the quality of this work by proof reading the chapters, in particular Paul, Maciej, Johannes, Sandra, and Marvin.

Meine Eltern Martin und Anastassia und meine Geschwister, Alex, Lennart und Elena, nur durch Eure bedingungslose Unterstützung habe ich es bis hierhin schaffen können.

Loui, mit den letzten und kostbarsten Worten dieser Danksagung, widme ich Dir all meine Dankbakeit.

"Oh jungle, behold the fate of all who lose themselves in your vortex!"
– José Eustasio Rivera, *The Vortex* (1924)

Contents

1

Introduction

Structures emerge in nature, and physics classifies them into phases of matter. This organizing principle manifests in the universal properties exhibited by distinct systems that are in the same phase, irrespective of their specific constituents. These properties are emergent as they cannot be constructed from a first principle microscopic description, and are instead defined by the collective behaviour of the entire ensemble [And72; Lau00]. A phase transition between two different phases is then associated with a qualitative change in their emergent, macroscopic properties.

Many phases in condensed matter systems can be classified by their symmetries [Lan36; Lan37; Gol62; Sac11], a concept introduced by Landau, which describes phase transitions based on *spontaneous symmetry breaking*. The ground state of the system is labelled *disordered* if it possesses the same symmetries as the system, while a phase transition occurs when the ground state breaks the symmetry of the system, referred to as the *ordered* state. A phenomenological description of phase transitions was derived by Ginzburg and Landau [Gin50], where an order parameter describes the phase transition. In the disordered phase, the order parameter vanishes, while it emerges in the symmetry-broken phase, signalling the onset of a phase transition. Such a transition can be invoked by thermal fluctuations where the temperature of the system is changed and is associated with a classical phase transition. On the other hand, a quantum phase transition, e.g. the superfluid to Mott-insulator transition [Jak98; Gre02], occurs at zero temperature and is driven by quantum fluctuations, rather than thermal fluctuations [Sac11]. However, these are still successfully described by the emergence of an order parameter.

There is yet another class of quantum phase transitions which preserve their symmetries, and therefore cannot be described by Landau's theory of spontaneously broken symmetries. The new ingredient is *topological order* [Hal17; Wen95; Che10]. Topological phases of matter are instead classified by a global invariant that is robust with respect to smooth deformations. More precisely, two states of a Hamiltonian with a gapped energy spectrum, that can be adiabatically deformed into each other by a local unitary transformation belong to the same topological phase. If the gap is not preserved during that process, the system undergoes a topological quantum phase transition [Has10; Qi11]. While topological phases of matter are found across numerous physical systems, including quantum spin liquids [Sac08; Bal10], photonic systems [Lu16], ultracold quantum gases [Gol16], mechanical systems [Hub16] or topological insulators [Has10; Qi11], the field came into existence with the topological interpretation [Tho82] of the quantum Hall effect [Kli80; Gir89].

The defining property of the quantum Hall effect is its quantization of the Hall conductance to integer values of e^2/h [Kli80], which originate from dissipationless, current carrying states at the boundary and insulating states in the bulk region [Hal82; Has10]. The quantum Hall states can be understood as topological phases since the number of states at the boundary can be related to a topological invariant, the so-called Chern number [Tho82; Gol16]. Hence, the quantized conductivity, a macroscopic property, is independent of the microscopic structure of the material and in particular, robust against minor deformations such as a change in the magnetic field.

A few years after the discovery of the integer quantum Hall (IQH) effect, fractional values of the Hall conductance e^2/h were also observed [Tsu82]. Such systems host quasiparticles that are fractionalized at the boundary [Wen95] and exhibit fractional exchange statistics within the bulk [Ste08]. Unlike the IQH effect, where the energy gap of the Hamiltonian stems from the single particle cyclotron frequency, the gap in the fractional quantum Hall (FQH) effect arises from an inherent many-body problem of strongly interacting electrons [Lau83]. As these systems are typically hard to simulate numerically, realizing them in synthetic materials, which offer observables that are hard to access in conventional solid state materials, could provide a deeper understanding of their microscopic origins [Gol16; Coo19; Ma24].

Ultracold atoms in rotating traps

Ultracold atoms are an excellent platform for the simulation of complex quantum-many-body systems, which offer high degree of control and tunability with respect to the temperature, the inter-particle interactions, the density, or the geometry and dimensionality of the potential landscape [Blo08; Blo12; Nav21; Gro21a; Wei21]. They provide a variety of observables to study their properties, ranging from spectroscopic probes [Val21], spatially resolved thermometry [Yan24], or correlation measurements by detecting single atoms in real and momentum space [Alt04; Gro21a; Hol21; Bra23]. In order to simulate electrons subjected to magnetic fields, neutral atoms require engineering of an artificial magnetic field due to their charge neutrality [Dal16]. Among the various approaches in Floquet engineered optical lattices [Jot14; Aid14] and spin-orbit coupled atomic gases [Lin09] in synthetic dimensions [Stu15; Man15], the most intuitive one, on a conceptual level, is to rotate the system [Fet03; Coo08]. Here, in the classical picture, the artificial magnetic field is introduced by exploiting the analogy between the Lorentz force and the Coriolis force.

The most direct manifestation of this equivalence in the context of rotating ultracold atomic gases, is the nucleation of quantized vortices [Mad00; Hod01] which form an Abrikosov lattice with increasing vortex number [Abo01; Zwi05], analogous to type-II superconductors exposed to a magnetic field [Til19]. When the number of vortices reaches the number of particles, however, the system undergoes a phase transition driven by quantum fluctuations of the vortices to a strongly correlated state [Coo01; Sin02; Bay04]. In a system of repulsively interacting bosons, a transition to a Laughlin state occurs [Wil98; Wil00; Coo08; Coo20], which is a paradigmatic example of the FQH effect [Lau83]. First signatures of entering the quantum Hall regime have been observed in the rapidly rotating limit, by the softening of the Abrikosov lattice [Bre04; Sch04], the suppression of photoassociation loss [Gem10], and more recently by geometrically squeezing a Bose-Einstein condensate into the LLL [Fle21; Muk22].

From an experimental point of view, reaching the strongly interacting limit is challenging since trap imperfections may cause heating of the system and the exceedingly small energy gaps render the stability of the FQH state delicate. In particular, rapidly rotating fermionic systems remain experimentally unexplored so far, primarily due to the necessity to use rotating optical potentials which often suffer from optical aberrations. Moreover, challenges arise in transferring all fermions from the non-rotating ground state into the LLL, given the Pauli principle.

In this thesis, we choose a bottom-up approach to realize a Laughlin state in a rapidly rotating optical potential comprised of two fermionic atoms, the fundamental building block of a FQH state. Our fluorescence imaging technique allows us to resolve each individual atom, thereby unveiling the microscopic structures of the strongly correlated Laughlin wavefunction. In this way, we demonstrate key properties of a Laughlin state, including the suppression of interactions due to the incorporation of angular momentum in the particles' relative motion. This establishes the foundation for future studies on strongly correlated topological phases of matter with rotating ultracold quantum gases.

Outline of this thesis

In *chapter 2*, we present the theoretical framework for the main experimental results in this thesis. We give a concise (and non-exhaustive) overview on the quantum Hall effect and its relevant connections to this work. In particular, we motivate the analogy of rapidly rotating atomic gases and FQH systems.

Chapter 3 contains a description of the interactions of neutral atoms at ultracold temperatures. Furthermore, we introduce the concept of Feshbach resonances which allows to tune the interactions of the atoms from attractive to non-interacting and to repulsive. Chapter 4 highlights the experimental apparatus to cool and trap neutral atoms in optical potentials, with control on the single particle level. We showcase a generic optical phase aberration correction scheme by directly using the quantum gas itself. Furthermore, we describe our optical setup to set a tightly focused optical tweezer in rotation by interference with a Laguerre-Gaussian mode. In the last section of this chapter, we describe the imaging techniques in our experiment to extract the single atom and spin resolved momenta of individual atoms which allows us to detect correlations of the quantum state.

In *chapter 5*, we study the motional control of a single fermion which we engineer into various angular momentum eigenstates of the harmonic trapping potential. We confirm the imprint of angular momentum by investigating the time evolution of the angular momentum state in a slightly deformed, anisotropic trap. In *chapter 6*, we realize a Laughlin state with two rapidly rotating spinful fermions. Our single atom and spin resolved fluorescence imaging allows us to sample from the Laughlin wavefunction and to reconstruct the two-dimensional density of the wavefunction. Furthermore, the imaging technique enables us to determine the pair and angle correlations of the two particles. *Chapter 7* summarizes the results of this thesis and gives a taste of the possibilities of future studies.

List of publications

Most of the results presented in this thesis can be found in the following references:

- *Realization of a Laughlin state of two rapidly rotating fermions*
  Philipp Lunt, Paul Hill, Johannes Reiter, Philipp Preiss, Maciej Gałka, Selim Jochim
  arXiv: 2402.14814 (2024)

- *Optical Phase Aberration Correction with an Ultracold Quantum Gas*
  Paul Hill, **Philipp Lunt**, Johannes Reiter, Maciej Galka, Philipp Preiss, Selim Jochim
  arXiv: 2404.16827 (2024)

The following references are not covered:

- *Observation of Cooper Pairs in a Mesoscopic 2D Fermi Gas*
  Marvin Holten, Luca Bayha, Keerthan Subramanian, Sandra Brandstetter, Carl Heintze, **Philipp Lunt**, Philipp M. Preiss, Selim Jochim
  doi: 10.1038/s41586-022-04678-1, arXiv: 2109.11511 (2022)

- *Emergent hydrodynamic behaviour of few strongly interacting fermions*
  Sandra Brandstetter*, **Philipp Lunt***, Carl Heintze, Giuliano Giacalone, Lars H. Heyen, Maciej Gałka, Keerthan Subramanian, Marvin Holten, Philipp M. Preiss, Stefan Floerchinger, Selim Jochim
  arXiv: 2308.09699 (2023)

2

The quantum Hall effect

The ground breaking discovery of the quantum Hall effect in 1980 [Kli80] has led to findings of completely novel phenomena in condensed matter physics [Kön07; Yu10; Ser20; McI19; Lee09; Tan19] and even beyond that field, such as the redefinition of the SI unit system. The precise quantization of the Hall resistance defined by two fundamental constants, the Planck constant and the elementary charge, underscores the astonishing robustness of this macroscopic quantum phenomenon in semiconductor samples that contain uncontrolled material impurities or imprecise geometries.

The discovery of the fractional quantum Hall effect (FQH), that is the quantization of the Hall resistance to fractional values, avalanched a variety of theoretical developments as it required a complete new rethinking of strongly correlated many-electron systems [Lau83; Hal83a; Hal84; Gir84; Mac85; Lee89; Jai89]. Laughlin's radical idea to propose a variational ground states wavefunction which describes an incompressible quantum fluid with excitations that are of fractional elementary charge [Lau83] turned out to describe the effect accurately and is until to date the cornerstone of many of these developments.

In this chapter, we intend to give a short introduction to the classical Hall effect and the integer quantum Hall (IQH) effect to introduce the mathematical notation, and to discuss the fundamental differences to the FQH effect. In the last section 2.4, we establish an analogy between electron systems in magnetic fields and ultracold neutral atoms in rotating potentials, which are used in this thesis to simulate FQH states. This chapter is based on books [Yos98; Gir89; Wen04; Coo20; Dal16], lectures notes [Ton16; Mac94] and reviews [Coo08; Pap22] on the quantum Hall effect, where we refer to a more in-depth treatment.

2.1 Classical Hall effect

Consider the motion of electrons with mass m_e and charge $-e$ restricted to a two-dimensional (2D) horizontal plane and exposed to an external magnetic field $\boldsymbol{B}$ along

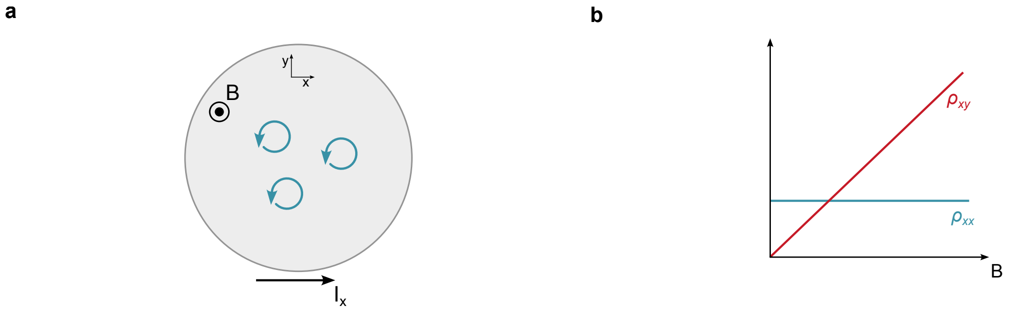

Figure 2.1: Classical Hall effect. **a**, Electrons confined to the horizontal xy-plane, slowly moving along the longitudinal x-direction, and subjected to an axial magnetic field B, undergo cyclotron motion, illustrated by the blue arrows. **b**, Resistivity along the longitudinal (blue) and transverse (red) direction.

the axial direction, illustrated in Fig. 2.1. Due to the Lorentz force the motion of the electrons obey cyclotron orbits with a frequency $\omega_\mathrm{B} = eB/m_\mathrm{e}$, which introduces a natural length scale, the magnetic length $l_\mathrm{B} = \sqrt{\hbar/m_\mathrm{e}\omega_\mathrm{B}}$, associated to the radius of the orbits.

A classical description of the electron transport in a metal is given by the Drude model [Dru00] that describes the electron velocity $\boldsymbol{v}$ accelerated by an electric field $\boldsymbol{E}$ along the $x-$direction, with a friction term to account for scattering of the electrons with underlying lattice or other electrons on a characteristic time scale τ. The equation of motion then reads

$$m\frac{\mathrm{d}\boldsymbol{v}}{\mathrm{d}t} = -e\boldsymbol{E} - e\boldsymbol{v} \times \boldsymbol{B} - \frac{m\boldsymbol{v}}{\tau}. \tag{2.1}$$

We would like to find the equilibrium solution $\mathrm{d}\boldsymbol{v}/\mathrm{d}t = 0$ and relate it to the current density $\boldsymbol{j} = ne\boldsymbol{v}$, here n is the electron density. Solving Eq. (2.1) in the 2D plane then relates the current density to the electric field by

$$\boldsymbol{j} = \frac{\sigma_\mathrm{DC}}{1+\omega_\mathrm{B}^2\tau^2}\begin{pmatrix} 1 & -\omega_\mathrm{B}\tau \\ \omega_\mathrm{B}\tau & 1 \end{pmatrix}\boldsymbol{E}, = \underline{\underline{\sigma}}\boldsymbol{E} \tag{2.2}$$

where $\sigma_\mathrm{DC} = ne^2\tau/m_\mathrm{e}$ is the DC conductivity in the absence of the magnetic field. This relation is known as *Ohm's law* as it relates the response of the current to an electric field via the conductivity $\underline{\underline{\sigma}}$. The off-diagonal terms in $\underline{\underline{\sigma}}$ cause a voltage perpendicular to the current direction, know as the Hall voltage [Hal79].

The resistivity $\underline{\underline{\rho}}$ is found by inverting the conductivity $\underline{\underline{\sigma}}$ which yields

$$\underline{\underline{\rho}} = \frac{1}{\sigma_{\mathrm{DC}}} \begin{pmatrix} 1 & \omega_{\mathrm{B}}\tau \\ -\omega_{\mathrm{B}}\tau & 1 \end{pmatrix} . \tag{2.3}$$

Remarkably, the off-diagonal term $\rho_{xy} = \omega_{\mathrm{B}}\tau/\sigma_{\mathrm{DC}} = B/ne$ depends only on the electron density and the electron charge, and is independent of the materials imperfections captured by the scattering time τ. In contrast, the resistivity along the longitudinal direction $\rho_{xx} = m_{\mathrm{e}}/ne^2\tau$ depends on τ and converges towards zero as the scattering time increases. The classical prediction of the resistivity based on the Drude model is illustrated in Fig. 2.1b, where ρ is displayed in arbitrary units. Having the classical expectation on the behaviour of the resistivity, we might wonder how they change under extreme conditions, that is at low temperatures and strong magnetic fields where quantum effects start to play the dominant role.

2.2 Integer quantum Hall effect

The IQH describes the quantization of the Hall resistivity at high magnetic fields to an extraordinary accuracy in terms of two fundamental constants

$$\rho_{xy} = \frac{h}{e^2\nu}, \ \nu \in \mathbb{Z} \tag{2.4}$$

the Planck constant h and the elementary charge e. The quantization of the Hall resistivity is accompanied with a vanishing longitudinal resistivity ρ_{xx}, displayed in Fig. 2.2. On the other hand, at low magnetic fields the classical expectation is recovered where ρ_{xy} increases linearly with the magnetic field and ρ_{xx} is approximately constant.

2.2.1 Landau levels

The IQH can be understood by considering non-interacting electrons in two dimensions $\boldsymbol{x} = (x, y)$ exposed to a magnetic field $\boldsymbol{B} = B\hat{\boldsymbol{e}}_{\mathrm{z}}$ along the axial direction. Since the electrons are non-interacting, the discussion can be simplified to a single electron, for which the Hamiltonian reads

$$\mathcal{H} = \frac{1}{2m_{\mathrm{e}}} \left(\boldsymbol{p} + e\boldsymbol{A}\right)^2 , \tag{2.5}$$

where $\boldsymbol{p} = (p_{\mathrm{x}}, p_{\mathrm{y}})$ is the canonical momentum and the vector potential $\boldsymbol{A}$ determines the magnetic field $\boldsymbol{B} = \nabla \times \boldsymbol{A}$. For a given magnetic field the choice of the vector potential is not unique as it stays the same under a gauge transformation $\boldsymbol{A} \rightarrow \boldsymbol{A} + \nabla\chi(\boldsymbol{r})$,

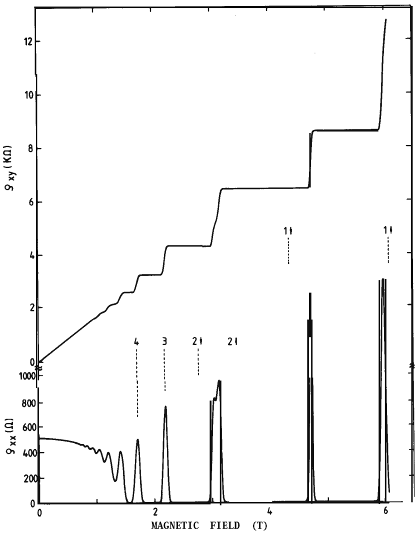

Figure 2.2: Integer quantum Hall effect. The IQH effect manifests in the quantization of the Hall resistivity ρ_{xy} with integer values accompanied with a drop in the longitudinal resistivity ρ_{xx} at strong magnetic fields and low temperatues. Taken from [Kli93].

where $\chi(\boldsymbol{r})$ is a scalar field[1]. We directly choose to work in the symmetric gauge $\boldsymbol{A} = (-By/2, Bx/2, 0)$ which preserves rotation symmetry about the origin. Let us remark that this is a natural choice in the underlying context of rotating systems as the angular momentum remains a good quantum number in both cases (more details in section 2.4).

In order to calculate the eigenergies of the Hamiltonian, we introduce new operators associated with the kinetic momentum and guiding center coordinates [Yos98; Mac94]

$$\boldsymbol{\pi} = \left(p_{\mathrm{x}} - \frac{\hbar}{2 l_{\mathrm{B}}^2} y, p_{\mathrm{y}} + \frac{\hbar}{2 l_{\mathrm{B}}^2} x \right), \tag{2.6a}$$

$$\boldsymbol{\rho} = \left(\frac{x}{2} - \frac{l_{\mathrm{B}}^2}{\hbar} p_{\mathrm{y}}, \frac{y}{2} + \frac{l_{\mathrm{B}}^2}{\hbar} p_{\mathrm{x}} \right), \tag{2.6b}$$

---

[1] The rotation of the divergence of a scalar field is zero $\nabla \times \nabla \chi(\boldsymbol{r}) = 0$

respectively, which obey the commutation relations

$$[\pi_{\mathrm{x}}, \pi_{\mathrm{y}}] = -i\hbar^2/l_{\mathrm{B}}^2, \tag{2.7a}$$

$$[\rho_{\mathrm{x}}, \rho_{\mathrm{y}}] = i l_{\mathrm{B}}^2, \tag{2.7b}$$

$$[\rho_{\mathrm{i}}, \pi_{\mathrm{j}}] = 0, \tag{2.7c}$$

where we used the known commutation relation for the canonical coordinates $[\boldsymbol{x}_{\mathrm{i}}, \boldsymbol{p}_{\mathrm{j}}] = i\hbar\delta_{\mathrm{ij}}$. From these commutation relations, we see that both the components of $\boldsymbol{\pi}$ and $\boldsymbol{\rho}$ are canonical conjugate variables, in which the magnetic length l_{B} appears as a natural length scale. Furthermore, the guiding center $\boldsymbol{\rho}$ can be interpreted as the center position of the cyclotron orbits. As they commute with the Hamiltonian (see Eq.(2.7c)) we expect that the energy states are degenerate. To put this in a physical picture, it doesn't cost any energy to shift the position of the guiding center. The only relevant energy scale is the kinetic energy given by the fast rotating cyclotron frequency.

The Hamiltonian can be expressed in a rather simple form consisting of the sum of π_{x}^2 and π_{y}^2, which has the same structure as the one-dimensional harmonic oscillator. Introducing the ladder operators

$$a = \frac{l_{\mathrm{B}}}{\sqrt{2}\hbar}\left(\pi_{\mathrm{x}} - i\pi_{\mathrm{y}}\right), \tag{2.8a}$$

$$a^\dagger = \frac{l_{\mathrm{B}}}{\sqrt{2}\hbar}\left(\pi_{\mathrm{x}} + i\pi_{\mathrm{y}}\right), \tag{2.8b}$$

which obey the commutation relation $[a, a^\dagger] = 1$ allows us to rewrite the Hamiltonian into the familiar structure

$$\mathcal{H} = \hbar\omega_{\mathrm{B}}\left(a^\dagger a + \frac{1}{2}\right). \tag{2.9}$$

This yields equally spaced eigenergies $E = \hbar\omega_{\mathrm{B}}(n + 1/2)$ which are called *Landau levels* and are separated by the cyclotron frequency ω_{B} proportional to the magnetic field, shown in Fig. 2.3a.

From the commutation relation of the guiding center coordinates we can estimate the number of degenerate states per Landau level, as a single state occupies an area $2\pi l_{\mathrm{B}}^2$. If we consider a disk with radius R and thus an area πR^2, the number of available states within the disk is therefore $\mathcal{N} = R^2/2l_{\mathrm{B}}^2$ which corresponds to an enormous degeneracy as we compare the macroscopic size of the disk with the microscopic length scale of the cyclotron orbit. The total flux which penetrates the wavefunction of an electron is given by $2\pi l_{\mathrm{B}}^2 B = h/e \equiv \phi_0$ which is exactly the magnetic flux quantum. Hence, there is a single flux quantum available for each electron.

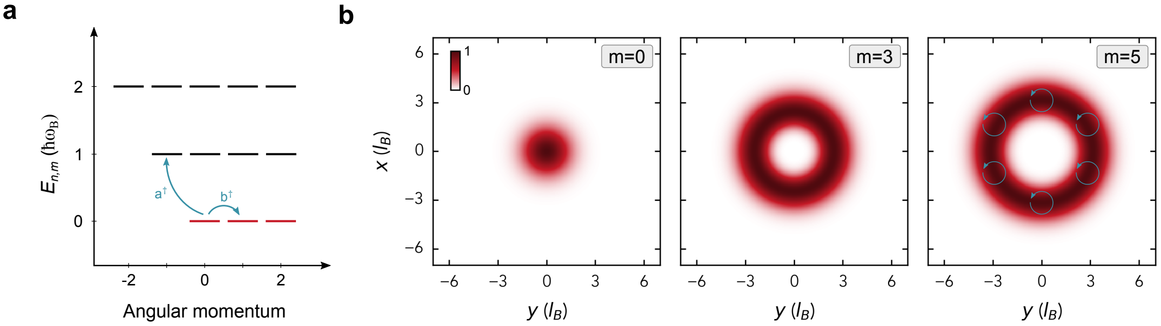

Figure 2.3: Landau levels. **a**, Degenerate Landau levels with respect to the angular momentum. Each Landau levels is separated equidistantly by the cyclotron frequency. The LLL $n = 0$ is highlighted in red. **b**, Probability density distributions of the single particle wavefunctions in the LLL for different angular momenta m. The radial extend grows with $\sqrt{2m}l_\mathrm{B}$. Non-zero angular momentum manifests in a node of the wavefunction at the origin $x = y = 0$. The circular arrows in the $m = 5$ case indicate the cyclotron orbits. Each density is normalized to 1.

In symmetric gauge, the angular momentum operator L_z distinguishes the states within each Landau level. To see this, let us express L_z in terms of the kinetic momentum and the guiding center coordinates by using Eq. (2.6a) and (2.6b). We arrive at

$$L_\mathrm{z} = xp_\mathrm{y} - yp_\mathrm{x} \tag{2.10}$$

$$= -\frac{\hbar}{2l_\mathrm{B}^2}(\rho_\mathrm{x}^2 + \rho_\mathrm{y}^2) + \frac{l_\mathrm{B}^2}{2\hbar}(\pi_\mathrm{x}^2 + \pi_\mathrm{y}^2). \tag{2.11}$$

The second term is associated with the kinetic energy (or equivalently the Hamiltonian), while the first term of L_z is again similar to the harmonic oscillator in terms of ρ_x, and ρ_y. Since L_z commutes with the Hamiltonian, it allows us to distinguish between states in a single Landau level. We introduce another set of creation and annihilation operators [Yos98; Mac94]

$$b = \frac{1}{\sqrt{2}l_\mathrm{B}}(\rho_\mathrm{x} + i\rho_\mathrm{y}) \tag{2.12a}$$

$$b^\dagger = \frac{1}{\sqrt{2}l_\mathrm{B}}(\rho_\mathrm{x} - i\rho_\mathrm{y}), \tag{2.12b}$$

which obey the commutation relation $[b, b^\dagger] = 1$. We can then express the angular momentum operator in terms of the ladder operators $L_\mathrm{z} = \hbar(a^\dagger a - b^\dagger b)$. The ladder operators $a^\dagger$ raises an energy state between Landau levels, while the application of $b^\dagger$ keeps the state in the same Landau level, but raises its angular momentum. This is illustrated in Fig. 2.3.

With that at hand, we can generally describe the state of an electron by the ket vector

$$|n, m\rangle = \frac{a^{\dagger n} b^{\dagger m}}{\sqrt{n! m!}} |0, 0\rangle \,, \tag{2.13}$$

where $|0, 0\rangle$ is the ground state which is annihilated to zero for both operators a, b and $n, m \geq 0$. These states are eigenstates of the operators $a^\dagger a$ and $b^\dagger b$, and in particular of the angular momentum operator $L_{\mathrm{z}} |n, m\rangle = (n - m)\hbar |n, m\rangle$. Here, the prefactor $(n-m)\hbar$ reflects the amount of orbital angular momentum incorporated by the electron.

To construct the wavefunctions in coordinate space we express the creation and annihilation operators in coordinate space $\boldsymbol{x}$. Therefore, we choose the complex coordinate[2] $z = x - iy$. The ground state wavefunction in coordinate space $\varphi_{0,0} \equiv \langle \boldsymbol{x} | 0, 0\rangle$ reads

$$\varphi_{0,0}(z) = \frac{1}{\sqrt{2\pi l_{\mathrm{B}}^2}} e^{-|z|^2/4l_{\mathrm{B}}^2}. \tag{2.14}$$

Of particular importance are the states in the lowest Landau level (LLL) which become most relevant in the FQH effect. These wavefunctions take the form

$$\varphi_{0,m}(z) = \frac{1}{\sqrt{2\pi 2^m m! l_{\mathrm{B}}^2}} \left(\frac{z}{l_{\mathrm{B}}}\right)^m e^{-|z|^2/4l_{\mathrm{B}}^2} \tag{2.15}$$

and are illustrated in Fig. 2.3b. States in the LLL consist of two parts, the trivial Gaussian contribution which take care that the the wavefunction converges to zero for large radii $|z| \to \infty$, and a polynomial of order m of the angular momentum causing a zero in the wavefunction at small radii $|z| \to 0$, given that $m > 0$. The maximum expectation value of the probability distribution $|\varphi_{0,m}(z)|^2$ is at a finite radius $\sqrt{2m} l_{\mathrm{B}}$ which does *not* correspond to the classical cyclotron orbit. In fact, the radius of the cyclotron orbit is still given by l_{B} in the LLL. Instead, the state $\varphi_{0,m}(z)$ can be understood as a linear combination of many cyclotron orbits with a radius l_{B}, see blue circular arrows in Fig. 2.3b with $m = 5$.

2.2.2 Robustness of the Hall plateaus

Having established the mathematical notation we come back to the question on the formation of the quantized plateaus of the resistivity. Here, we will concentrate on pro-

---

[2] This is in contrast to the usual mathematical expression $z = x + iy$ due to the direction of the magnetic field.

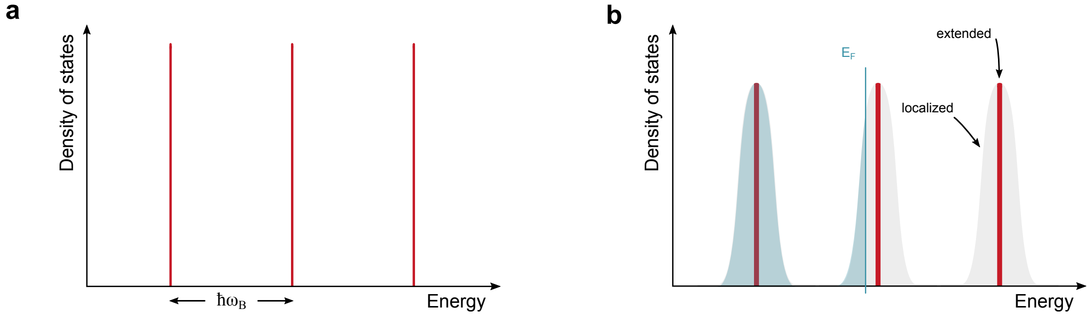

Figure 2.4: Landau levels with disorder. a, Landau levels without disorder are infinitely degenerate in a translational invariant system. **b,** Disorder lifts the degeneracy (broadening of Landau levels) and causes localization (in gray) of the extended (in red) states. Occupied extended and localized states up to the Fermi energy E_{F} are highlighted in blue.

viding a physical intuition of the origin of the IQH effect to underscore the fundamental distinctions from the fractional quantum Hall effect.

The role of impurities is crucial for the quantization of the Hall plateaus [Ton16]. This seems surprising in the first place as typically quantum mechanical effects are sensitive and tend to break down if subjected to disorder. However in the context of IQH effect, disorder is even necessary to exhibit broad plateaus of quantized resistivity. In the case of a pure, translationally invariant sample, the energy spectrum exhibits infinitely degenerate Landau levels equally spaced by the cyclotron frequency ω_{B}, illustrated in Fig. 2.4a. Disorder, which does not conserve any symmetry, lifts that degeneracy resulting in a broadening of the Landau levels, see Fig. 2.4b. However broadening alone does not explain the quantum Hall effect.

A second effect of disorder is the localization of states. Only extended states contribute to the conductivity of a material as they carry the charges throughout the sample. Localized states on the contrary are confined to a certain region of the material which undergo cyclotron motion around the impurities. Therefore, they do not contribute to the longitudinal conductivity.

The interplay of populating extended and localized states is the reason for the occurrence of the quantized Hall plateaus. Consider a fully filled Landau level at a certain magnetic field. Reducing the magnetic field leads to a decrease of available states per Landau level as the number of states scales with $\mathcal{N} \sim B$. Instead of populating the next higher Landau level, localized states are populated which do not contribute to the conductivity. Hence, the Hall conductance σ_{xy} remains constant, while the longitudinal conductivity σ_{xx} remains close to zero.

Finally, the origin of the stability of the IQH effect, that is the quantization of the Hall resistivity $\rho_{xy} = h/e^2\nu$ at fully occupied Landau levels, stems from the energy gap to the next higher lying Landau level given by the large cyclotron frequency $\hbar\omega_{\mathrm{B}}$. This is valid as long the temperatures are low enough $k_{\mathrm{B}}T \ll \hbar\omega_{\mathrm{B}}$ to suppress excitations to higher Landau levels and the disorder of the sample is small enough, though not vanishing, $0 < V_{\mathrm{d}} \ll \hbar\omega_{\mathrm{B}}$ to cause broadening and localization of extended states.

2.3 Fractional quantum Hall effect

From a phenomenological point of view the FQH and IQH feature similar properties in that both show a quantized Hall resistivity at which the longitudinal resistivity vanishes. In contrast to the integer values in the IQH effect, In the FQH effect, the Hall resistance takes fractional values of the von Klitzing constant $R_{\mathrm{K}} = h/e^2$, the most prominent one being the $\nu = 1/3$ plateau, see Fig. 2.5.

However, the nature of the energy gap in the FQH effect is of fundamental difference from the IQH effect. In the latter, the gap arises from a single particle effect given by the separation of the Landau levels, while in the former, the energy gap stems from a many-body effect caused by the inter-particle Coulomb interaction between the electrons in the LLL. Laughlin proposed with an ingenious intuition a variational ansatz for a wavefunction that captures the essence of the FQH effect [Lau83].

2.3.1 Laughlin wavefunction

The construction of Laughlin's trial wavefunction to describe the ground state of the $\nu = 1/3$ FQH effect was largely inspired by the following arguments [Lau83]. The Coulomb interactions between the electrons are repulsive, hence electrons tend to maximize their distance to lower the interaction energy. Thus, the trial wavefunction should be composed of a term which minimizes the inter-electron distance of the form

$$\prod_{\mathrm{i}<\mathrm{j}}^{\mathrm{N}} f(z_{\mathrm{i}} - z_{\mathrm{j}}). \tag{2.16}$$

Here, f is a function that vanishes for $(z_{\mathrm{i}} - z_{\mathrm{j}}) \to 0$. These type of functions are known as Jastrow-type wavefunctions [Jas55] in which only two-body correlations are taken into account and higher orders are neglected. Furthermore, f needs to be antisymmetric due to the spinless fermionic nature of the particles. To ensure that the wavefunction

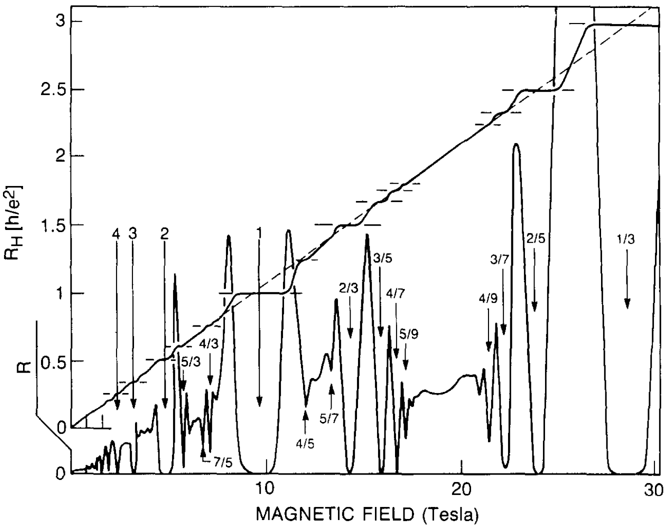

Figure 2.5: Fractional quantum Hall effect. Similar to the IQH effect, the FQH effect exhibits a quantized Hall resistance R_{H}, however at fractional values of the von Klitzing constant $R_{\mathrm{K}} = h/e^2$, accompanied with a vanishing longitudinal resistance R, at strong magnetic fields and low temperatures. Taken from [Sto92].

can be normalized, an exponential factor for each particle is factored out, yielding

$$\psi(z_1, ...z_N) = \prod_{\mathrm{i<j}}^{\mathrm{N}} f(z_{\mathrm{i}} - z_{\mathrm{j}})\ e^{-\sum_{\mathrm{i}=1}^{N} |z_{\mathrm{i}}|^2/4l_{\mathrm{B}}^2}. \tag{2.17}$$

The variational approach suggests to vary the Jastrow function f until the expectation value of the Hamiltonian minimizes the total energy. However, we can impose further constraints on f that remove the variational degree of freedom. First, the many-body wavefunction can be constructed from single particle wavefunctions in the LLL, see Eq. (2.15). Second, f needs to be odd fulfilling $f(-z) = -f(z)$. And third, the wavefunction is an eigenstate of the total angular momentum $M = \sum_{\mathrm{i}} m_{\mathrm{i}}$ which implies that f is a homogeneous polynomial[3] of degree M. Note that the constraints to the wavefunction also apply to excited states of the system. The only function which obeys all three restrictions is $f(z) = z^m$ with m an odd integer. Thus, we arrive at the famous

---

[3] If a polynomial P is homogenous of order d, then $P(\lambda x_1, ..., \lambda x_{\mathrm{N}}) = \lambda^d P(x_1, ..., x_{\mathrm{N}})$

Laughlin wavefunction

$$\psi_{1/m}(z_1,...z_N) = \prod_{\mathrm{i}<\mathrm{j}}^{N}(z_\mathrm{i} - z_\mathrm{j})^m \; e^{-\sum_{\mathrm{i}=1}^{N}|z_\mathrm{i}|^2/4l_\mathrm{B}^2}, \tag{2.18}$$

which is an eigenstate of the angular momentum operator with the eigenvalue

$$M = \frac{N(N-1)}{2}m. \tag{2.19}$$

Note that even though the Laughlin wavefunction is a variational ansatz, it does not contain any variational parameters since the angular momentum m fixes the filling factor $\nu = 1/m$ within the LLL.

One of the main characteristic of the Laughlin wavefunction is the distribution of the zero points. For a filling factor $\nu = 1/m$, the probability density $|\psi_{1/m}|^2$ of two of any electrons in the system decreases with the power $2m$. These are *deep nodes*[4] in the probability of two electrons to approach each other, quantitatively stronger than the Pauli exclusion of two fermions which scales only linearly, i.e. $m = 1$. Furthermore, due to the structure of the prefactor $(z_\mathrm{i} - z_\mathrm{j})^m$ there exists a single node for each electron with respect to all others. These bound states of zero points and electrons are also called vortices as they are accompanied with a phase winding of the wavefunction. In conclusion, the incorporation of relative angular momentum m of an electron with respect to each and every other electron in the system results in a reduction of the repulsive Coulomb interaction and to an overall reduction of the total energy of the system

2.3.2 Classical plasma analogy

The only variational parameter of the Laughlin wavefunction is the relative angular momentum m between the electrons. Even though m fixes the filling factor $\nu = 1/m$ in the LLL, we can still assess which one of the Laughlin states has the lowest energy. Therefore, we express the probability density distribution in the form

$$|\psi_{1/m}|^2 = e^{-\beta\Phi}, \tag{2.20}$$

where $\beta = 2/m$ and a classical potential energy

$$\Phi = -\sum_{\mathrm{i}<\mathrm{j}} 2m^2 \ln|z_\mathrm{i} - z_\mathrm{j}| + \frac{m}{2l_\mathrm{B}^2}\sum_\mathrm{i}|z_\mathrm{i}|^2, \tag{2.21}$$

---

[4] This notion was coined by Laughlin in [Gir89]

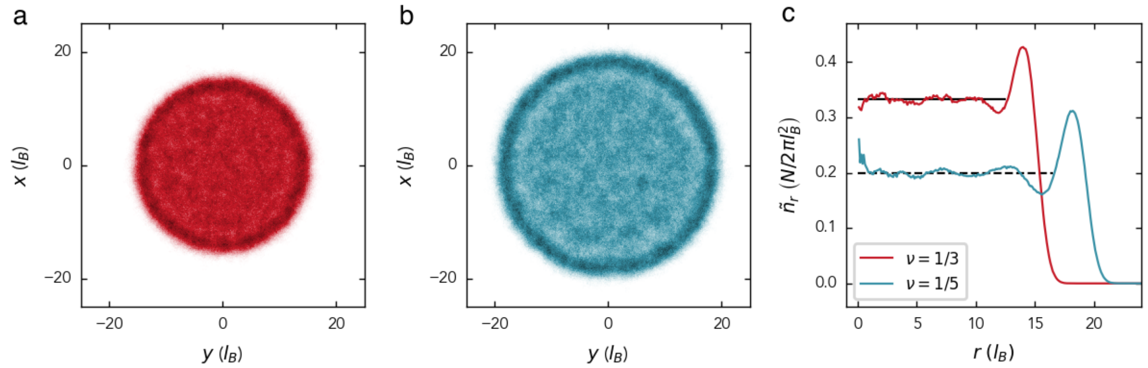

Figure 2.6: Density distribution of the Laughlin wavefunction. a, b, Normalized 2D density distribution of $N = 42$ particles occupying the $\nu = 1/3$ (red) and $\nu = 1/5$ (blue) Laughlin state calculated via Monte Carlo simulation [Tom18]. **c**, Radial density of the $\nu = 1/3$ (red) and $\nu = 1/5$ (blue) Laughlin state normalized with respect to the particle number N. Characteristic for the incompressibility of the FQH fluid is the flat density at 1/3 (solid line) and 1/5 (dashed line) extending up to a radius $r_{\text{max}} \simeq \sqrt{2Nm} l_{\text{B}}$. At the edge, the density exhibits a peak and falls off to zero.

which, remarkably, is a well known studied problem in statistical mechanics, namely the one-component plasma (OCP) in two dimensions. The choice of $\beta = 2/m = 1/k_{\text{B}}T$ can be interpreted as a temperature at which the system is in thermal equilibrium.

We further identify the two terms in Eq. (2.21) by correspondence with the OCP. The first term coincides with the Coulomb potential energy in two dimensions which scales logarithmically. This is seen by considering the Poisson equation of a point charge $-\nabla^2\phi = 2\pi\delta(\boldsymbol{r})$ in two dimensions, from which we obtain the Coulomb potential $-q^2 \ln(r/l_{\text{B}})$. The second term scales quadratically with the radius. Using again the Poisson equation, we get $-\nabla^2(r^2/4l_{\text{B}}^2) = -1/l_{\text{B}}^2$. Hence, the electrons of the plasma experience a homogeneous background density $\rho = 1/2\pi l_{\text{B}}^2$. In order to minimize their energy, the electrons neutralize the homogeneous background density $\rho + mn = 0$ such that the electron density reaches $n = 1/2\pi l_{\text{B}}^2 m$, which is exactly the density at a filling factor $\nu = 1/m$. Therefore, the analogy with the OCP tells us that the average density distribution of the FQH state is constant with a density of $1/m$ in units of $2\pi l_{\text{B}}^2$.

We use numerical methods to visualize the density distribution of many particles occupying the Laughlin state. In particular, we calculate 2D density through the Metropolis Monte Carlo (MC) algorithm [Tom18] which is an established method to

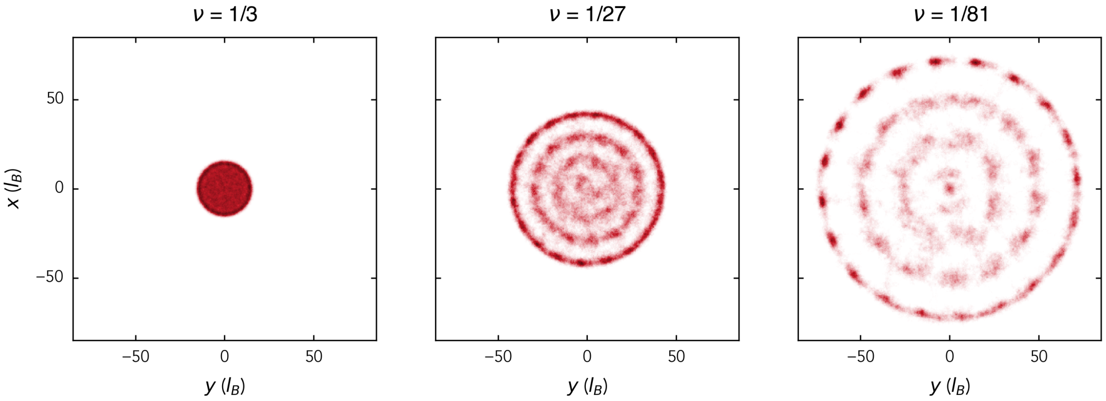

Figure 2.7: Crystallization of the FQH fluid. MC simulation of the 2D normalized density distribution of the $N = 42$ particle Laughlin wavefunction as the filling factor $\nu = 1/m$ is decreased (from left to right).

calculate properties of FQH states which depend on the particles position [Mor86; Kjø99; Umu18]. In Fig. 2.6, we show the 2D and azimuthally averaged density of the $\nu = 1/3$ and $\nu = 1/5$ Laughlin state of $N = 42$ particles. The Laughlin state exhibits its characteristic flat density profile within the bulk, up to a maximum radius given by the particle number and the relative angular momentum $\sim \sqrt{2(N-1)m}$. As the filling factor $\nu = 1/m$ decreases, each particle acquires a larger angular momentum thereby carving out more space less likely to be occupied by the neighbouring particles. Hence, the increase in the radial size of the density.

Furthermore, in the OCP an important quantity is the plasma parameter Γ which relates the Coulomb interaction to the temperature. Identifying the corresponding energy scales in the quantum system, the plasma parameter takes the form

$$\Gamma = \frac{E_{\text{Coulomb}}}{E_{\text{thermal}}} = 2m. \tag{2.22}$$

Numerical simulations show [Bau80] that at large $\Gamma > 140$ the OCP crystallizes as the Coulomb interactions dominate over the thermal energy, while for smaller $\Gamma < 140$ the OCP behaves as a fluid.

In particular, in the case of the FQH states at $\nu = 1/3, 1/5$ the Laughlin wavefunction describes an *incompressible* quantum fluid [Lau83; Gir85]. The origin of the incompressibility stems from a finite energy gap of low-lying quasiparticle excitations within the bulk of the system [Gir84; Gir85; Gir86; Hal85]. In addition to the finite gap of the collective excitation spectrum at small wavevectors, the spectrum exhibits a minimum at finite wavevectors associated to a *magneto-roton*, similar to the roton minimum in superfluid helium [Fey72]. The deepening of the magneto-roton for decreasing filling factors ν is interpreted as a precursor of a Wigner crystal [Wig34; Tsu24].

In Fig. 2.7, we show the crystallization of the FQH liquid by gradually decreasing the filling factor using MC simulation. At comparatively large filling factors $\nu = 1/3$ the density is flat within the bulk region, while the crystalline structure manifests via a periodic density modulation along the radial and azimuthal direction, as the filling factor is further reduced. Since the Laughlin state is a variational ground state wavefunction, it is expected that the Laughlin state is not a good approximation anymore of the true ground state at smaller filling factors.

2.3.3 Haldane pseudopotentials

What makes the Laughlin wavefunction such an effective approximation for the ground state of the $\nu = 1/3$ FQH state? Despite the large overlap with the ground state [Fan86], it is however not the exact ground state due to the long-range order of the Coulomb interaction. Following this line of thought, Haldane constructed a toy model with short-range interactions in which the Laughlin state becomes the *exact* ground state of the system [Hal83a] This method turns out to be quite powerful, as the toy model allows to determine for which interaction parameters the Laughlin state approximates the exact ground state satisfactory.

The conceptual idea is to construct a set of parameters $\mathcal{V}_m$ which characterize the interaction energy of pairs of particles with relative angular momentum m. These are the expectation value of the interaction potential V_{int} satisfying the relation [Hal83a; Sim07]

$$\mathcal{V}_m = \frac{\langle \varphi_m | V_{\text{int}} | \varphi_m \rangle}{\langle \varphi_m | \varphi_m \rangle}, \tag{2.23}$$

and are referred to as *Haldane pseuodpotentials*. Knowledge of the interaction potential V_{int} uniquely determines the pseudopotentials. However, the opposite is not true, as there are many interaction potentials for the same pseudopotentials. They uniquely determine the properties of the system for isotropic interactions.

Here, $\mathcal{V}_m$ does not depend on the total angular momentum for central potentials $V(|\boldsymbol{r}_1 - \boldsymbol{r}_2|)$ as the eigenstates factorize in center-of-mass and relative motion due to the conservation of angular momentum. Since φ_m peaks at a radius $r = \sqrt{2m} l_{\text{B}}$ the eigenvalues $\mathcal{V}_m$ approximately correspond to the value of the interaction potential at the peak radius $\mathcal{V}_m \sim V_{\text{int}}(r = \sqrt{2m} l_{\text{B}})$. In a toy model of spin-polarized fermions with only short-range interaction in which all pseudopotentials are zero, except $\mathcal{V}_1 \neq 0$, the Laughlin wavefunction is the exact ground state with an eigenvalue zero [Hal83a].

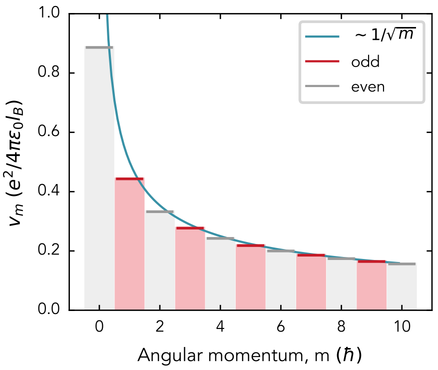

Figure 2.8: Haldane pseudopotentials for Coulomb interaction. Calculated Haldane pseudopotentials in the LLL for Coulomb interactions in 2D and in units of $e^2/4\pi\epsilon_0 l_\mathrm{B}$. Even $\mathcal{V}_m$ are greyed out since they don't contribute to the interaction of spin polarized fermions.

Furthermore, the pseudopotential $\mathcal{V}_1$ determines the scale of the energy gap to higher lying excitations.

We calculate the Haldane pseudopotentials for electrons interacting via Coulomb interactions $V_\mathrm{int} = e^2/4\pi\epsilon_0 r$ in the LLL, with a negligible extend in the vertical direction (modelled via a Dirac δ). The mth pseudopotential takes the form

$$\mathcal{V}_m = \frac{e^2}{4\pi\epsilon_0} \int_0^{2\pi} \mathrm{d}\phi \int_0^{\infty} \mathrm{d}r |\varphi_m(r,\phi)|^2, \tag{2.24}$$

where we integrated out the axial direction and expressed the single-particle states in the LLL in Eq. (2.15) in polar coordinates r, ϕ. Solving the integral then yields

$$\mathcal{V}_m = \frac{\Gamma\left(m+\frac{1}{2}\right)}{2m!} \frac{e^2}{4\pi\epsilon_0 l_\mathrm{B}}. \tag{2.25}$$

We show the lowest $\mathcal{V}_m$ in Fig. 2.8. The even $\mathcal{V}_m$ (greyed out) do not contribute to the interaction since we consider spin polarized fermions. The magnitude of $\mathcal{V}_m$ decreases monotonically with increasing angular momentum m in the LLL, provided that the real interaction potential behaves similarly.

To close the circle to the initially posed question of this section regarding the overlap of the Laughlin wavefunction with the exact ground, we compare the lowest Haldane pseudopotential $\mathcal{V}_1$ with higher angular momenta $\mathcal{V}_1 = 0.44 > \mathcal{V}_3 = 0.28, \mathcal{V}_5 = 0.22$, which supports that the Laughlin wavefunction is a good approximation to the ground

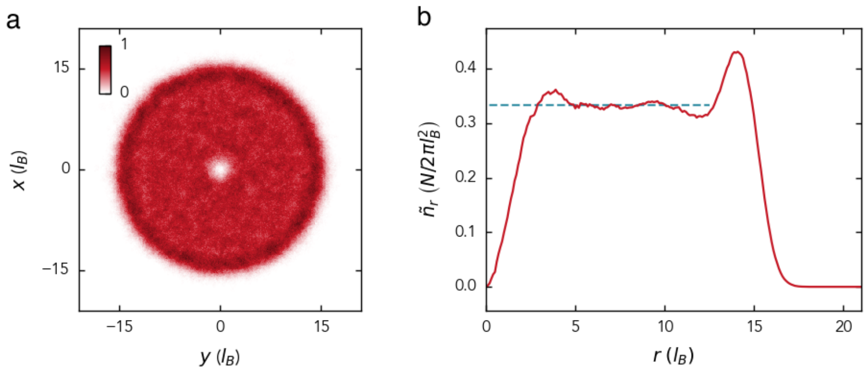

Figure 2.9: Quasihole excitation. a, Normalized 2D density distribution of $N = 42$ particles occupying the $\nu = 1/3$ Laughlin state with a single quasihole excitation, calculated via MC simulation [Tom18]. **b**, Azimuthal average of the 2D density to visualize the density drop to zero at the position of the quasihole. The blue dashed line corresponds to 1/3 in the units of the density.

state. On the other hand, for large angular momenta the pseudopotentials scale with $\mathcal{V}_m \simeq 1/2\sqrt{m}$ and the difference in $\mathcal{V}_m$ and $\mathcal{V}_{m+2}$ decreases. Hence at low filling factors $m \gg 1$, the Laughlin state is expected to deviate from the real ground state. This is consistent with the instability of the FQH liquid with respect to the appearance of a Wigner crystal at $\nu < 1/7$ [Pap22; Tsu24].

2.3.4 Quasihole excitations

The Laughlin wavefunction $\psi_{1/m}$ hosts excitations with a fractional value of the elementary charge e/m, these are *quasi-hole* and *quasi-particle* excitations [Lau83]. Here, we focus on the quasi-hole excitations.

The wavefunction of such a quasi-hole excitation is constructed by adding a zero point at the position η in the radial plane with respect to the each particle

$$\psi^{(\text{hole})}_{1/m}(z_1, ..., z_\text{N}, \eta) = \prod_{\text{i}=1}^{\text{N}} (z_\text{i} - \eta) \prod_{\text{i}<\text{j}}^{N} (z_\text{i} - z_\text{j})^m \; e^{-\sum_{\text{i}=1}^{N} |z_\text{i}|^2/4l_\text{B}^2}. \tag{2.26}$$

In order to calculate the charge of the hole, we make use again of the plasma analogy. The classical potential energy from Eq. (2.21) with the included hole reads

$$\Phi^{(\text{hole})}_\eta = \Phi - m \ln |z_\text{i} - \eta|. \tag{2.27}$$

The hole in the Laughlin wavefunction leads to an additive term in the classical potential energy. Thus, the electrons experience on top of the uniform background density an additional charge at the position of the hole, with a unit test charge. To ensure overall charge neutrality of the system, a deficit of $1/m$ electrons close to η is required, from which follows that the hole carries a charge of e/m. Furthermore, we calculate the 2D and radial density of the Laughlin wavefunction with a quasihole excitation by means of MC simulation, shown in Fig. 2.9. At the position of the quasihole, which is arbitrarily chosen at the center, the flat bulk density falls off to zero.

2.3.5 Halperin states – spinful Laughlin states

So far we have neglected the spin of the electrons, the energy of which scales with $E = g\mu_{\mathrm{B}} m_{\mathrm{s}} B$. In free space, the Landé factor of the electron is $g \approx 2$ while the spin component along the magnetic field axis is $m_{\mathrm{s}} = 1/2$. This energy scales with $E \simeq \hbar\omega_{\mathrm{B}}$ and is therefore significantly larger than the Coulomb interaction within the LLL. However, the Landé factor in semiconductor materials can decrease drastically compared to free space, as well as spin-orbit coupling can change the effective mass of the electrons. These effects lead to the reduction of the Zeeman splitting thereby rendering the spin degree of freedom a comparable energy scale to the Coulomb interactions, first observed experimentally in a double-layer electron system [Sue92]

Halperin proposed an extension of the Laughlin wavefunction to account for the spin degree of freedom [Hal83b]

$$\psi_{m_\uparrow,m_\downarrow,n}(z_1,...,z_{\mathrm{N}},\xi_1,...,\xi_{\mathrm{N}}) \propto \prod_{\mathrm{i<j}}^{N_\uparrow}(z_{\mathrm{i}}-z_{\mathrm{j}})^{m_\uparrow}\prod_{\mathrm{i<j}}^{N_\downarrow}(\xi_{\mathrm{i}}-\xi_{\mathrm{j}})^{m_\downarrow}\prod_{\mathrm{i,j}}^{N_\uparrow,N_\downarrow}(z_{\mathrm{i}}-\xi_{\mathrm{j}})^{n}, \qquad (2.28)$$

where we disregard the Gaussian envelope of each spin state for the sake of simplicity. The variables z_{i}, ξ_{i} label the complex coordinate of the ith spin up, spin down particle, respectively, in the radial plane of the system. They are expressed in units of l_{B}. The exponents $m_{\uparrow,\downarrow}$ are odd integers determining the relative angular momentum between particles with the same spin, and $n > 0$ is an integer. This set of wavefunctions characterized by $(m_\uparrow, m_\downarrow, n)$ are referred to as *Halperin states*.

A particularly prominent Halperin state is a spin singlet [Hal88], i.e. the total spin is zero in a balanced mixture of spin states $N_\uparrow = N_\downarrow = N$, and one which contains equal relative angular momentum in both spin states $m_\uparrow = m_\downarrow = m$. The anti-symmetry of the wavefunction under exchange of same spin states imposes that m is odd. Since the spin singlet is antisymmetric, we require that n is even. The respective Halperin state is thus characterized by the set $(n+1, n+1, n)$. The total filling factor in the LLL of such a state is then given by

$$\nu = \nu_{\uparrow} + \nu_{\downarrow} = \frac{2}{2n+1}. \tag{2.29}$$

The simplest case $(1,1,0)$ corresponds to an IQH state where each of the spin states fully occupies the LLL, hence $\nu = 2$ and $\nu_{\uparrow,\downarrow} = 1$. Here, both spin states form Fermi seas which are uncorrelated with respect to each other. More interestingly is the first state with vanishing interactions $(1,1,1)$, which corresponds to a ferromagnetic state due to the long-range order among all particles.

2.4 Ultracold quantum gases in synthetic magnetic fields – a rotating perspective

Ultracold atomic gases in synthetic magnetic fields allow the study of quantum many-body physics in magnetic fields with unprecedented control of the system parameters such as the density, interaction strength or geometry [Blo08; Blo12], with an enormous variety of observables ranging from microscopy of individual atoms [Gro21b] to collective excitations [Ket08] or transport measurements [Chi15]. Realizing FQH states in these engineered systems has the potential to unravel unanswered questions in the field of quantum Hall physics [Kli20; Coo08; Gol14; Gol16; Coo19]. We outline the generation of synthetic magnetic fields in ultracold atoms and establish relevant connections to the solid state systems. Details on the preparation and manipulation of ultracold quantum gases can be found in the next chapter 3.

2.4.1 Rotating quantum gases

When an external magnetic field is applied perpendicular to a 2D plane, charged particles that move on a full circle of their cyclotron orbits accumulate a complex phase, known as the Aharonov-Bohm phase [Aha59]. Neutral atoms on the contrary are rather insensitive to external magnetic fields which necessitates other methods to engineer such a complex phase. There are several experimental techniques to realize synthetic magnetic fields, based on the underlying principle that particles which adiabatically move on a closed path in Hilbert space acquire a *geometric phase* after a full trajectory. The notion of geometry arises from the fact that this phase is unchanged regardless of the exact dynamics of a specific path. Such a geometric phase is referred to as Berry phase [Ber84] and is a generalization of the Aharonov-Bohm phase [Wu75].

In Fig. 2.10, different approaches in ultracold atomic gases are illustrated. Floquet engineering in optical lattices renders the tunneling amplitudes between lattice sites

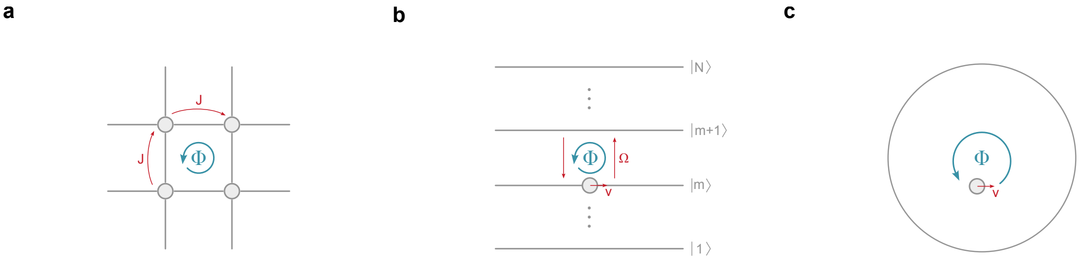

Figure 2.10: Geometric phases in ultracold atoms. Different realizations of a geometric phase in ultracold atomic gases analogous to the Aharonov-Bohm phase experienced by an electron subjected to a magnetic field. **a,** Due to Laser-assisted tunneling J in optical lattices, the atom acquires a complex phase when tunneling along a closed circle. **b,** In a coherent two-photon process Ω the internal states $|m\rangle$ of the atom are coupled to their center-of-mass velocity, known as spin-orbit coupling. **c,** The analogue of the Lorentz and Coriolis force introduces an artificial Aharonov-Bohm phase in a rotating system.

complex, thereby imprinting a non-vanishing geometric phase after a closed hopping loop [Aid11; Jim12; Miy13; Aid13b; Aid13a; Aid14; Ken15; Tai17; Ast19; Str12; Jot14; Win20]. A geometric phase can also be engineered by coupling the spin and the motional degree of freedom [Lin09; Man15; Stu15; Cha20; Zho23]. Here, the atoms are dressed by an optical light field that imparts a momentum on the atoms when coupled to a different spin state.

However, one of the most intuitive approaches to engineer a synthetic magnetic field, which leads to the accumulation of a geometric phase, is to simply rotate the system [Mad00; Abo01; Sch04; Bre04; Zwi05; Fle21]. This technique makes use of the analogy of the Lorentz force $q\boldsymbol{v} \times \boldsymbol{B}$ and the Coriolis force $2m_\mathrm{a}\boldsymbol{v} \times \boldsymbol{\Omega}$, where $\boldsymbol{v}$ is the velocity of a particle, m_a its mass and $\boldsymbol{\Omega}$ the rotation frequency. Similar to electrons that are constrained by a magnetic field to move on cyclotron orbits, neutral particles rotate on closed orbits, thereby acquiring a geometric phase.

Formally in the quantum mechanical context, we consider the Hamiltonian

$$\mathcal{H} = \frac{p^2}{2m_\mathrm{a}} + \frac{m_\mathrm{a}}{2}\omega^2 r^2 \tag{2.30}$$

of a single particle confined in a rotationally symmetric, 2D harmonic potential with a harmonic oscillator frequency ω. By transformation of the Hamiltonian in the laboratory frame to the rotating frame of reference

$$\mathcal{H}_\Omega = \mathcal{H} - \Omega L_\mathrm{z} \tag{2.31}$$

the angular momentum operator $\boldsymbol{L} = \boldsymbol{r} \times \boldsymbol{p}$ is introduced and directly projected along the axial direction since the rotation is perpendicular to the motional plane of the atom. Rewriting the Hamiltonian yields

$$\mathcal{H}_\Omega = \frac{(\boldsymbol{p} - m_\mathrm{a}\boldsymbol{\Omega} \times \boldsymbol{r})^2}{2m_\mathrm{a}} + \frac{m_\mathrm{a}}{2}\left(\omega^2 - \Omega^2\right) r^2. \tag{2.32}$$

In the deconfinement limit $\Omega \to \omega$ the second term, corresponding to the trapping potential, vanishes. The Hamiltonian then resembles a particle with charge q in a 2D plane exposed to a vector potential $q\boldsymbol{A} = m_\mathrm{a}\boldsymbol{\Omega} \times \boldsymbol{r}$. We identify the analogue quantities $q\boldsymbol{B} = 2m_\mathbf{a}\boldsymbol{\Omega}$ from which we can define the effective magnetic length in the rotating atomic gas

$$l_\mathrm{B} = \sqrt{\frac{\hbar}{qB}} = \sqrt{\frac{\hbar}{2m_\mathrm{a}\omega}} = \frac{l_\mathrm{HO}}{\sqrt{2}}. \tag{2.33}$$

The magnetic length l_B only differs by a factor $1/\sqrt{2}$ from the natural length scale l_HO of the harmonic oscillator.

The Hamiltonian $\mathcal{H}_\Omega$ is exactly solvable for all rotation frequencies Ω [Coo08]. The eigenstates are classified by their primary quantum number n and angular momentum m, and take the form in real space coordinates

$$\varphi_{n,m}(r,\phi) = \frac{1}{\sqrt{\pi l_\mathrm{HO}^2}}\sqrt{\frac{k!}{(k+|m|)!}}e^{im\phi}\rho^{|m|}e^{-\rho^2/2}L_k^{|m|}\left(\rho^2\right), \tag{2.34}$$

where we have introduced $k = 1/2(n - |m|)$, the dimensionless radius $\rho = r/l_\mathrm{HO}$ in units of the harmonic oscillator length and the associated Laguerre Polynomials $L_k^m(\rho)$ of degree k and order m. In the LLL $k = 0$, the maximum available angular momentum with respect to its primary quantum number is $n = m$, and we retrieve the same eigenstates as for a charged particle exposed to an external magnetic field in Eq. (2.15).

Furthermore, the eigenenergies as a function of the rotation frequency take the form

$$E_\mathrm{n,m} = (2n + 1 + |m|)\hbar\omega - m\hbar\Omega, \tag{2.35}$$

shown in Fig. 2.11. In the non-rotating limit $\Omega/\omega = 0$ the energy levels are equally spaced with the harmonic oscillator frequency $\hbar\omega$ and display the characteristic shell

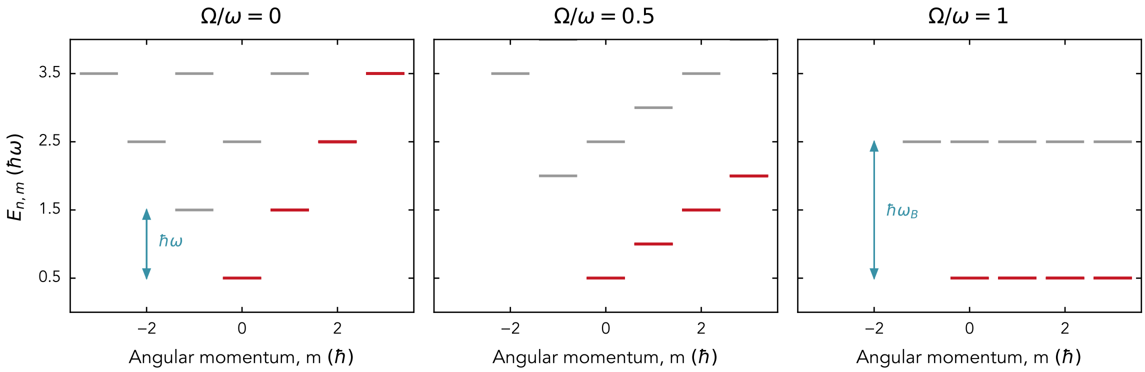

Figure 2.11: 2D harmonic oscillator levels. Energy levels of the 2D harmonic oscillator with trap frequency $\hbar\omega$, rotated with a frequency Ω. Without rotation, we retrieve the typical shell structure where each level has a degeneracy $n+1$. Increasing the rotation frequency breaks the degeneracy by shifting levels with $m > 0$ ($m < 0$) up (down) in energy due to the preferred rotation direction. In the deconfinement limit $\Omega = \omega$, the level structure resembles that of Landau levels, where each level contains infinitely many degenerate levels which are separated by the cyclotron frequency $\hbar\omega_{\mathrm{B}}$. States in the LLL are highlighted in red.

structure of the 2D harmonic oscillator, where each energy level has a degeneracy of $n+1$ due to the rotational symmetry. Increasing Ω breaks this degeneracy due to the energy levels shifting higher / lower depending on the sign of their angular momentum m. The eigenstates, however, are not affected by the rotation since the angular momentum is still a conserved quantity. In the deconfinement limit $\Omega/\omega = 1$, the level structure is reminiscent of Landau levels, where each level is highly degenerare and separated by the cyclotron frequency $\omega_{\mathrm{B}} = 2\omega$.

Hence, a single neutral atom confined in a 2D harmonic potential which rotates in the deconfinement limit $\Omega \to \omega$ is formally equivalent to a charged particle exposed to an external magnetic field. However, we are interested in strongly correlated many-body states within the LLL, which imposes the condition on the energy of the interaction strength to be smaller than the separation of the Landau levels, given by ω_{B}.

2.4.2 The filling factor

In the context of the FQH effect, the phases of matter are characterized by the filling factor ν [Giu12], which is defined as the electron density n_{e} that occupies a partially filled Landau level

$$\nu = 2\pi n_\mathrm{e} \frac{\hbar}{eB} = 2\pi n_\mathrm{e} l_\mathrm{B}^2. \tag{2.36}$$

In ultracold atomic gases, the filling factor can be expressed by the 2D atomic density n_2D and the analogous expression for the magnetic length (see Eq. (2.33))

$$\nu = 2\pi n_\mathrm{2D} \frac{\hbar}{2m_\mathrm{a}\omega} = \frac{n_\mathrm{2D}}{n_\mathrm{v}}, \tag{2.37}$$

where we have introduced the vortex density n_v [Don91]. Assuming a uniform density we arrive at

$$\nu = \frac{N}{N_\mathrm{v}}, \tag{2.38}$$

which defines the filling factor as the ratio of number of atoms per number of vortices.

Similarly to the FQH effect, the filling factor controls the emergent phases of matter in repulsively interacting BECs [Wil98; Coo01]. Above a critical filling factor $\nu > \nu_\mathrm{c} \sim 17$ [Bay04], the ground state of the system is qualitatively well described by the mean-field Gross-Pitaevskii equation [Coo08; Pit16]. It consists of a triangular vortex lattice, also known as Abrikosov lattice in analogy to type-II superconductors [Til19]. Close to the critical filling factor ν_c, quantum fluctuations of the vortices become dominant, which leads to a breakdown of mean-field theory. A zero temperature quantum phase transition from a BEC to a strongly correlated quantum Hall liquid is anticipated [Coo01; Sin02]. In particular, at a filling factor of $\nu = 1/2$, that is a total angular momentum of $L = N(N-1)$, the exact ground state of repulsively, contact interacting bosons is a bosonic Laughlin state [Wil98; Lau83].

We emphasize that when bosons occupy the LLL, i.e. $\mu < \hbar\omega_\mathrm{B}$, it does *not* signal the onset of the fractional quantum Hall regime $\nu \lesssim 1$. This is in contrast to spinless fermions, where Pauli exclusion principle allows only one particle per state. Consider the example of non-interacting bosons where all occupy the ground state of a 2D harmonic oscillator. The chemical potential is vanishing and therefore significantly smaller than the cyclotron frequency $\mu \ll \hbar\omega_\mathrm{B}$, on the other hand, the filling factor diverges $\nu \to \infty$ since all particles occupy a state with zero angular momentum.

2.4.3 Haldane pseudopotentials in ultracold atoms

Ultracold atomic gases serve as a well controllable experimental platform to study exact ground states of the FQH effect since their zero-range contact interactions accurately fulfil the conditions of Haldanes toy model. In fact, all Haldane pseudopotentials introduced in Eq. (2.23) are exactly zero at these ultracold temperatures except of the zeroth order $\mathcal{V}_0$ (considering either bosons or spinful fermions). This renders the Laughlin state the exact ground state in the deconfining rotating limit.

Similar as in the previous subsection on the Haldane pseudopotentials, we calculate $\mathcal{V}_m$ for a contact interacting potential $V_{\text{int}} = 4\pi\hbar^2 a_{\text{s}}\delta(\boldsymbol{r})/m_{\text{r}}$ (see next chapter 3 for more details on interactions in ultracold atoms), where a_{s} is the scattering length in three dimensions which provides a measure for the strength of the interaction, and m_{r} is the relative mass of the atoms. We take into account a finite, Gaussian extend in the axial direction l_{ax}, however assuming a quasi-2D regime $l_{\text{ax}} \ll l_{\text{HO}}$. The relative wavefunction of two particles in the LLL is then given in cylindrical coordinates by

$$\varphi_m(r, \phi, z_{\text{ax}}) = \frac{1}{\sqrt{\pi m! l_{\text{HO}}^2}} \left(\frac{re^{i\phi}}{l_{\text{HO}}}\right)^m e^{-r^2/4l_{\text{HO}}^2} \frac{1}{\sqrt{2\pi l_{\text{ax}}^2}} e^{-z_{\text{ax}}^2/4l_{\text{ax}}^2} \tag{2.39}$$

We have introduced the axial coordinate z_{ax}, not to be confused with the complex coordinate z in the radial plane and expressed the wavefunction in units of the harmonic oscillator length in the radial plane l_{HO} and the axial direction l_{ax} since these are the natural units in the harmonic potential. From this expression, we can immediately see that higher angular momentum states $m > 0$ possess a node in the relative two-particle wavefunction as they scale with $\sim r^m$ and thus are exactly zero in the context of zero-range interactions. The only Haldane pseudopotential which survives is

$$\mathcal{V}_0 = \int_0^{2\pi} \mathrm{d}\phi \int_0^{\infty} \mathrm{d}r \int_{-\infty}^{\infty} \mathrm{d}z_{\text{ax}} |\varphi_0(r, \phi, z_{\text{ax}})|^2 \frac{4\pi\hbar^2 a_{\text{s}}}{m_{\text{r}}} \delta(\boldsymbol{r}) \tag{2.40a}$$

$$= \sqrt{\frac{2}{\pi}} \frac{a_{\text{s}}}{l_{\text{ax}}} \hbar\omega. \tag{2.40b}$$

It depends on three variables, the scattering length a_{s}, the radial trap frequenc ω and the axial harmonic oscillator length l_{ax}, which are all independently tunable in typical ultracold atom experiments. Hence, at low energies in the quasi-2D LLL, the zeroth pseudopotential $\mathcal{V}_0$ defines the only relevant energy scale in rapidly rotating ultracold Bose and two-component Fermi gases.

We remark that rotating ultracold atoms with dipolar long-range interactions, realized in the slow rotating limit [Kla22], could be used to model toy Hamiltonians with contributions from all $\mathcal{V}_m$ [Bar12; Cho22].

3

Ultracold quantum gases

With the advent of Bose-Einstein condensation [And95; Dav95] and the realization of degenerate Fermi gases [DeM99], completely new platforms emerged for studying complex quantum many-body physics in very clean and controlled environments [Blo08; Blo12]. The degree of control has been a gold standard in ultracold quantum gas experiments from early on, leading to an impressive technological development up to the manipulation of these systems on the single particle level, in various platforms ranging from optical lattices in quantum gas microscopes [Gro21a; Blo12], tweezer arrays of Rydberg atoms [Bro20], to few-body quantum systems in a single optical tweezer [Ser11a].

This chapter aims to provide a concise overview on the concepts of ultracold quantum gas experiments which are of relevance for this thesis. In particular, we outline the properties of fermionic Lithium 6 which is used throughout all the experiments. We give an introduction into the scattering processes at ultracold temperatures and their tunability via a Feshbach resonance. In the last section, optical dipole traps are introduced for trapping neutral atoms.

3.1 Bosons and fermions

Particles are identical if they cannot be distinguished by any intrinsic property. A quantum mechanical system of N identical particles described by the many-body wavefunction ψ must be invariant under the successive interchange of particles at position $\boldsymbol{r}_\mathrm{i}$ and $\boldsymbol{r}_\mathrm{j}$ back to their original configuration. Such an operator P_ij needs to retrieve the identity I after two consecutive operations $P_\mathrm{ij}^2 = I$. Therefore, the eigenvalues of this operator are ±1 which distinguishes a symmetric and anti-symmetric wavefunction. The former one is referred to as *Bosons*

$$P_\mathrm{ij}\psi_\mathrm{B}(\boldsymbol{r}_1, ..., \boldsymbol{r}_\mathrm{i}, ..., \boldsymbol{r}_\mathrm{j}, ..., \boldsymbol{r}_\mathrm{N}) = +\psi_\mathrm{B}(\boldsymbol{r}_1, ..., \boldsymbol{r}_\mathrm{j}, ..., \boldsymbol{r}_\mathrm{i}, ..., \boldsymbol{r}_\mathrm{N}), \tag{3.1}$$

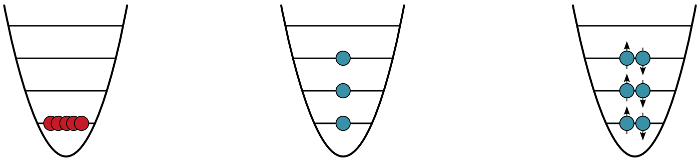

Figure 3.1: Bosons and (spinful) fermions. The exchange symmetry of the total wavefunction results in two types of particles which differ in their quantum statistics – referred to as bosons (red) and fermions (blue). An internal spin degree of freedom (denoted as an arrow), renders fermions distinguishable, which allows the occupation of the same quantum state for different spin configurations.

while the latter one are called *Fermions*

$$P_{\mathrm{ij}}\psi_{\mathrm{F}}(\boldsymbol{r}_1, ..., \boldsymbol{r}_{\mathrm{i}}, ..., \boldsymbol{r}_{\mathrm{j}}, ..., \boldsymbol{r}_{\mathrm{N}}) = -\psi_{\mathrm{F}}(\boldsymbol{r}_1, ..., \boldsymbol{r}_{\mathrm{j}}, ..., \boldsymbol{r}_{\mathrm{i}}, ..., \boldsymbol{r}_{\mathrm{N}}). \tag{3.2}$$

As a consequence, bosons can occupy the same state while for fermions the anti-symmetry of the wavefunction is the origin of the Pauli exclusion principle which forbids identical particles to occupy the same quantum state, illustrated in Fig. 3.1.

Let us consider two fermions with a spatial and spin degree of freedom, as this is a standard configuration in our experiments. The fermions contain a spin $s = 1/2$, which projected on the magnetic field axis can take two values $m_{\mathrm{s}} = \pm 1/2$ denoted with $|\uparrow\rangle$ and $|\downarrow\rangle$, respectively. Neglecting any coupling between the spin and spatial degree of freedom, we can write the total wavefunction as a product state of the spatial ϕ and spin part χ of the wavefunction

$$\psi = \phi(\boldsymbol{r}_1, \boldsymbol{r}_2)\chi\left(|\uparrow\rangle, |\downarrow\rangle\right). \tag{3.3}$$

The fermionic nature of the particles imposes that the total wavefunction is anti-symmetric. Hence, either the spin part is symmetric and the spatial part is anti-symmetric, or vice versa. Note that in the case of bosons either both parts need to be symmetric or anti-symmetric. There are four possible combinations for the spin wavefunction, three symmetric configurations referred to as triplets $|\uparrow\uparrow\rangle$, $|\downarrow\downarrow\rangle$, $1\sqrt{2}(|\uparrow\downarrow\rangle + |\downarrow\uparrow\rangle$ and one anti-symmetric spin singlet $\chi_{\mathrm{S}} = 1/\sqrt{2}(|\uparrow\downarrow\rangle - |\uparrow\downarrow\rangle)$. In particular, let us consider two fermions in a spin singlet and two spin polarized bosons. Both their spatial wavefunction must be symmetric to fulfil the total anti-symmetric wavefunction of the fermions and symmetric wavefunction of the bosons. Hence, in this scenario the spatial wavefunction of two spinful fermions mimics that of two bosons[1].

---

[1] We make use of this analogy by preparing a bosonic $\nu = 1/2$ Laughlin state with two fermions in

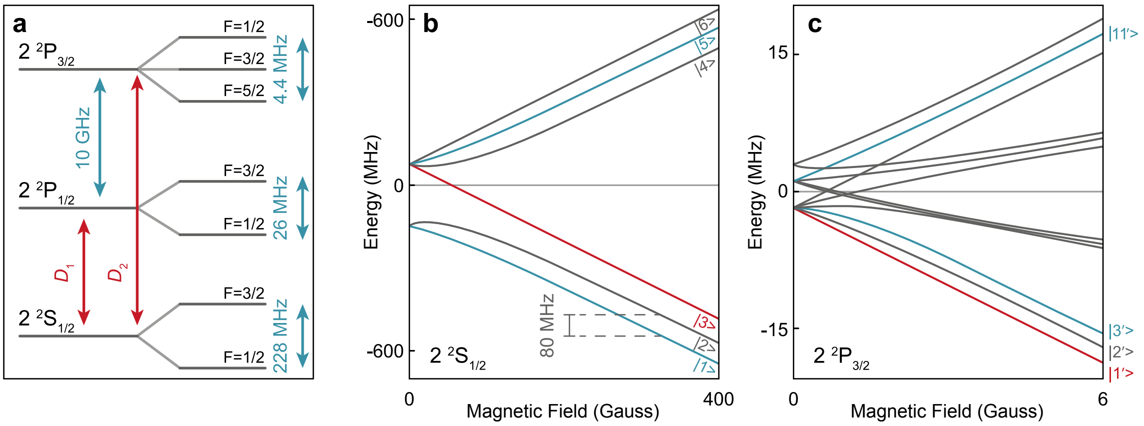

Figure 3.2: Hyperfine splitting of ^{6}Li. **a**, Fine structure (left) and hyperfine structure (right) level diagram of the electronic ground state $2^2S_{1/2}$ and the $2P$ excited states of ^{6}Li. The fine structure splitting of the excited states is given by the characteristic D_1 and D_2 lines of Alkali atoms. **b**, Magnetic field dependence of the $2^2S_{1/2}$ ground state and **c**, of the excited state $2^2P_{3/2}$. At low magnetic fields, the splitting is characterized by the total angular momentum $F = I + J$, while in the Paschen-Back regime at high magnetic fields the nuclear spin I and the total electron spin J decouple, leading to a linear energy dependence. Adapted from [Hol22].

3.2 Internal structure of lithium 6

Lithium is an excellent choice of matter for studying strongly interacting ultracold atomic gases as it hosts several beneficial properties such as a simple hydrogen-like electronic structure, a cycling transition in its electronic spectrum, resonant transitions which are easily accessible with current laser technologies, multiple stable hyperfine mixtures, a Feshbach resonance to tune inter-particle interactions, low three-body recombination rates and many more. A description *en detail* can be found in the reference [Geh03]; here, we briefly introduce the relevant concepts for this thesis.

The isotope of choice for our experiments is ^{6}Li which has a single electron in its outer-most shell exhibiting a total electron spin $S = 1/2$. Its nucleus comprises three protons and three neutrons, resulting in a total nuclear spin of $I = 1$. Consequently, the isotope is of fermionic nature. The electronic ground state $2^2S_{1/2}$ and the two lowest excited states $2^2P_{1/2}$ and $2^2P_{3/2}$ are separated by 671 nm. The excited states

---

chapter 6. This might seem odd at first glance, since for fermions only odd filling factors ν are allowed, but is possible due to the spinfulness of the fermions.

are split by 10 GHz due to spin-orbit coupling, similar to other Alkali atoms exhibiting the D_1 and D_2 lines [Tie10; Ste23]. Applying an external magnetic field results in a Zeeman shift of the energy levels, both in the ground and excited states. Typically, we work in the Paschen-Back regime at magnetic fields $> 100\,\mathrm{G}$ where the nuclear spin and electron spin decouple. The separation of energy levels of the lowest hyperfines mixtures $|1\rangle, |2\rangle, |3\rangle$ is $\sim 80\,\mathrm{MHz}$. All three combinations of hyperfine states are collisionally stable. In Fig. 3.2, we show the hyperfine splitting of ^{6}Li.

To cool and detect the atoms we solely use the D_2 cycling transition which has a linewidth $\Gamma/2\pi = 5.87\,\mathrm{MHz}$. In particular, we drive the σ^- transition from state $|3\rangle$ to $|1'\rangle$ which does not contain any admixture of the m_I sublevels at high magnetic fields (marked in red in Fig. 3.2). On the contrary, the state $|1\rangle$ is excited to $|3'\rangle$ which has a 1 % probability to decay to state $|5\rangle$. In order to close the transition we use a second laser on the σ^+ transition to couple state $|5\rangle$ to $|11'\rangle$ which has some finite overlap to $|1\rangle$ (states are marked in blue in Fig. 3.2). With that, we achieve spin resolved imaging of the two hyperfine states $|1\rangle, |3\rangle$ by subsequently addressing the optical transitions [Ber18], as further discussed in section 4.4.

3.3 Optical dipole traps

When an electric laser field is spatially aligned with an atom, it induces an atomic dipole moment. The interaction potential relates the electric field amplitude $\boldsymbol{E}$ and the induced dipole moment $\boldsymbol{p}$ of the atom $U_\mathrm{dip} = -1/2\,\langle \boldsymbol{p} \cdot \boldsymbol{E} \rangle$, where the factor 1/2 takes into account that the dipole moment is induced and the brackets $\langle\rangle$ denote the time average. Within the classical Lorentz model, this system is interpreted as a driven harmonic oscillator at a driving frequency ω set by the laser, the resonance frequency of the atom ω_0 and a damping rate Γ. The optical potential created by the laser light is described by [Gri99]

$$U_\mathrm{dip}(\boldsymbol{r}) = -\frac{3\pi c^2}{2\omega_0^3}\left(\frac{\Gamma}{\omega_0 - \omega} + \frac{\Gamma}{\omega_0 + \omega}\right) I(\boldsymbol{r}), \tag{3.4}$$

while the scattering rate of single photons by absorption and spontaneous reemission takes the form

$$\Gamma_\mathrm{sc}(\boldsymbol{r}) = \frac{3\pi c^2}{2\hbar\omega_0^3}\left(\frac{\omega}{\omega_0}\right)^3 \left(\frac{\Gamma}{\omega_0 - \omega} + \frac{\Gamma}{\omega_0 + \omega}\right)^2 I(\boldsymbol{r}). \tag{3.5}$$

Here, c is the speed of light. Therefore, at a fixed optical wavelength ω, the optical dipole potential is fully determined by the shape of the light intensity field $I(\boldsymbol{r})$, which in our experiments typically have a Gaussian distribution.

From these equations we can deduce two essential characteristics. The sign of the detuning $\Delta = \omega - \omega_0$ determines whether the dipole potential is attractive ($\Delta < 0$, referred to as red-detuned) or repulsive ($\Delta > 0$, referred to as blue-detuned). Furthermore, the potential depth scales with $U_{\text{dip}} \sim I/\Delta$ while the single photon scattering rate scales with $\Gamma_{\text{sc}} \sim I/\Delta^2$. Hence, in order to suppress scattering at the same potential depth we can choose light that is detuned further away but at a higher intensity.

3.4 Interactions in ultracold quantum gases

Tuning the interactions in ultracold quantum gases is a well established technique covered in the literature [Dal99; Ket08; Chi10], and in previous theses [Hol22; Kle21; Bay20b; Bec20b]. Here, we focus on the essential features of contact-interacting particles at ultracold temperatures.

3.4.1 Elastic collisions

The main features of the scattering processes of neutral atoms at low temperatures are captured by considering a spherically symmetric van der Waals potential $V(r) = -C_6/r^6$ at the two-body level. The van der Waals length r_0 defines the characteristic length scale $r_0 = (2m_\text{r}C_6/\hbar^2)^{1/4} \approx 60\,\text{a}_0$ of the interaction potential and is given by the van der Waals coefficient[2] C_6 and the reduced mass m_r of the colliding particles, in units of the Bohr radius a_0. The details of the inter-atomic potentials can be neglected since the typical inter-particle spacing $n^{-1/3} \sim 10\,000 a_0$ is significantly smaller than $r_0 \ll n^{-1/3}$. Therefore, it is save to assume that the elastic collision process is depicted by binary interactions determined by a single length scale, the scattering length a.

The Schrödinger equation which describes the scattering process of two colliding particles 1 and 2 can be reduced to a one-body problem in center-of-mass and relative coordinates $\mathbf{R} = \mathbf{r}_1 + \mathbf{r}_2$, and $\mathbf{r} = (\mathbf{r}_1 - \mathbf{r}_2)/2$, as the center-of-mass motion does not depend on the interaction potential and therefore is simply given by a plane wave solution. The Schrödinger equation in relative coordinates then reads

$$\left(\frac{\hbar^2}{2m_\text{r}}\nabla_\text{r}^2 + V(\mathbf{r})\right)\psi_\mathbf{k}(\mathbf{r}) = E_\mathbf{k}\psi_\text{k}(\mathbf{r}), \tag{3.6}$$

where $\mathbf{k}$ is associated with the wavenumber of the relative wavefunction, and the collision energy $E_\mathbf{k} = \hbar^2 k^2/2m_\text{r}$ is given by the energy of a free particle with reduced mass m_r in the limit of large particle separations $r \gg r_0$ with respect to the van der Waals

---

[2] The C_6 coefficient of Li is $1396 E_\text{h} a_0^6$, where $E_\text{h} = m_\text{e}e^4/4\epsilon_0^2 h^2$ is the Hartree energy [Gou16].

length. The total energy and wavenumber is conserved in the elastic collision process allowing only a phase shift of the outgoing wavefunction. The total wavefunction is then a sum of the incoming and outgoing wavefuntion:

$$\psi_{\mathbf{k}}(\mathbf{r}) = \psi_{\text{in}}(\mathbf{r}) + \psi_{\text{out}}(\mathbf{r}) \sim e^{i\mathbf{k}\cdot\mathbf{r}} + f(\mathbf{k}, \mathbf{k}')\frac{e^{ikr}}{r}, \tag{3.7}$$

where we have introduced the scattering amplitude $f(\mathbf{k}, \mathbf{k}')$ which describes an incoming plane wave with wavevector $k = |\boldsymbol{k}|$ scattered into a direction $\mathbf{k}' = k\mathbf{r}/r$.

Since the interaction potential is central symmetric we can expand the ansatz wavefunction in eq. (3.7) in partial waves. The wave function is then expressed in terms of Legendre polynomials. Within this partial wave expansion, it becomes clear that all states with angular momentum $l > 0$ do not contribute to a phase shift due to the centrifugal barrier and can therefore be neglected. Hence, the only relevant contribution stems from the s-wave ($l = 0$) term, resulting in the final scattering amplitude

$$f(k, \theta) = \frac{1}{k/\tan\delta_0 - ik} \simeq \frac{1}{-1/a + r_{\text{eff}}k^2/2 - ik}, \tag{3.8}$$

where θ is the angle between the incoming and outgoing plane wave, a is the scattering length, δ_0 is the phase shift from the s-wave contribution and r_{eff} is the effective range. In the case of ^{6}Li the effective range is $r_{\text{eff}} = 87a_0$ and can be omitted throughout the scope of this thesis [Zür12b]. Let us consider two particularly interesting cases. The limit $k|a| \ll 1$ results in a scattering amplitude $f = -1/a$, thus the scattering process is independent on the momentum and fully determined by the scattering length a. Another limiting case is $k|a| \gg 1$, in which $f = i/k$. This is known as the unitary limit discussed later in the section on Feshbach resonances.

We can further simplify the scattering problem in case that the de-Broglie wavelength $2\pi/k$ of the constituents is significantly larger than the inter-atomic length scale $r_0 \gg 1/k$. The most rudimentary approximation is to replace the interaction potential by a δ-potential, which however turns out to be an accurate description. The interaction strength of the δ-potential

$$V(r) = g\delta(r) \tag{3.9}$$

is quantified by the coupling constant $g = 4\pi\hbar^2 a/m_{\text{r}}$. This interaction potential is also referred to as *contact interactions* since the particles only interact with each other when their relative distance is zero. All the short-range physics covered in the inter-atomic potential is neglected, the only relevant information is the phase shift imprinted on the outgoing wavefunction during the collision.

The interpretation of contact interactions becomes important in the last chapter 6, where the relative wavefunction of two particles exhibits a node at zero relative distance. In a physical picture, this means that the probability to detect the particles on top of each other vanishes, leading to a non-interacting state of the two particles.

3.4.2 Feshbach resonances

Feshbach resonances are a remarkable experimental tool to tune the scattering properties of ultracold atomic gases by orders of magnitude with an extraordinary degree of control [Chi10; Ket08]. On general grounds, Feshbach resonances occur when the energy of two colliding atoms is close to the bound state energy of a molecule. The energy of the molecular bound state can be varied with respect to the energy of the unbound atoms via an external magnetic field, if their magnetic moments differ. This is called a *magnetically tuned* Feshbach resonance.

The underlying mechanism is the interaction of the magnetic moment $\boldsymbol{\mu}$ of the atom with an external magnetic field $\boldsymbol{B}$, leading to the effective Zeeman Hamiltonian $\mathcal{H} = -\boldsymbol{\mu} \cdot \mathbf{B}$. In the limit of large magnetic fields (which in the case of ^{6}Li is reached for fields of a few Gauss), this results in energy shifts with respect to zero magnetic field

$$\Delta E = \frac{\mu_\mathrm{B}}{\hbar} \left(g_\mathrm{J} m_\mathrm{J} + g_\mathrm{I} m_\mathrm{I} \right) B, \tag{3.10}$$

where g_J (g_I) is the Landé g-factor of the electron (nucleus), μ_B is the Bohr magneton. The external magnetic field is strong enough to decouple the magnetic moment of the electron and the nucleus such that they can be treated independently.

The Feshbach resonance can be understood within the model of two molecular potentials, illustrated in Fig. 3.3a. The open channel represents the scattering potential of two free atoms which collide in the gas with an energy E. A resonance occurs when a bound state within the closed channel approaches the same energy as the colliding particles in the open channel. The scattering atoms virtually couple to the bound state before they separate into free atoms after the scattering event. In this situation, even a small coupling between the closed and open channel strongly affects the phase of wavefunction.

The scattering length around the broad Feshbach resonance in ^{6}Li can be described by a relatively simple model [Chi10]

$$a_\mathrm{3D} = a_\mathrm{bg} \left(1 - \frac{\Delta B}{B - B_0} \right), \tag{3.11}$$

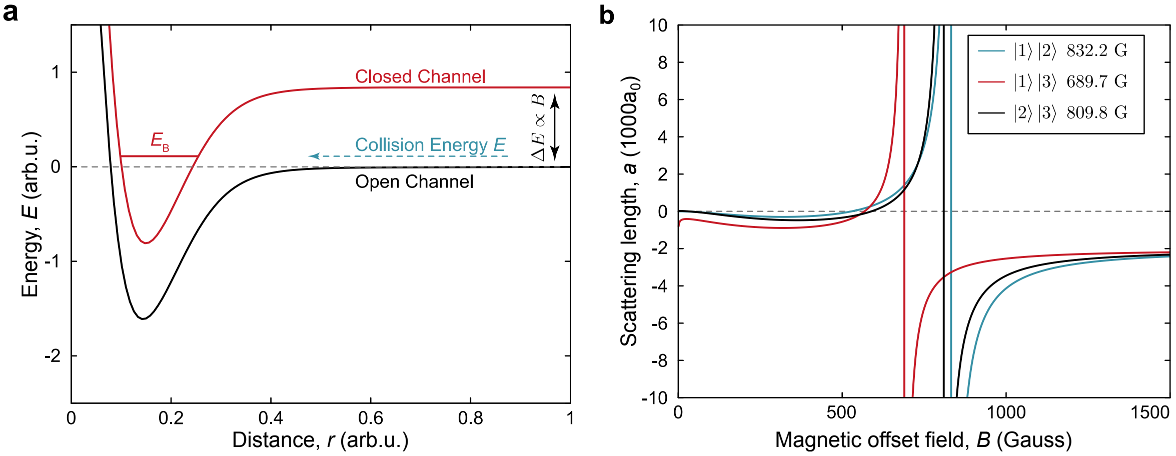

Figure 3.3: Feshbach resonance in ^{6}Li. **a**, A Feshbach resonance occurs if the collisional energy of two particles in an open channel can be tuned into resonance with the energy of a bound state E_{B} in a forbidden closed channel. The energy of the bound states is proportional to an external magnetic field. **b**, Tunable scattering length of all combinations of the three lowest hyperfine states. The interactions can be tuned from $\pm\infty$ to 0. Adapted from [Hol22].

with the background scattering length a_{bg} of the open channel, the position of the Feshbach resonance B_0 and the width ΔB. The Feshbach resonances in ^{6}Li were measured for all three hyperfine mixtures [Zür12a], and are shown in Fig. 3.3b. Throughout this thesis, we work with a $|1\rangle, |3\rangle$ mixture for which $a_{\mathrm{bg}} = -1770a_0$, $B = 689.7\,\mathrm{G}$ and $\Delta B = -166.6\,\mathrm{G}$. An important point is the *zero crossing* of the scattering length which results in a completely non-interacting hyperfine mixture at the field $B = B_0 + \Delta B$.

3.4.3 Two interacting particles in a harmonic potential

The interactions between two atoms trapped in a confining potential deviate from those in free space. The level spectrum of two interacting atoms in harmonic potentials in various dimensions have been explored in previous studies [Bus98; Ols98; Ber03; Idz05; Idz06]. While our optical trap can be approximated by a one-dimensional harmonic potential with an aspect ratio $\eta = \omega/\omega_{\mathrm{z}}$ for small atom numbers occupying the ground state, we also consider excitations to higher lying radial states, e.g. by rotating the atoms, which necessitates to include all three dimensions. We provide a short introduction into the derivation of the energy of two particles with respect to the scattering length, following [Idz06].

We consider two interacting particles 1 and 2 in an axially symmetric harmonic trap such that the Hamiltonian reads

$$\mathcal{H} = -\frac{\hbar^2}{2m}\nabla_1^2 - \frac{\hbar^2}{2m}\nabla_2^2 + V_\mathrm{t}(\boldsymbol{r}_1) + V_\mathrm{t}(\boldsymbol{r}_2) + V_\mathrm{i}(\boldsymbol{r}_1 - \boldsymbol{r}_2), \tag{3.12}$$

where the the trapping potential is given by

$$V_\mathrm{t}(\boldsymbol{r}) = \frac{m}{2}\left(\omega r^2 + \omega_\mathrm{z} z^2\right), \tag{3.13}$$

and the interacting potential V_i is translational invariant according to eq. (3.9). Note that the mass m of both particles is the same since in our case they only differ in their hyperfine state.

The center-of-mass $\boldsymbol{R} = (\boldsymbol{r_1} + \boldsymbol{r_2})/2$ and relative $\boldsymbol{r} = \boldsymbol{r_1} - \boldsymbol{r_2}$ motion decouple in a harmonic potential such that the Hamiltonian can be separated in

$$\mathcal{H}_\mathrm{com} = -\frac{\hbar^2}{2m_\mathrm{tot}}\nabla_\mathrm{R}^2 + \frac{m_\mathrm{tot}}{m}V_\mathrm{t}(\boldsymbol{R}) \tag{3.14}$$

and

$$\mathcal{H}_\mathrm{rel} = -\frac{\hbar^2}{2m_\mathrm{r}}\nabla_\mathrm{r}^2 + \frac{m_\mathrm{r}}{m}V_\mathrm{t}(\boldsymbol{r}) + g\delta(\boldsymbol{r})\frac{\partial}{\partial r}\boldsymbol{r}, \tag{3.15}$$

with the total $m_\mathrm{tot} = 2m$ and relative $m_\mathrm{r} = m/2$ mass. The center-of-mass degree of freedom is independent of the interaction potential and therefore solely resembles the equidistant energy levels of a harmonic oscillator. Hence, there will be many copies of the energy levels in the relative motion, spaced by the center-of-mass energies.

The energies and eigenfunctions of the relative motion are found by solving the time-independent Schrödinger equation, where the interacting wavefunction is expanded in the basis of harmonic oscillator states. This is examined in thorough detail in [Idz06], in which an implicit equation of the scattering length a and the energy $\mathcal{E} = E - E_0$ with respect to the ground state energy E_0 is derived, which reads

$$-\frac{1}{a} = \frac{1}{\sqrt{\pi}}\frac{\eta}{2\pi}\sum_{n=0}^{\infty}\left(\frac{\Gamma(-\mathcal{E}/2 + n\eta)}{\Gamma(\frac{1}{2} - \mathcal{E}/2 + n\eta)} - \frac{1}{\sqrt{\eta}\sqrt{n+1}}\right) + \frac{\sqrt{\eta}}{2\pi}\zeta\left(\frac{1}{2}\right), \tag{3.16}$$

where Γ is the Gamma Euler function and ζ is the Riemann zeta function. This expression holds for integer aspect ratios η. The energies are shown in Fig. 3.4.

Since we have a cigar-shaped trap with a tighter confinement in the radial than in the axial direction $\omega/\omega_z \approx 7$, there are many axially excited levels in the radial ground state. Furthermore, many axially excited energy levels of the Feshbach molecule in the

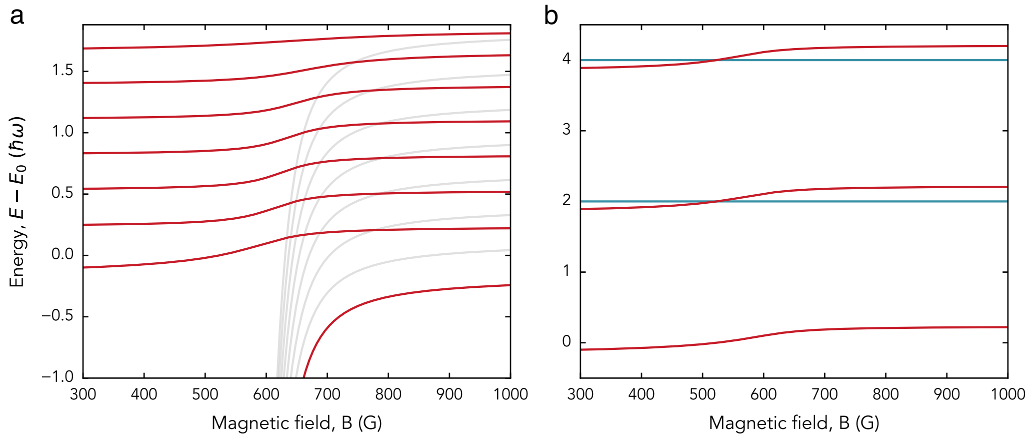

Figure 3.4: Level spectrum of two interacting particles in a harmonic trap. The energies are calculated for a three-dimensional, cigar-shaped harmonic potential with an aspect ratio $\omega/\omega_z = 7$, similar to the experimentally realized trap, according to eq. (3.16). The energy is shifted with respect to the energy E_0 of the non-interacting state at 568 G. **a**, Energy levels in the radial ground state (red) of two interacting fermions in terms of the magnetic field determined from eq. (3.11). In gray, the molecular branches with center-of-mass excitations in the axial direction are shown. In an anharmonic potential the energy crossings lead to energy gaps, and thus coupling between the levels. **b**, Relevant energy levels in the $0\hbar$, $2\hbar$, $4\hbar$ angular momentum manifold. All other energy levels are disregarded. The energy of the states with the relative degree of freedom in the ground state $m = 0$ (excited state $m > 0$) are shown in red (blue).

center-of-mass degree of freedom lead to level crossings in particular with the repulsive branch, i.e. the state with $-0.5 < E < 1.5$. In an anharmonic potential this leads to coupling to a Feshbach molecule when tuning the magnetic field from a non-interacting state at 568 G to a strongly repulsive state at 680 G.

In Fig. 3.4b, we show the relevant energy levels in the $0\hbar$, $2\hbar$, $4\hbar$ angular momentum manifold. States which remain in the ground state in the center-of-mass degree of freedom, i.e. their angular momentum quantum number in the relative degree of freedom is $m = 0$, tune their interactions with the magnetic field and thus lead to an energy shift (red). On the contrary, states with $m > 0$ remain constant (blue).

4

Experimental setup and techniques

This chapter summarizes the relevant experimental techniques to deterministically prepare ground state systems of few fermionic atoms in a tightly focused optical tweezer and to manipulate and detect their quantum state. For that, it is necessary to isolate the atoms from the environment in a vacuum chamber, to cool the atoms to quantum degeneracy by means of magnetic and optical trapping potentials and to manipulate their internal and motional degrees of freedom. A general overview on the production and probing of ultracold Fermi gases can be found in [Ket08], a detailed description of the experimental apparatus is given in previous PhD theses [Ser11b; Zür13; Ber17]. However during the course of this thesis, major changes regarding the microscope objective and the optical tweezer setup were implemented, which are documented here. The optical setup of the tweezers used for trapping and manipulating the atoms has been described in the recent master theses [Hil21; Rei23].

The chapter is divided in three main topics. The first part introduces the relevant experimental stages to prepare few-fermion systems. The second part focuses on the implementation of rotating optical potentials realized via the interference of Laguerre-Gaussian beams. The third part highlights the imaging techniques available in the apparatus for characterization of the quantum system.

4.1 Deterministic preparation of few-fermion systems

All the experiments described in this thesis are carried out in a vacuum chamber, shown in Fig. 4.1, at ultrahigh vacuum 1×10^{-11} mbar, which is necessary to reach a lifetime of tens of seconds for the atoms in the optical dipole traps. The titanium sublimator (1) and the ion pumps (2) provide the sufficient pumping strength to reach the high vacuum conditions. In order to achieve a degenerate sample of ^{6}Li atoms multiple cooling stages are required. The starting point is a collimated beam of lithium atoms exiting the oven at a temperature of $\sim 370\,^\circ\mathrm{C}$ (3). The atoms are slowed down in a 30 cm long Zeeman slower (4) and finally trapped in the stainless steel octagon (5).

The octagon enables optical access through six viewports in the horizontal plane with optical access of $NA = 0.15$ and two re-entrant viewports in the vertical direction with optical access $NA = 0.65$. The valves (6) are build in for separate access to the science chamber and the oven, in case lithium has to be refilled in the oven.

4.1.1 Zeeman slower and Magneto-optical trap

The first challenge to reach a degenerate Fermi gas is to slow the lithium atoms from a mean rms thermal velocity $v_{\mathrm{th}} = \sqrt{3k_{\mathrm{B}}T/m_{\mathrm{Li}}} \approx 1600\,\mathrm{m/s}$ at a temperature $T = 370\,°\mathrm{C}$ down to a few $0.01\,\mathrm{m/s}$. To this end, we use a Zeeman slower consisting of a magnetic field gradient along the propagation direction of the atoms and a counter-propagating laser beam resonant on the $D2$ line [Geh03]. Atoms that absorb a photon experience a directed momentum transfer $p = h/\lambda$ opposite to the propagation direction, resulting in a change of velocity of $\sim 0.1\,\mathrm{m/s}$. The resonance condition of the atoms changes with the velocity due the Doppler effect $\Delta\omega = kv$, where v corresponds to the velocity of the atoms. To account for the change in the resonance condition we apply a decreasing magnetic field with the minimum field at the science chamber.

At the final stage of the Zeeman slower the atoms reach a thermal velocity $v_{\mathrm{th}} \approx 50\,\mathrm{m/s}$ sufficiently slow to be captured in the magneto-optical trap (MOT). The MOT consists of three red-detuned, retro-reflected laser beams that apply a friction force on the atoms slowing them even further. Additionally with a magnetic field gradient provided by dedicated MOT-coils, the atoms are trapped spatially. Typical MOT loading times are $0.75\,\mathrm{s}$ limited by the speed of the mechanical ovenshutter. In the experiment, we use a pair of beams in each direction, named the *repumper* and *cooler* to close the optical transition between the $F = 3/2$ and $F = 1/2$ ground states [Geh03]. The lowest temperatures in the MOT are limited by the Doppler temperature $T_{\mathrm{D}} = h\Gamma/2k_{\mathrm{B}} \approx 140\,\mathrm{\mu K}$, given by the natural linewidth of the transition $\Gamma \approx 6\,\mathrm{MHz}$. These temperatures are still too high to reach quantum degeneracy requiring further cooling techniques.

4.1.2 Crossed optical dipole trap

We thus transfer the atoms from a compressed MOT to a crossed optical dipole trap (CODT) at a wavelength $\lambda = 1064\,\mathrm{nm}$, which is far-off resonant detuned to any optical transition. The CODT consists of two focused lasers beams that intersect at an angle of 14° resulting in a waist of $50\,\mathrm{\mu m}$ [Ber17]. At the latest stage of the transfer only the repumper beam is kept on to accumulate atoms in the $F = 1/2$ manifold. We then jump the magnetic field from $B = 0\,\mathrm{G}$ to $B = 795\,\mathrm{G}$ to accumulate atoms in the hyperfine mixture $|1\rangle$ and $|2\rangle$ at high magnetic field [Geh03]. We perform a $400\,\mathrm{ms}$ linear forced evaporation ramp within the CODT during which we apply an rf-pulse to create a

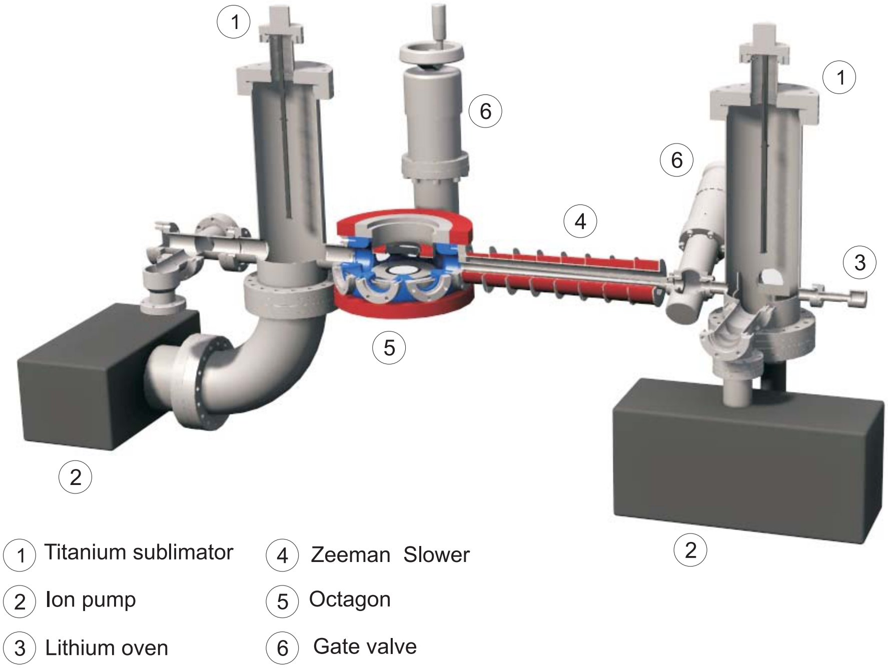

Figure 4.1: Vacuum chamber. Mechanical setup of the vacuum chamber. Taken from [Ser11b].

balanced hyperfine mixture. Subsequently, we transfer atoms from the hyperfine state $|2\rangle$ to $|3\rangle$ via a Landau-Zener passage at a magnetic field of 570 G. Depending on whether we work above or below the Feshbach resonance of ^{6}Li of the $|1\rangle, |3\rangle$ hyperfine mixture, we either jump to 800 G or 300 G, respectively. At this stage, we are left with 10^4 atoms in the CODT which are good starting conditions to load the atoms into our tightly focused optical tweezer.

4.1.3 High-NA objective

At the heart of the experiment lies the objective with a numerical aperture $NA = 0.55$, a focal length $f_{\text{obj}} = 20.3\,\text{mm}$, and an aperture size of 24.4 mm which serves two main purposes. First, it facilitates the generation of tightly focused optical tweezers on the µm size and second, it collects the fluorescence signal emitted by the atoms during the imaging. The implementation of the rotating optical tweezers required a new mounting system for the high-NA objective, sketched in Fig. 4.2.

The objective mount requires to meet the following criteria. The stability of the objective with respect to the vacuum chamber has the highest priority. This ensures

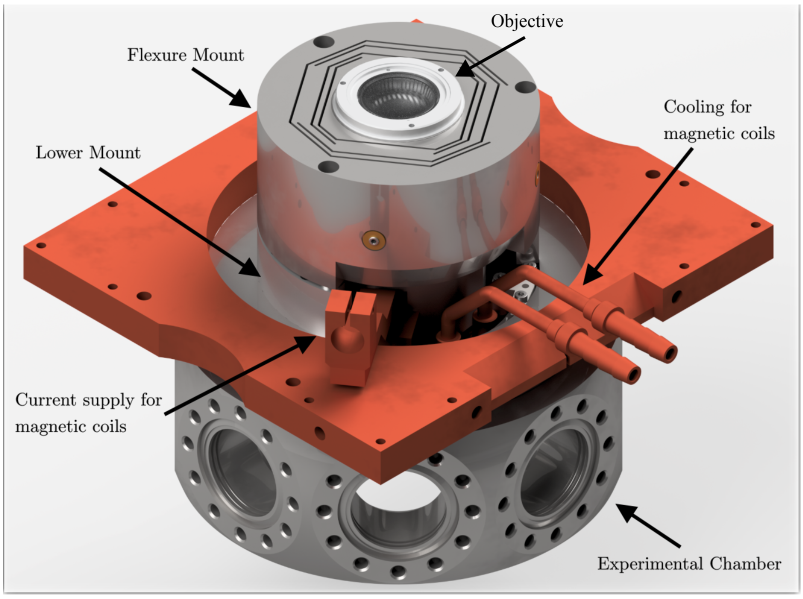

Figure 4.2: Objective mount. The objective is mounted in the flexure mount which is directly attached to the octagon on three contact points to adjust the height and the angle of the objective. The only kinematic degrees of freedom are the position in the horizontal direction. Optical elements (except the objective) are not shown for better visibility of the relevant components. Taken from [Dux].

stable positioning of the optical tweezers preferably on the nm scale, with high reproducibility. Furthermore, minimizing the degrees of freedom on the objective mount contributes to the overall stability. The only degrees of freedom required after the objective is mounted are the position in the horizontal plane enabled via a flexure mount to overlap the tweezer position with the magnetic field saddle of the Feshbach coils. The total adjustable distance in either axis is $\pm 0.5\,\mathrm{mm}$ with a resolution of $\sim 1\,\mu\mathrm{m}$ given by the $M4$ fine threaded screws. Crucial in the design of the flexure mount is the suppression of cross talk, both in the displacement of the axes and the change in the vertical angle. Simulating the flexure mount in *Autodesk Inventor 2021* yields an estimation on how severe the unavoidable cross-talk is, which turns out that for maximal displacements in either axis the tilt of the objective is $< 6\,\mu\mathrm{rad}$, the displacement in the perpendicular axis is $< 4\,\mu\mathrm{m}$, and the shift in the vertical direction is $< 3\,\mu\mathrm{m}$. The shifts are below the percent level and therefore negligible for the alignment procedure. More important is the coupling to the angle of the objective since a mismatch in the relative angle of the objective and the incoming light beam introduces optical aberra-

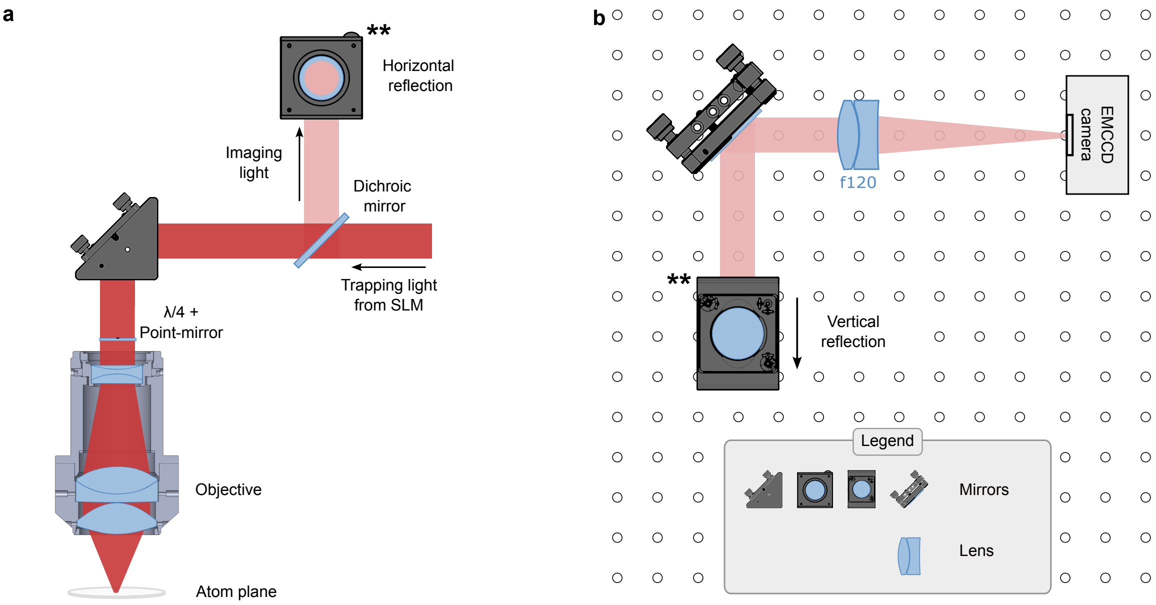

Figure 4.3: Optical path above the vacuum chamber. a, Optical path of the trapping and imaging light split by a dichroic mirror. Retro-reflection of the MOT beam is done via a so-called point-mirror, consisting of a 1 inch $\lambda/4$ waveplate with a 1 mm-diameter aluminium mirror sputtered on the center of the waveplate. **b,** Optical path of the imaging light focused on the *EMCCD* camera (from *NueVue*). The mirrors marked with $**$ in **a,b** are the same.

tions. The flexure mount is attached to a lower mount on a tripod. By using spacers between the flexure and lower mount, we adjust the angle and height of the objective with an accuracy of $\sim 1\,\mathrm{mrad}$ measured with an acceleration sensor on a precision of 0.25 mrad.

Above the objective we combine several optical components used for the MOT, for the generation of the rotating optical tweezers and the fluorescence imaging system, sketched in Fig. 4.3a.

Unlike the horizontal MOT beams, which are collimated on the atoms and retro-reflected using a standard Thorlabs mirror, the vertical MOT beam passes through the objective, leading to a divergent beam. Here, we focus the MOT beam with a lens system[1] close to the atoms which shifts the back-focal point slightly above the objective. At the position of the focus, we place a $\lambda/4$ waveplate with a 1 mm-diameter aluminium

---

[1] $f = 40\,\mathrm{mm}$ achromatic lens and $f = 150\,\mathrm{mm}$ spherical 1 inch Thorlabs lenses.

mirror (*point*-mirror) in the center of the waveplate to retro-reflect the beam on the atoms. The divergent MOT beam might result in lower MOT loading rate, however still sufficiently high for our purposes. On the contrary, we gain a compact optical setup for the MOT light with minimal distortion on the trapping and imaging light and without any additional mechanically moving elements in the setup. Note that the trapping and imaging light pass through the waveplate and thus the *point*-mirror as well. However, since we image small scale structures on the atoms and the objective acts as Fourier transformation, both the trapping and imaging light are on a large scale at the position of the *point*-mirror and therefore marginally affected.

The trapping and imaging light are combined via a dichroic mirror[2]. The imaging light is then reflected horizontally and focused with a $f_{\mathrm{EMCCD}} = 120\,\mathrm{mm}$ 2-inch sized lens on the *EMCCD* camera[3], shown in Fig. 4.3b. We make an image of the atom plane on the camera, with a magnification M determined by the ratio of the focal length of the objective and the focusing lens in front of the camera $M = f_{\mathrm{obj}}/f_{\mathrm{EMCCD}} \approx 6$. A single pixel on the camera has a size of $16\,\mu\mathrm{m}$ and thus corresponds to $2.7\,\mu\mathrm{m}$ in the atom plane. This is a compromise between resolving small scale structures in the atom plane – for which a large magnification is required – and collecting enough photons on a single pixel to discriminate the signal from the background noise – for which a small focal length is beneficial. A more detailed description of the imaging technique is given in section 4.4.

4.1.4 Optical tweezer setup

The new experimental tool in the optical setup is a spatial light modulator (SLM) [4] placed in the Fourier plane of the atoms. The general working principle is illustrated in Fig. 4.4. The SLM consists of 800×600 liquid crystals with a size of $20\,\mu\mathrm{m}$. The crystal's orientation alters the refractive index, allowing the imprint of a spatially varying phase $\phi(x, y)$ on the reflected light field

$$u_{\mathrm{out}}(x, y) = e^{i\phi(x,y)} u_{\mathrm{in}}(x, y) \tag{4.1}$$

given the local control of each crystal. By utilizing an optical lens which performs a Fourier transformation in its focal plane we can generate almost arbitrary intensity patterns. Details on the principles and characterization of the SLM can be found in [Hol17; Pal18; Hil21].

Using the Fourier transformation of the light field – instead of alternative applications where an SLM is set up in the image plane of the atoms – has the advantage that

---

[2] Laser components, HT10664nm, HR671nm

[3] NüVü Hnü 512

[4] Hamamatsu X10468-03 Liquid Crystal on Silicon (LCoS)

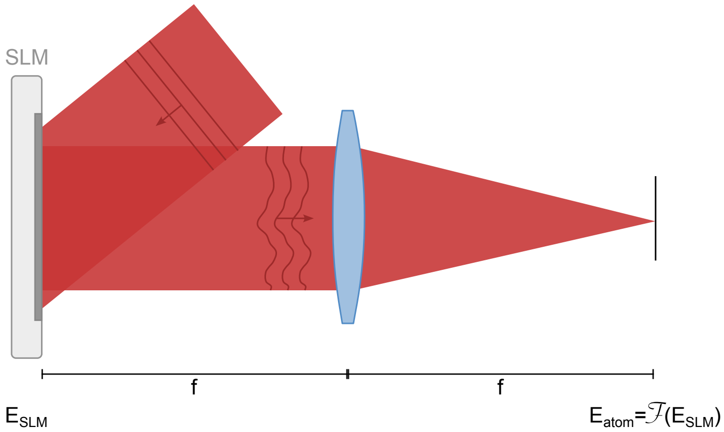

Figure 4.4: Spatial light modulator. The SLM imprints a locally varying phase $\phi(x, y)$ on the flat incident wavefront. Arbitrary intensity distributions can be generated by Fourier transformation of the light field via a lens. Adapted from [Pal20].

aberrations of the optical potential can be corrected at the resolution limit. Furthermore, the diffractive nature of the SLM renders it possible to generate multiple beams with different spatially varying phases. We make use of this to generate rotating optical potentials, discussed in the next sections.

The complete optical setup for the SLM is shown in Fig. 4.5. In our approach for creating rotating optical potentials, we use two beams from the SLM that interfere with each other. Beam 1 serves as the main optical tweezer in which we prepare the few fermion systems. This beam generates a Gaussian optical potential with minimal optical aberrations corrected with the aid of the SLM [Rei23]. Beam 2 is shaped to a Laguerre-Gaussian mode using the SLM. Its optical frequency relative to beam 1 is adjustable via an acousto-optical modulator (AOM) such that the deformation of the optical potential caused by the interference of the two beams can be rotated (details in the next section).

For the preparation of the tailored optical potentials, we clean the polarization and power stabilize the Beams on a photodiode (PD). Beam 1 and 2 are combined via a non-polarizing beam splitter (NPBS). Both beams are aligned on the SLM via a non-PBS on a 90° angle. This setup has the drawback of loosing at least 75 % of the light after the SLM but decreases the beam length tremendously, and hence increasing the beam pointing stability. We use a circular aperture in the Fourier plane of the SLM to remove unwanted diffraction orders, after which we magnify the Beams to match the aperture size of the objective. We install an additional camera in front of the objective

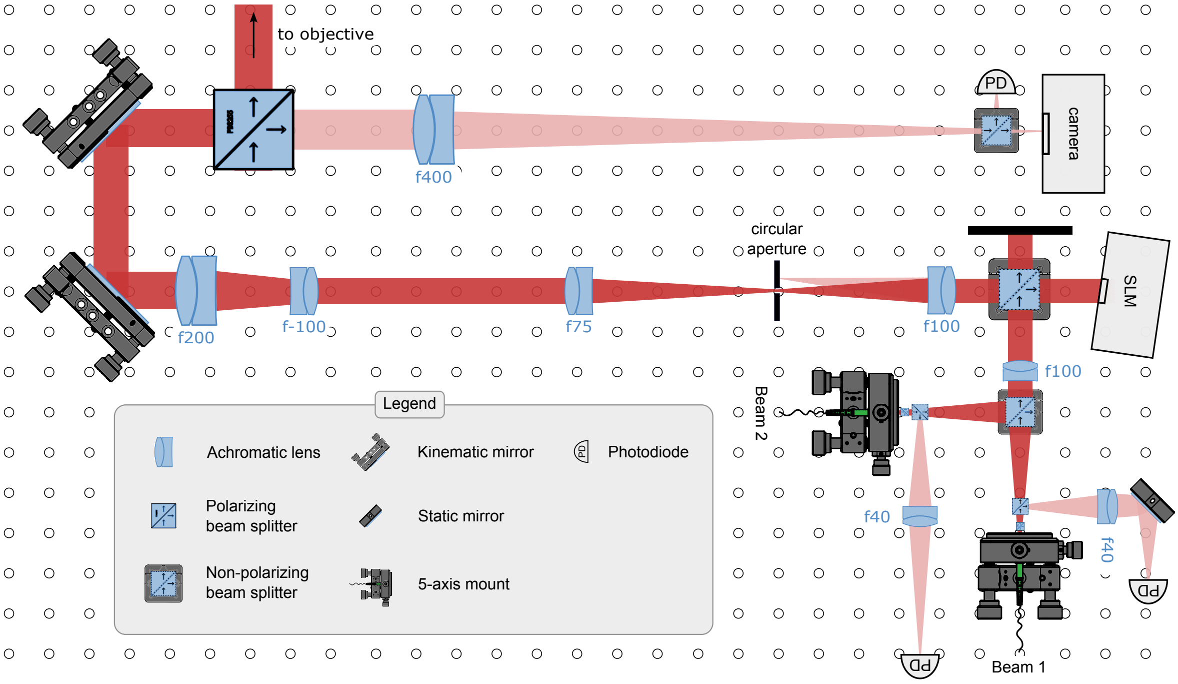

Figure 4.5: Optical setup. Optical setup to create tailored optical potentials via a spatial light modulator (SLM). The main optical tweezer is generated from Beam 1, while Beam 2 is used to deform the main tweezer with a precisely controllable rotation frequency.

to monitor the beam shape and the position of the beams generated by the SLM.

The central element of our experiment is a tightly focused optical tweezer with a waist of 1 µm, with which we prepare few-fermion systems with fidelities up to 95 %. First demonstrated in [Ser11a], it was refined to create multi-well systems [Ber19; Bec20a] and recently extended to 2D [Bay20a] by usage of an SLM. The small focus entails a drastic increase of the chemical potential, known as the dimple trick [Gri07], originally described in [Pin97; Sta98]. The small tweezer is superimposed with our CODT which serves as a large reservoir, from which the tweezer is filled with atoms through elastic collisions. Assuming thermal equilibrium between the large reservoir trap and the tweezer, this leads to a significant increase of the local density, the phase space density, elastic collision rate and T/T_F. In particular in our setup, we reach densities in the tweezer on the order of 10^{15}atoms/cm^3. These are excellent starting conditions for forced evaporative cooling to reach a cold sample of hundreds of fermions in the tweezer. We achieve that by ramping down the optical power quadratically by a factor of 20 within 40 ms. Additionally, during the transfer from the CODT to the

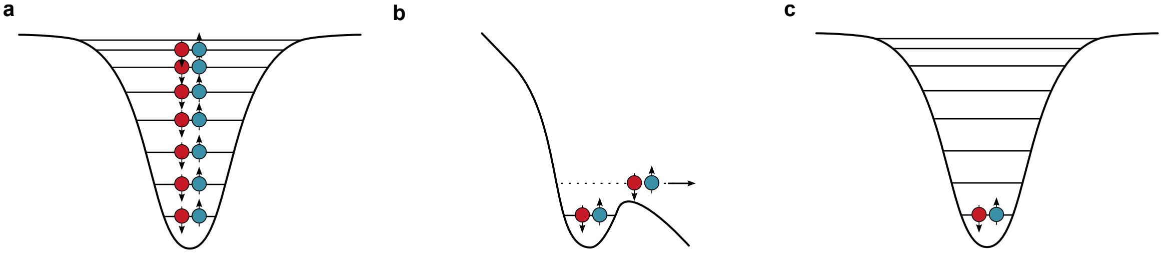

Figure 4.6: Deterministic preparation of few-fermion systems. The starting point is a degenerate, two-component Fermi gas of roughly 200 atoms in total in a tightly focused optical tweezer (a). Each energy level is occupied by two fermions differing in their spin degree of freedom. Applying a magnetic field gradient of 40 G/cm and lowering the trap depth removes all atoms above a certain energy threshold (b). We end up with a discrete quantum state in the ground state of the optical potential with variable atom number.

tweezer and the evaporation procedure, we turn on a magnetic field gradient of 40 G/cm to expel atoms with high kinetic energy.

In order to prepare few fermion systems, we start from a degenerate Fermi gas in the tweezer, illustrated in Fig. 4.6a. Subsequently, we apply a magnetic field gradient along the vertical direction, which corresponds to a linear potential in addition to the harmonic confinement given by the tweezer. As a result, depending on the strength of the gradient and the optical power in the tweezer, we can tune the number of bound states set by the large trap frequency (Fig. 4.6b). All atoms above a certain energy threshold are expelled from the trap, and after adiabatically turning off the magnetic field gradient we end up with a fixed number of fermions in the ground state of the optical potential (Fig. 4.6c).

Specifically, we start with a spin mixture in the hyperfine states $|1\rangle, |3\rangle$ of roughly 200 atoms in total, close to the ground state of the optical tweezer. We linearly ramp the magnetic field gradient to $\delta B/\delta z = 20\,\mathrm{G/cm}$ within 10 ms while keeping the tweezer power constant. After reaching the maximum gradient, we quadratically decrease the tweezer power within 80 ms and hold it for 40 ms to spill out the remaining atoms. We invert the sequence, leaving us with the desired atom number.

In Fig. 4.7, we show the experimental results on the preparation of mesosocpic Fermi systems. The upper row contains the variance, while the lower row displays the corresponding full counting statistics of the atom numbers. Within the lowest radial shell (**a,b**), the variance drops near zero accompanied by a step like occurrence of a particle number. In particular, we prepare the ground state of a single spin up and spin down

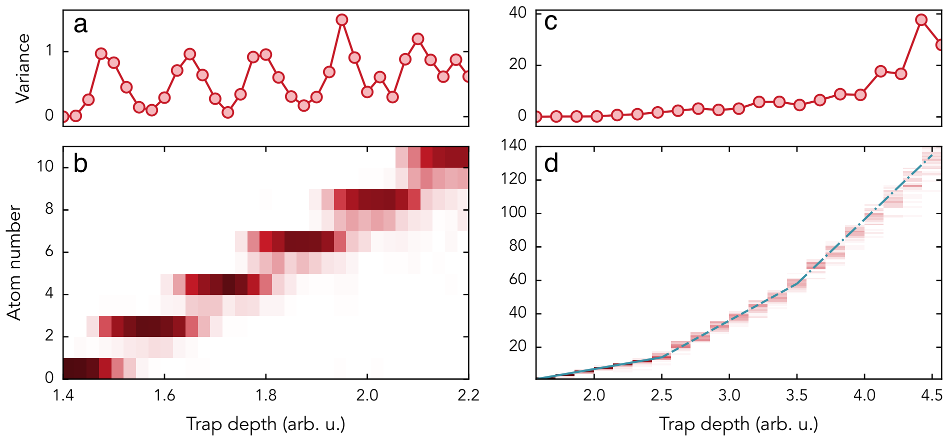

Figure 4.7: Experimental preparation of mesoscopic fermi systems. Variance **a**, and full counting statistics **b**, in the lowest radial shell are shown. Steps in the atom number counting are visible associated with a decrease in the variance to almost zero. The right column shows the variance **c**, and the full counting statistics **d**, of many fermions in the ground state extending to higher lying radial shells. The blue lines are linear slopes of the atom numbers corresponding to the density of states within each radial shell.

fermion with a fidelity of 95(3) % at an optical power of 136 µW above the objective. Note that the required optical power changes with the magnetic field gradient. As shown in [Ser11a], we can spill a second time to the same optical power to ensure that no excitations occur during the spilling procedure. The fidelity to spill two times is then given by the square of the single spill fidelity.

For larger atom numbers (**c,d**) we do not occupy the lowest radial shell and therefore near-deterministic preparation is not possible anymore given the degeneracy of the axial levels. However, the variance provides valuable information about the fluctuations in atom number. At a mean atom number of $N = 100$ atoms we observe a standard deviation $\mathrm{std} = \sqrt{\mathrm{var}(N)} = 4.2$ which is more than a factor 2 suppression in atom number fluctuations compared to the Poisson distribution $\sqrt{N} = 9.9$ expected for a thermal gas. Note that the atom number fluctuations is an upper bound as our method of counting the number of atoms cannot reliably discriminate between single atoms at these high atom numbers (see section 4.4 for details).

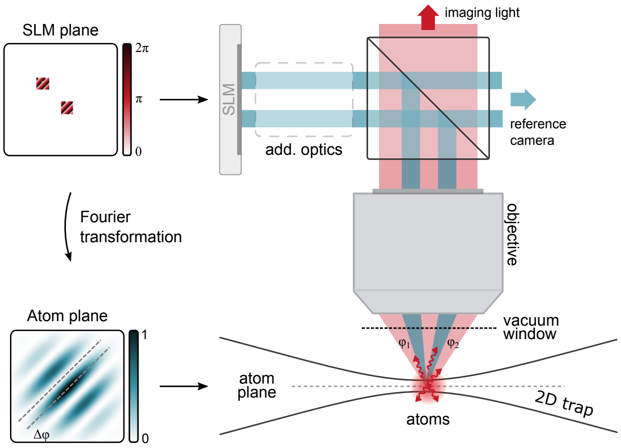

Figure 4.8: Phase shifting interferometry. Experimental setup for phase shifting interferometry (PSI). On the source, in our case an SLM, two patches are created, which interfere in the atom plane. The objective acts a a Fourier transformation. As the light stemming from the two patches travels through the optical elements they accumulate a different relative phase $\Delta\varphi$ if aberrations are present. This phase shift can be measured on a reference camera or on the atoms.

4.2 Correction of optical phase aberrations

High numerical aperture objectives enable access to the microscopic structures of quantum many-body systems, down to the single particle level [Kau21; Gro21a; Ber18]. In order to achieve such a small resolution the optical setup requires to be free of optical aberrations which limit the performance of the trapping and imaging system above the diffraction limit. Measuring the complete optical path turns out to be challenging, as the quantum gas is typically placed in a vacuum system with optical elements causing optical aberrations which are experimentally impractical to measure. This requires to use the quantum gas itself as a wavefront detector, to map out the optical aberrations from the source of the light field to the atoms. This section is partly based on the publication citeHill2024.

Phase shift interferometry (PSI) is an established technique to measure optical phase aberrations [Bru74]. The conceptual idea is to create two local patches on the source of the light field, in our case an SLM, sketched in Fig. 4.8. The light stemming from the two patches traverse through the optical elements along different paths, thereby accumulating different phases in the presence of optical aberrations. In the Fourier plane of the source, which is accessed through a focusing lens or an objective, the two patches overlap and interfere with each other. The spatial distance of the patches $|\boldsymbol{r}|$ at the source translates into an interference pattern with a fringe spacing given by the inverse of the initial spatial separation $1/|\boldsymbol{r}|$. In case that aberrations are present in the optical setup, they cause a path dependent relative phase shift of the patches $\Delta\varphi$, thereby shifting the position of the maxima (and minima) of the interference pattern. Thus, the shift of the interference pattern directly relates to the optical aberrations present in the optical system.

In order to experimentally realize the PSI algorithm by using the quantum gas as the wavefront sensor, we identify three key components. First, we require an SLM in the Fourier plane of the atoms used as the source of the light fields and for local manipulation. Second, a 2D confining potential is required which restricts the extend of the atoms along the vertical direction. Since we use small patches on the SLM, to increase the resolution of the phase map obtained by sampling the patches over the SLM, the Rayleigh length in the atom plane is large leading to a broad extend along the vertical direction. This is mitigated by the usage of the 2D trap. The third component consists of an imaging procedure to detect the atomic distribution along the optical axis.

We are concerned with the light field in the atom plane E_{atoms} stemming from the input field E_{SLM} on the SLM. Under the assumption that the SLM is in the Fourier plane of the atoms, and that we can approximate all the optical elements into an ideal lens with an effective focal lens f, the electric field amplitude in the atom plane takes the form

$$E_{\text{atoms}}(\boldsymbol{x}) \sim \mathcal{F}\left[|E_{\text{SLM}}(\boldsymbol{x}')|e^{iW(\boldsymbol{x}')}\right](\boldsymbol{\nu})\Big|_{\boldsymbol{\nu}=\boldsymbol{x}/\lambda f}, \tag{4.2}$$

where we have included all the local optical aberrations acquired by traversing through the optical elements into the wavefront $W(x')$. Hence, the aim is to measure $W(x')$ in the atom plane and imprint the inverse $-W(x')$ on the SLM to achieve a flat wavefront.

Consider two adjacent patches at positions $\boldsymbol{p}_1$ and $\boldsymbol{p}_2 = \boldsymbol{p}_1 + \boldsymbol{d}$, separated by a distance $|\boldsymbol{d}|$. We approximate the wavefront of each path to first order by $W(\boldsymbol{x}) = h_{\boldsymbol{p}_i} + \boldsymbol{g}_{\boldsymbol{p}_i} \cdot (\boldsymbol{x} - \boldsymbol{p}_i)$, where $h_{\boldsymbol{p}_i}$ is a constant phase and the $\boldsymbol{g}_{\boldsymbol{p}_i}$ corresponds to a linear phase gradient. Assuming a constant field amplitude E_{SLM}, we can use the approximative wavefront $W(\boldsymbol{x})$ to integrate Eq. (4.2). This yields an intensity distribution of the interference pattern in the atom plane

$$I(\boldsymbol{\nu}) = I_{\boldsymbol{p}_1} + I_{\boldsymbol{p}_2} + 2\sqrt{I_{\boldsymbol{p}_1} I_{\boldsymbol{p}_2}} \cos \Delta\Phi(\boldsymbol{\nu}) \tag{4.3a}$$

$$\Delta\Phi(\boldsymbol{\nu}) = 2\pi \boldsymbol{d} \cdot \boldsymbol{\nu} + \Delta\varphi, \tag{4.3b}$$

where $\Delta\varphi = \varphi_{\boldsymbol{p}_1} - \varphi_{\boldsymbol{p}_2}$ is the essential phase difference which determines the position of the central intensity peak of the interference pattern. The intensities $I_{\boldsymbol{p}_1}$, $I_{\boldsymbol{p}_2}$ are

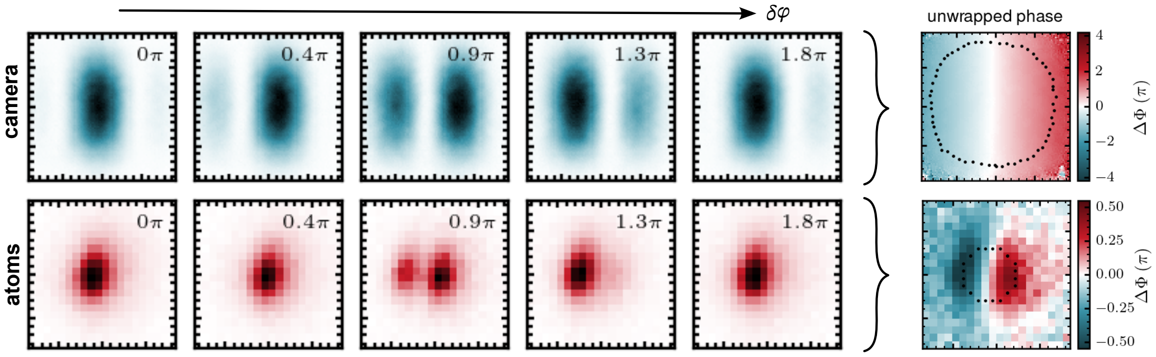

Figure 4.9: Phase sensitive intensity pattern. Interference pattern created from two patches on SLM, directly taking the light field on the reference camera (upper row, blue) and fluorescence images of the atomic distribution (lower row, red).

created from each patch, respectively, and are assumed to be homogeneous for small patch sizes.

In order to determine the phase $\Delta\varphi$ we perform phase shift interferometry, where we deliberately add a phase offset $\delta\varphi_\mathrm{n}$ between $2\pi n/N, n = 0, 1, ..., N-1$ to patch $\boldsymbol{p}_1$. This yields a periodic function in the intensity in the Fourier plane $I(\boldsymbol{\nu})$ with respect to the phase offset. Hence, we can Fourier decompose the intensity and directly retrieve the phase [Sch83]

$$\tan\Delta\Phi(\boldsymbol{\nu}) = \frac{\sum_{n=0}^{N-1} I_n(\boldsymbol{\nu})\sin\delta\varphi_n}{\sum_{n=0}^{N-1} I_n(\boldsymbol{\nu})\cos\delta\varphi_n}. \tag{4.4}$$

While in principle the phase $\Delta\phi$ can be extracted by fitting Eq. (4.3a) to the intensity signal of the atoms, the PSI algorithm offers a more general approach, since it does not rely on specific assumptions on the intensity distribution across the patches.

In Fig. 4.9, we show the interference patterns of two neighbouring patches aligned along the horizontal direction for multiple relative phase offset $\delta\varphi_\mathrm{n}$. The upper row contains the light intensity on the reference camera while the lower row displays the fluorescence signal of the atoms trapped in the interference pattern (details on the imaging scheme are found in section 4.4). As we increase the relative phase offset $\delta\varphi$ the node of the of central fringe moves along the horizontal direction, visible in both cases. Using Eq. (4.4), we determine the phase $\Delta\varphi$ by fitting a linear gradient to the unwrapped phase $\Delta\Phi$. We constrain the signal region in which the phase increases linearly by selecting only pixels above a certain intensity threshold. The signal region is highlighted with black dots in Fig. 4.9 in the right panel.

Let us emphasize that it in general, the fluorescence signal of the atomic distribution

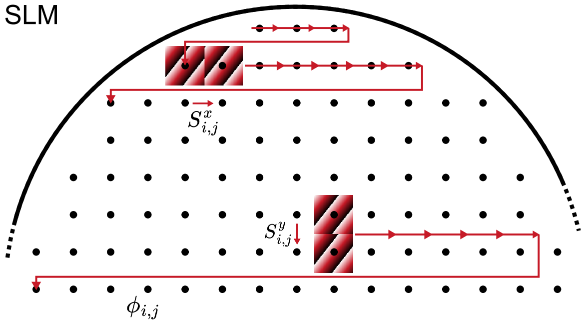

Figure 4.10: Shear maps. Neighbouring patches stacked along the horizontal and vertical direction are moved throughout the adjacent grid points on the SLM. The points correspond to the grid along which the patches are moved. The circle indicates the aperture of the objective.

is proportional to the distribution of the light intensity [Hil24]. Instead, a non-linear mapping is expected which is more pronounced in small atomic samples, where the local density approximation, i.e. where the chemical potential is approximated by $\mu(\boldsymbol{r}) = \mu - V(\boldsymbol{r})$, is not applicable. Furthermore, the temperature and the interactions might play an additional role on the distribution of the atoms. Moreover, during the imaging process the atoms perform a random walk which leads to broadening. Nevertheless, we observe that the atomic distribution follows the intensity distribution when the relative phase is varied, which justifies our approach.

The determination of the relative phase offset $\Delta\varphi$ of one pair of patches is the groundwork for the construction of the complete wavefront across the SLM. To this end, we use neighbouring patches along the horizontal and vertical direction, which are moved across the entire SLM, shown in Fig. 4.10. The reason to use neighbouring patches which move simultaneously is to maximize the fringe spacing in the atom plane. However, this measures not the relative phase offset but instead the shear of the phase along the respective direction. Alternative methods [Bru74] use a static reference patch with only a single moving patch from which the relative phase offset can be directly retrieved. This method requires sufficient resolution of the imaging system which is not accessible on the atoms.

To be precise, we measure the shear $S^x_{\mathrm{i,j}}$, $S^y_{\mathrm{i,j}}$ defined as

$$S^x_{\mathrm{i,j}} = \varphi_{i+1,j} - \varphi_{i,j} \tag{4.5a}$$

$$S^y_{\mathrm{i,j}} = \varphi_{i,j+1} - \varphi_{i,j}, \tag{4.5b}$$

along the $x-$ and $y-$direction, respectively, of patches located at $\boldsymbol{p} = (x_{\mathrm{i}}, y_{\mathrm{i}}) = (x_0, y_0) + (d_{\mathrm{i}}, d_{\mathrm{j}})$ and $(i, j = 0, ..., M-1)$. Here, $\varphi_{\boldsymbol{p}}$ corresponds to the absolute phase

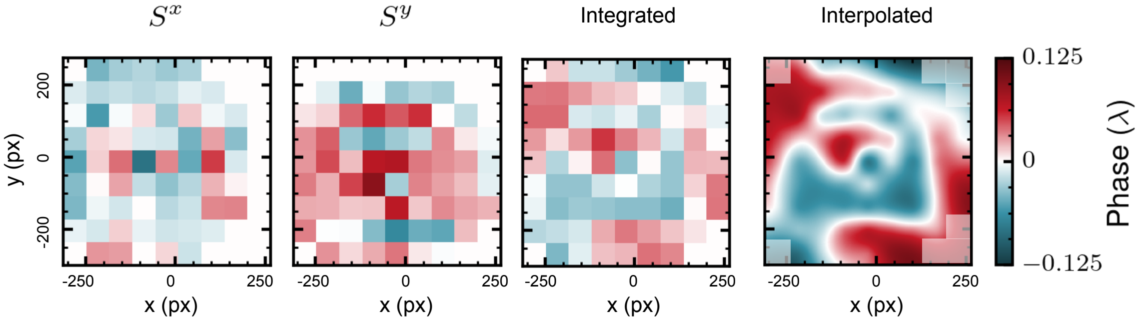

Figure 4.11: Wavefront flattening. Measured shear maps S^{x} and S^{y} in $x-$ and $y-$direction, respectively. The integration of the shear maps in both dimensions yields the coarse grained phase map which is interpolated using biharmonic splines to receive a smoothly varying phase map. The inverted phase map is imprinted on the SLM resulting in a flattened wavefront.

in the atom plane at the patch position $\boldsymbol{p}$. The shear map S^x is sampled on a grid with dimensions $M-1\times M$, while the shear map S^y is defined on the grid with size $M\times M-1$. In order to obtain the actual relative phase $\Delta\varphi$ we use least squares [Tal06] which minimizes the gradient of the phase map $\phi_{\mathrm{i,j}}$ with respect to the shear map along the $x-$ and $y-$direction

$$\min\left(\sum_{ij}(\phi_{i+1,j}-\phi_{i,j}-S^x_{ij})^2+\sum_{ij}(\phi_{i,j+1}-\phi_{i,j}-S^y_{ij})^2\right) \tag{4.6}$$

To retrieve the full phase map in the atom plane, we load ~ 100 ultracold atoms (the exact number varies among the patch positions) into the interference pattern formed by two neighbouring patches and image their density distribution. At each location on a 9×9 grid of the neighbouring patches with a patch size of 70 pixels (in comparison, the SLM contains 800×600 pixels, one pixel has a size of $20\times 20\,\mu\mathrm{m}$), we scan the relative phase offset $\delta\varphi_{\mathrm{n}}$ for six different phases. In each setting, we average around 20 fluorescence images of the atoms to increase the signal-to-noise ratio. From that, we end up with two shear maps S^x and S^y, shown in Fig. 4.11. Using the least squares, we retrieve the integrated phase map, which is subsequently interpolated. We invert the phase map, and display it on the SLM. We run the PSI algorithm multiple times to retrieve the phase map, which is then additionally displayed on the SLM. We observe that after three iterations the residual errors remain constant and conclude that the algorithm converged. The sum of all phase maps is shown in Fig. 4.11 on the right.

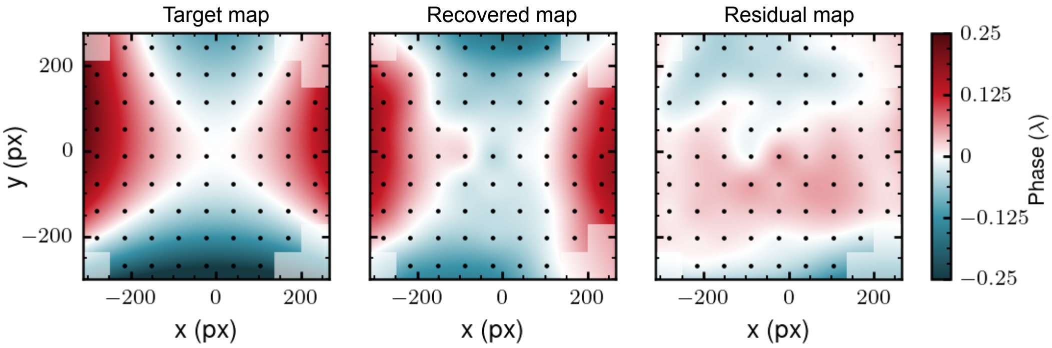

Figure 4.12: Benchmarking the PSI algorithm. We benchmark the PSI algorithm by applying a known erroneous phase map to the SLM consisting of a combination of coma and astigmatism. We run the PSI algorithm iteratively and recover a phase map close to the target one. The difference of the target and recovered phase map yields the residuals, which show a $\sigma_{\mathrm{rms}} = 0.03\lambda$ deviations.

Quantitatively, we calculate the root-mean-square (rms) deviation compared to a flat wavefront resulting in $\sigma_{\mathrm{rms}} = 0.05\,\lambda$. Furthermore, running multiple iterations on the atoms allows us to calculate the rms precision of the technique $\sigma_{\mathrm{rms}} = 0.01\,\lambda$ by comparing the difference of the rms deviation of the 3rd and 4th iteration. In that calculation, we exclude the outermost grids on the edges since they are clipped by the finite aperture size of the objective, marked as a shaded squares. Moreover on a qualitative level, we observe the structure of the point-mirror (for clarification, see Fig 4.3a)) at the center of the phase map. We emphasize that the obtained phase map includes the optical phase aberrations stemming primarily from the objective and the vacuum window. The aberrations caused by the optical elements between the SLM and the objective were cancelled on the reference camera before running the PSI algorithm on the atoms.

Having determined the precision of the PSI algorithm, the natural question arises how accurate it is. To this end, we apply a target map on the SLM which consists of coma and astigmatism aberrations, as these typically occur in optical systems. A crucial parameter is the peak-to-valley strength of the aberrations which is chosen to $\sigma_{\mathrm{ptv}} = 0.6\,\lambda$ – too strong and the aberrations render the PSI algorithm impossible on the atoms, too small and the signal-to-noise ratio is not sufficient to determine the target map. We measure in three iterations the shear maps in both $x-$ and $y-$direction, integrate them according to Eq. (4.6) and display the inverse on the SLM.

In Fig. 4.12, we show the target phase map, the sum of the recovered phase map and the residual map, which is calculated by the difference of the former maps. Qualitatively, we observe agreement between the target and recovered map in regions. The shaded regions are discarded since at these patch locations we do not trap any atoms in the interference pattern. Furthermore, in the center of the maps, we observe a mismatch due to the presence of the point-mirror (see Fig. 4.3a). On a quantitative level, we determine an rms deviation of the residual map $\sigma_{\mathrm{rms}} = 0.03\,\lambda$, by neglecting the shaded region, which is a factor of 3 larger than the rms-precision.

4.3 Implementation of rotating optical potentials

Many roads lead to rotation. Over the last decades various methods have been successfully implemented to rotate ultracold bosonic gases close to the deconfinement limit, by using either magnetic traps [Sch04; Fle21], optical lattices [Gem10] or a combination of a magnetic trap and a rotating elliptic optical potential [Bre04]. Strongly interacting fermionic atoms of lithium require trapping in optical potentials which often suffer from optical aberrations, specifically when using small focal waists on the µm scale. Rotating optical traps have been employed to reveal superfluidity in strongly interacting Fermi gases [Zwi05; Rie10], however reaching the rapid rotation limit without heating the system has been elusive so far. Here, we overcome these challenges and use an all-optical approach to smoothly rotate our tweezer up to arbitrary rotation frequencies. In this section, we highlight the implementation of the rotating optical potentials.

The conceptual idea of our technique is based on the interference of Laguerre-Gaussian modes with different orbital angular momentum. They are characterized by a radial and azimuthal index p and l, respectively, and read

$$\mathrm{LG}_{\mathrm{p}}^{l}(r,\varphi) = \frac{\sqrt{2}}{w_0}\sqrt{\frac{p!}{\pi(|l|+p)!}}\left(\frac{\sqrt{2}r}{w_0}\right)^{|l|}\mathrm{L}_{\mathrm{p}}^{|l|}(2r^2/w_0)e^{il\varphi}e^{-r^2/w_0^2}, \tag{4.7}$$

where w_0 is the waist of the laser beam in the focal plane, and $L_{\mathrm{p}}^{|l|}$ are the associated Legendre polynomials. The phase winding of the LG mode is given by $e^{il\varphi}$, thus carrying l quanta of angular momentum resulting in a node in the intensity distribution. Superimposing two LG modes does not lead to rotation, yet; it also requires the temporal control of the relative phase. Changing the phase continuously is equivalent to a relative frequency offset between the two beams. To accomplish this, we use an AOM for each beam, allowing us to set the relative frequency to arbitrary values via a frequency generator[5].

To approximate a harmonic potential with the tweezer we choose the zeroth order LG mode corresponding to a flat phase $\phi(x, y) = 0$ on the SLM. In order to generate

---

[5] Rigol DG4162

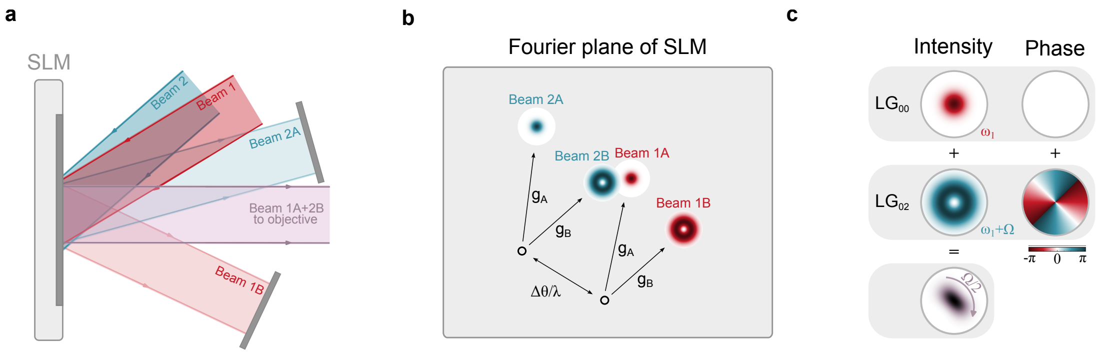

Figure 4.13: Implementation of rotating optical potentials. **a**, The SLM is used to generate two diffraction patterns from a single incident beam, generating in total four outgoing beams, two of which are overlapped by adjusting the gradients $\mathbf{g}_\text{A}$, $\mathbf{g}_\text{B}$. **b**, Position of the four outgoing beams in the Fourier plane, slightly displaced due to an offset in the angle. Gradient A (B) diffracts a LG_{00} (LG_{02}) mode. The black circles indicate the position of the outgoing beams if no gradient is applied on the SLM. **c**, The phase pattern on gradient A and B can be adjusted independently. A Gaussian mode is chosen for Beam 1A and a $l = 2$ Laguerre-Gaussian mode is selected for Beam 2B. Interference of the beams deforms the optical potential elliptically. The relative frequency Ω of the beams determines the rotation frequency Ω/l.

a higher order LG mode, we imprint a phase winding

$$\phi(x, y) = l \arctan(x, y) = l\varphi, \tag{4.8}$$

of l-th order on the SLM depending on the amount of angular momentum we intend to imprint on the atoms. Here, φ corresponds to the angle in polar coordinates. The Fourier transformation of the above phase pattern then yields a LG_{0l} mode in the atom plane.

In Fig. 4.13, we illustrate the generation of two interfering beams by utilizing the SLM. To this end, two incident Beams 1 (red) and 2 (blue) are shone on the SLM under a small relative angle $\Delta\theta$ (see Fig. 4.13a). In order to individually modify the local phase of each beam, we generate multiple outgoing beams from a single source by choosing the phase pattern

$$\phi(x, y) = \arg\left(e^{i\phi_\text{A}(x,y)} + e^{i\phi_\text{B}(x,y)}\right) \tag{4.9}$$

on the SLM. This yields approximately an outgoing electric field amplitude

$$u_{\mathrm{out}}(x,y) \simeq (e^{i\phi_{\mathrm{A}}} + e^{i\phi_{\mathrm{B}}})u_{\mathrm{in}}, \tag{4.10}$$

which consists exactly of two beams reflected with an angle given by the phase gradient ϕ_{A} and ϕ_{B}. Note that this contrasts the situation where simply a sum of two phase gradients $\phi_{\mathrm{A}} + \phi_{\mathrm{B}}$ is applied to the SLM which results in the outgoing amplitude $u_{\mathrm{out}} \simeq e^{i(\phi_{\mathrm{A}}+\phi_{\mathrm{B}})}u_{\mathrm{in}}$ corresponding only to a single outgoing beam.

The outgoing angle of the beams in eq. (4.10) can be adjusted by the phase gradients g_{A}, g_{B} which create the sub-beams A, B. To compensate for the initial relative angle $\Delta\theta$, the gradients are set to $\Delta\theta = (g_{\mathrm{A}} - g_{\mathrm{B}})/\lambda$ which aligns two out of the four beams on top of each other. This scenario is illustrated in Fig. 4.13b, where the beams overlap ever so slightly. Here, we also imprinted a LG_{00} (LG_{02}) mode on gradient A (B).

In Fig. 4.13c, we calculate the interference of a LG_{00} and LG_{02} mode in the limit of small relative intensity of the latter one. Even though the intensity pattern of both beams is radially symmetric, the interference pattern deforms to an ellipse. This becomes evident when considering the phase of each beam. While the LG_{00} mode has a flat phase the LG_{02} has $2 \times 2\pi$ phase windings leading to constructive and destructive interference along perpendicular axes. The relative frequency Ω of the two beams sets the rotation frequency which is adjustable via a single AOM for each beam. However, the *real* geometric frequency at which the optical potential rotates is $\Omega/l = \Omega/2$ which is reflected in the 2-fold symmetry of the perturbation – after 1/2th of a period the perturbed potential is mapped back on itself.

4.4 Imaging techniques

Imaging the atomic system gives access to crucial information required to characterize the quantum state. In contrast to quantum non-demolition imaging techniques which rely on the atoms imprinting a phase shift on the incident light field [Ket99], we employ measurements which destroy the initial quantum state. Within the scope of this thesis we mainly utilize two methods. The first one counts the number of atoms with high fidelity [Hum13] which allows us to characterize the system spectroscopically. The second one employs a single atom and spin resolved fluorescence imaging technique [Ber18] which projects the quantum state on the momentum of each particle. To extract information about the system we prepare the exact same quantum state many times and reconstruct various observables from statistics.

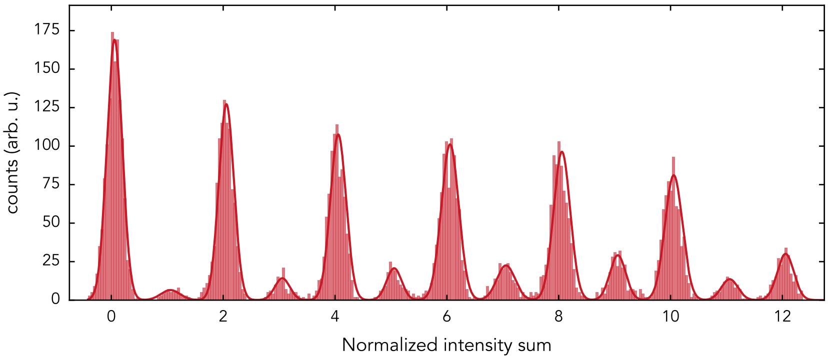

Figure 4.14: Histogram of fluorescence signal of few atoms. Single atoms can be distinguished via the large separation of their normalized fluorescence signal, with an average peak separation of 6.7σ for the displayed atom numbers. The envelope corresponds to Gaussian fits which scale linearly with the fluorescence signal of increasing atom numbers.

4.4.1 Atom number counting

A prerequisite for any measurements in our few fermion systems is the detection of atoms at the single particle level. To this end, we use an atom number counting technique [Ser11a; Hum13] where the atoms are recaptured from the tweezer into the MOT. In order to increase the emitted fluorescence of the atoms in the MOT, we ramp the detuning $\Delta = -2\Gamma$ close to resonance and increase the magnetic field gradient to 250 G/cm to localize the particles tightly. The fluorescence signal is then focused on a CCD camera and integrated over 500 ms, which experimentally turned out to be an optimal integration time to reliably discriminate single atoms. With these settings we achieve a large separation of the fluorescence signals of different atom numbers up to range of 12 atoms, shown in Fig. 4.14, already normalized to the mean intensity of single atom. Assuming a Gaussian distribution of the fluorescence signal, the separation of the peaks is on average 6.7σ and, within the displayed atom numbers, scales linearly with the single atom intensity.

The high counting fidelities come at the cost of losing information about the position, the momentum and the spin state of the particles. It is however possible to access information about the energy of the particles within the trap by probing the system spectroscopically. This situation is sketched in Fig. 4.15. Typically, we start with two non-interacting spinful fermions in the ground state of the optical tweezer. Subsequently, we perturb the system at a given frequency Ω for a certain perturbation time τ_p after which we spill again to the same energy level of the ground state, thereby

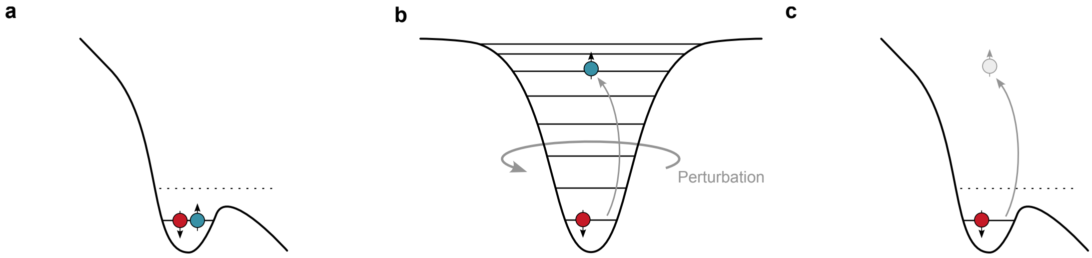

Figure 4.15: Atom loss spectroscopy. The two spinful fermions in the ground state of the optical potential (**a**) are characterized by perturbing the system (**b**, typically a rotation of the deformed optical potential) and subsequent counting of the remaining atoms in the ground state (**c**).

removing all excited atoms.

The perturbation can take various forms, ranging from amplitude modulation of the optical power of the tweezer to Laguerre-Gaussian modes LG_{0l} of different orders l. The variety of perturbations allows us to selectively address specific motional states within the optical potential giving access to the complete potential landscape (see appendix A for details). We demonstrate this technique in chapter 5 by preparing different angular momentum eigenstates.

4.4.2 Spin and atom resolved fluorescence imaging

We make use of a single atom and spin resolved imaging technique pioneered in previous work [Ber18] to access correlations in momentum space. The conceptual idea is to illuminate the atoms with resonant light on a time scale that is short with respect to their velocity. The fluorescence light is then collected via the high-NA objective and focused on an EMCCD camera.

The schematics are sketched in Fig. 4.16a. Two alternating resonant laser pulses with a periodicity of 200 ns illuminate the atoms for 15 µs resulting in ~ 250 emitted photons from which we collect on average 24 photons given the numerical aperture $NA = 0.55$ of the objective, the radiation pattern of the atoms and the losses on the optical components. In order to discriminate a single atom from the background noise we employ an EMCCD camera, for details see [Jan16]. We achieve a gain over read-out noise $g/\sigma_{\text{read}} = 23$ with our camera. Choosing a 5σ detection threshold we reach single photon detection fidelities of $P = e^{-5\sigma_{\text{read}}/g} = 80\,\%$. When operating the camera in the electron multiplying mode the most dominant noise source are clock-induced charges (CICs) which are randomly generated photoelectrons during the read-out. For a successful detection of single atoms it is essential to operate in a regime where the

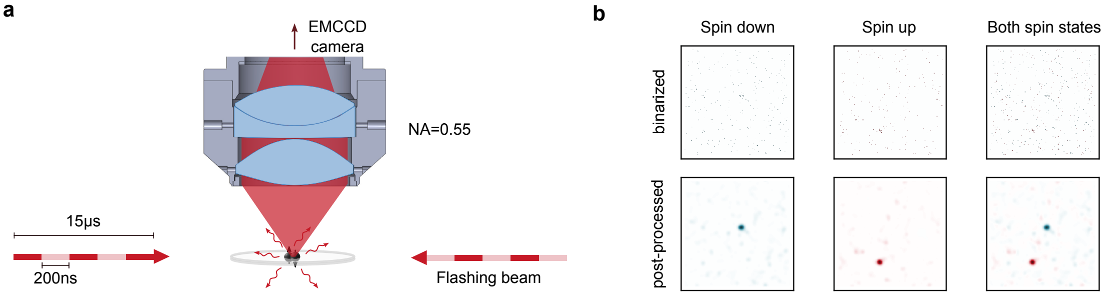

Figure 4.16: Single atom and spin resolved imaging. Two counter-propagating, resonant laser beams with alternating intensity are shone on the atoms. The fluorescence light is collected via the $NA = 0.55$ objective and focused on an EMCCD camera. The total imaging time of 15 µs is sufficiently long to collect enough photons to discriminate them from the background and short enough to limit the diffusion of the atoms, such that no cooling is required. Adapted from [Ber17].

CICs are as low as possible. Remaining background light in the experiment leads to an additional increase of randomly generated photoelectrons. In total, the probability to excite an unwanted photoelectron per pixel is in our case 0.3 % on a pixel size 320×320.

The detection of single atoms requires additional processing of the obtained raw images. We first binarize each pixel to one if the value is above the threshold of $5\sigma_{\text{read}}$, otherwise it is set to zero. Afterwards we use a low-pass filter with a Gaussian width of 5 pixels. This increases the signal of the atoms drastically as the photons emitted from the atoms cluster while the CICs are randomly distributed over the camera chip. The process is showcased in Fig. 4.16b for both a spin up (red) and spin down (blue) fermion. Finally, they are combined to a single image.

The *in-situ* imaging resolution σ_{I} is not sufficient to resolve the microscopic features of the wavefunction within the tweezer. Typically, we work with radial trap frequencies up to $\omega/2\pi = 50\,\text{kHz}$ resulting in a harmonic oscillator length $l_{\text{HO}} = 0.18\,\mu\text{m}$ which sets the natural length scale of the system. Due to the random walk caused by the recoil of the scattered photons during the imaging procedure, the diffusion of the atom position leads to an *in-situ* imaging resolution on the order of $\sim 10\,\mu\text{m}$, see Fig. 4.17, for the spin down state (blue) and the spin up state (red). Here, we image the spin down state directly after switching off the tweezer, and subsequently the spin up state with a time delay of 145 µs leading to an additional broadening. We observe a slight asymmetry in the $x-$ and $y-$direction which we attribute to stimulated emission along the direction of the flashing beams.

To circumvent the problem of the resolution, we use a time-of-flight expansion on

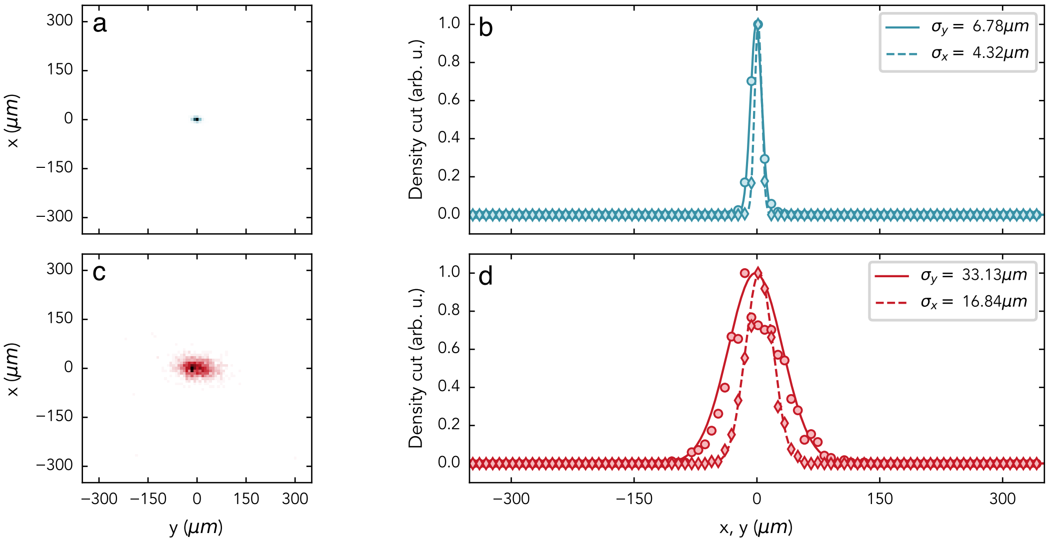

Figure 4.17: Effective imaging resolution. The in-situ imaging resolution is not sufficient to resolve any microscopic details of the wavefunction. The successive imaging of spin down (blue, **a**,**b**) and spin up (red, **c**,**d**) with a time delay of 145 µs leads to off-resonant scattering of the spin up state and thus an increase in the effective imaging resolution.

the order of $t_{\mathrm{tof}} = 2\,\mathrm{ms}$ which leads to a magnification $M = \omega t_{\mathrm{tof}} \sim 600$. The time-of-flight expansion maps the initial real space system to momentum space given that we are considering eigenstates of the 2D harmonic oscillator. This results in an effective imaging resolution in momentum space

$$\frac{\sigma_{\mathrm{p}}}{p_{\mathrm{HO}}} = \frac{\sigma_{\mathrm{l}}}{l_{\mathrm{HO}}} \frac{1}{M}, \tag{4.11}$$

in units of the harmonic oscillator momentum p_{HO}. Specifically, we obtain an effective imaging resolution in momentum space of the spin down state $2\sigma^{\mathrm{x}}_{\mathrm{p},\downarrow} \approx 0.08 p_{\mathrm{HO}}$, $2\sigma^{\mathrm{y}}_{\mathrm{p},\downarrow} \approx 0.13 p_{\mathrm{HO}}$ and the spin up state $\sigma^{\mathrm{x}}_{\mathrm{p},\uparrow} \approx 0.29 p_{\mathrm{HO}}$, $\sigma^{\mathrm{y}}_{\mathrm{p},\uparrow} \approx 0.57 p_{\mathrm{HO}}$. Note that the magnification of the spin up state is slightly larger due to the 145 µs time delay.

5

Engineering angular momentum states

In order to simulate complex quantum many-body systems with ultracold atoms, novel experimental approaches are required to engineer the desired Hamiltonians [Llo96; Geo14]. Optical dipole traps are particularly suited for this tasks as they allow the utilization of spatial light modulators (SLMs) to manipulate the optical potential locally, down to the diffraction limit [Bij13]. Nowadays, SLMs have become a standard technique in cold atom experiments to engineer Hamiltonians. These range from the Hubbard model [Gro21a], spin models in Rydberg systems [Bro20], homogeneous systems [Gau13; Muk17; Hue18], cosmological models [Vie22], to artificial gauge fields [Aid13b; Tai17], to name an incomplete list.

A long-standing goal in ultracold atom experiments has been the realization of strong artificial magnetic fields [Aid18; Gol16; Coo19; Coo08]. They enable a direct mapping to strongly correlated phases analogues to those in the FQH effect. Among various experimental techniques [Lin11; Cha20; Man15; Zho23; Str12; Aid14; Jot14; Ken15; Ast19], rotating ultracold atomic gases stand out due to the intuitive mathematical equivalence of the Coriolis force acting on a neutral particle and a charged particle exposed to the Lorentz force [Dal16]. From an experimental standpoint however, rotating a quantum system is a delicate process as, if not well controlled, it might lead to coupling to unwanted states which eventually heats the system. The exquisite control of the particle number, interactions and optical potentials in ultracold atomic gases allows for the examination of the simplest experimental systems to test the rotating perturbation for heating mechanisms, before exploring strongly correlated many-body phases with many particles.

In this chapter, we report on the preparation of a single fermionic atom in angular momentum eigenstates, trapped in a radially symmetric optical potential. These measurements are enabled by the precise control of the ellipticity of the optical tweezer, as well as a newly developed experimental technique to deform and rotate the optical potential. We demonstrate the preparation of angular momentum states by measuring the density of the wavefunction in momentum space after a time-of-flight expansion.

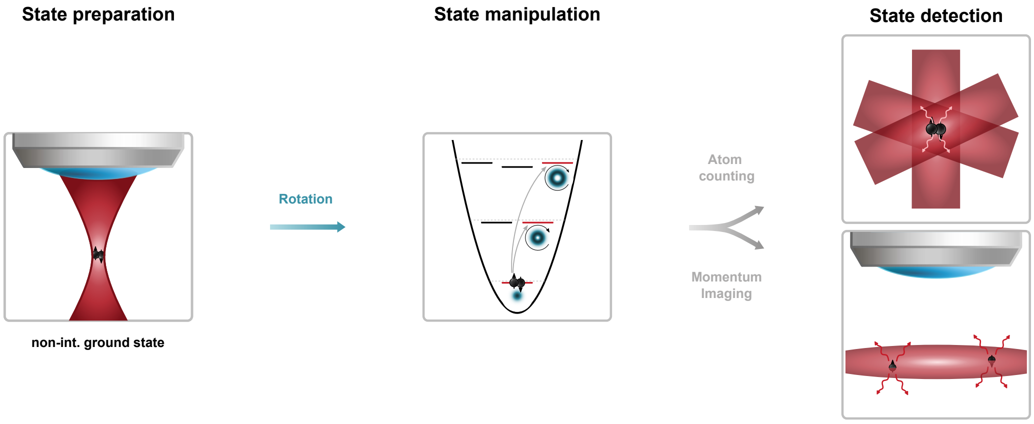

Figure 5.1: Experimental sequence for preparing angular momentum states. **a**, We prepare two spinful non-interacting fermions (black particles) in the ground state of a radially symmetric optical tweezer, tightly focused through a high-NA objective. **b**, The in-plane potential forms a two-dimensional harmonic oscillator up to anharmonic corrections. The rotating perturbation couples the stationary ground state to a state with $L_z = m\hbar$ angular momentum. These are states that carry maximal angular momentum in their respective shell n and lie in the LLL. **c**, We either spectroscopically characterize the prepared angular momentum state (1) or we use our imaging scheme to detect the momentum of each of the particles (2).

The incorporation of the angular momentum manifests in a radially symmetric density distribution with a depletion in the center. We further investigate the angular momentum eigenstates by letting the quantum state evolve in slightly anisotropic trap, thereby demonstrating the imprint of a phase winding. Most of the results presented in this chapter are based on the Supplementary material of the publication [Lun24].

5.1 Preparation of angular momentum states

Our approach to prepare a single fermion in an angular momentum eigenstate consists of three main steps, illustrated in Fig. 5.1. First, we start with two spinful fermions in the ground state of the optical tweezer at a magnetic field of 300 G where the atoms are still interacting. Subsequently, we adiabatically tune the magnetic field to 568 G at which interactions between the fermions are zero. We prepare this non-interacting state near-deterministically with fidelities of 95(3) %. Here, we can treat the two fermions as independent, identical copies of the same system. This allows us to effectively consider a single atom in the ground state of the optical potential and is the starting point of all experiments described in this chapter.

In the second step, we employ a rotating perturbation to couple the ground state to an angular momentum state. We imprint a LG mode of lth order for a varying time τ_{rot} on the atoms. This perturbation deforms the originally, rotationally symmetric optical tweezer and rotates at a frequency $\Omega/2\pi l$, where Ω is the difference of the optical frequencies between the light used to create the LG mode and the optical tweezer. The order l of the LG mode determines the amount of angular momentum inserted into the system. Furthermore, we make use of the anharmonicity of our optical potentials which renders the ground state and the desired angular momentum eigenstate an effective two-level system since coupling to higher states is suppressed. We then drive Rabi oscillations between these states, followed by a $\pi-$pulse to the angular momentum state.

The third step, following the state preparation, consists of the the state detection. We have two options in our experiment: we can either spectroscopically characterize the system, where we transfer atoms back to the MOT after applying the rotating perturbation and count the total number of remaining atoms in the ground state, or we can utilize our fluorescence imaging technique. The latter technique involves projecting the wavefunction with a momentum measurement on each of the spin states. The repeated preparation of the exact same quantum state allows us to re-construct the density of the wavefunction.

If not mentioned otherwise throughout this chapter, we will only detect the hyperfine state $|F = 3/2, m_{\text{F}} = -3/2\rangle$ (corresponding to $|\downarrow\rangle$) since the detection fidelity is significantly larger compared to the hyperfine state $|F = 1/2, m_{\text{F}} = 1/2\rangle$ (corresponding to $|\uparrow\rangle$) due to the closed imaging transition (see chapter 4) and the other one being only an identical copy.

5.1.1 Experimental caveats

Before studying the preparation and detection of angular momentum states, it is instructive to understand the experimental challenges of realizing such angular momentum states. We had to overcome several experimental obstacles.

Relative position of the main trap and the rotating perturbation beam. It is necessary to align the perturbation beam on the main optical tweezer with a precision that is on the same order of magnitude as the radial extend of the wavefunction, typically $\sim 200\,\text{nm}$, set by the tight radial confinement of the tweezer. Displacement of the perturbation beam and the main trap leads to unwanted coupling elements which might

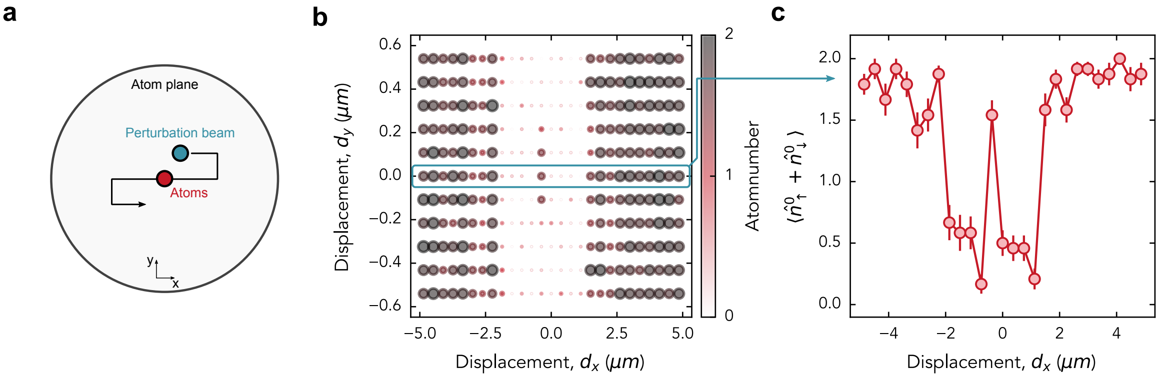

Figure 5.2: Alignment of the perturbation beam and main trap. **a**, Sketch of the alignment procedure. We choose a LG_{00} mode as the perturbation beam and scan it across the two-dimensional atom plane while modulating the intensity of the perturbation with the radial trap frequency. In the case of slight displacement of the perturbation and the main trap this leads to excitations of the atoms from the ground state. **b**, Excitation spectrum for various displacements of the perturbation beam with respect to the position of the atoms. **c**, Exemplary excitation spectrum at $d_y = 0\,\mu\mathrm{m}$. The coupling to the dipole mode is suppressed when the perturbation beam and the atoms overlap, at this point no atoms are lost during the perturbation.

break the required symmetry of the perturbation, and thus leading to dominant coupling to superpositions of angular momentum states. The procedure of aligning the perturbation beam and the main tweezer is shown in Fig. 5.2a. We utilize a Gaussian mode LG_{00} as the perturbation whose intensity is modulated at the radial trap frequency of the tweezer. Hence, in the case that the perturbation beam is slightly displaced with respect to the main trap the atoms are excited from the ground state. Only when the perturbation is largely displaced the intensity modulation has no effect, or when the perturbation is aligned precisely on top of the main tweezer. Then, the coupling to the odd-parity state at the trap frequency is suppressed. We scan the position of the perturbation beam on the atom plane and measure the remaining atoms in the ground state, shown Fig. 5.2b, with an exemplary excitation spectrum in Fig. 5.2c where we recover almost all atoms when both beams overlap. We observe that the relative position of the two beams is stable on a time scale of a few months up to the radial extent of the wavefunction.

Optical abberations - anisotropy of the main trap. The anisotropy $\delta\omega$ of the optical potential breaks the rotational symmetry, therefore, the angular momentum is not a good quantum number anymore. Hence, $\delta\omega$ sets the time scale of preparing the angular momentum state $< 1/\delta\omega$ before the state dephases due to coupling to other states (see section 5.3 for further details). Furthermore, after the preparation of the quantum state, any manipulation such as ramping magnetic fields, rf-pulses, etc., needs to be faster than $1/\delta\omega$. Later in the chapter, we will demonstrate that we can precisely measure the anisotropy of the optical tweezer, enabling us to adjust it. Furthermore, we show that the anisotropy can be harnessed as a tool for characterizing the prepared angular momentum state.

Homogeneity of the perturbation beam. Surprisingly, it turns out that the azimuthal homogeneity of the LG mode is not as crucial as the points mentioned above. We can directly load many non-interacting atoms into an LG mode and measure the density distribution of the atoms *in-situ*, which correlates with the intensity distribution of the optical potential created via the LG mode. We observe that the azimuthal homogeneity is roughly 10 %. This inhomogeneity of the LG mode results in additional coupling elements to unwanted states, however here it is beneficial that the energy spacing set by the trap frequencies of the main trap are large $\sim 10\,\mathrm{kHz}$ such that any additional couplings are suppressed.

5.1.2 Model of the optical trap

The optical tweezer is a tightly focused red-detuned laser beam which can be approximated by a harmonic potential with a radial $\omega/2\pi \approx 28.1\,\mathrm{kHz}$ and an axial $\omega_\mathrm{z}/2\pi \approx 3.7\,\mathrm{kHz}$ trap frequency. Since the rotation only couples to the in-plane motion of the particles, we consider a 2D harmonic oscillator (dotted lines), as shown in Fig. 5.3. Anharmonic corrections lead to shifts of the harmonic energy levels illustrated by the solid lines, they preserve the rotational symmetry, however. The angular momentum state $|m\rangle$ in the LLL are highlighted in red, carrying m quanta of angular momentum, consequently the density at the center is depleted and the state increases in size (in blue). The phase winding of the wavefunction is denoted by the arrow surrounding the density.

The potential is generated from a Gaussian beam which includes higher anharmonic terms. Therefore, we use a 2D Gaussian beam model for the optical tweezer to account for the anharmonicity, which reads for a single particle

$$\mathcal{H}_\mathrm{sp} = \mathcal{H}_\mathrm{kin} + \mathcal{H}_\mathrm{pot} = -\frac{\hbar}{2m_\mathrm{Li}}\Delta - \gamma\frac{P}{w_0^2}e^{-2r^2/w_0^2}, \tag{5.1}$$

expressed in SI-units and with $\gamma \approx 800\ h\cdot\mathrm{kHz}\ \mathrm{\mu m}^2/\mathrm{mW}$. Approximating the Gaussian potential to second lowest non-vanishing order and neglecting a constant energy shift

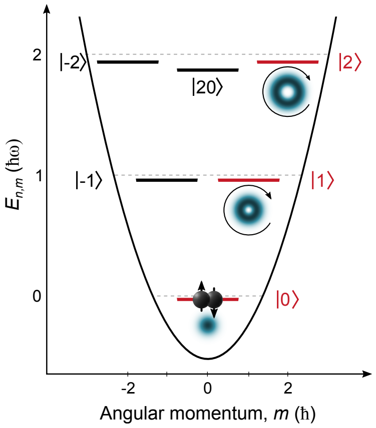

Figure 5.3: Two-dimensional harmonic oscillator. Lowest energy levels of the 2D harmonic oscillator including anharmonic corrections. States in the LLL are highlighted in red. These states carry m quanta of angular momentum revealed through the increase in size of their density distribution (blue).

yields the following approximation of the optical potential

$$\mathcal{H}_{\text{pot}} \approx \frac{2\gamma P}{w_0^4} r^2 - 2\frac{\gamma P}{w_0^6} r^4. \tag{5.2}$$

From this equation, we can see the connection of the harmonic oscillator frequency $m_{\text{Li}}\omega^2/2 \equiv 2\gamma P/w_0^4$ to the optical power P and the waist w_0. Note that the sign of the quartic contribution is negative leading to a down-shift of the energy levels.

In order to obtain the harmonic oscillator frequency ω we measure various transition frequencies from the ground state $|0\rangle$ to the final states $|1\rangle, |2\rangle, |20\rangle$. We use these transition frequencies to fit the optical power P and the waist w_0. This gives a waist of the optical potential $w_0 = 1.1\,\mu\text{m}$ close to the diffraction limited waist $w_0^{\text{diff}} = 0.72\,\mu\text{m}$ of the objective at the optical wavelength $\lambda_{\text{opt}} = 1064\,\text{nm}$. This limit is only reached in the case that an aberration-free light beam illuminates the entrance aperture of the objective completely. The latter requirement is *not* fulfilled in our setup, instead our incoming Gaussian beam is slightly smaller leading to a larger waist in the atom plane.

5.1.3 Transfer to an angular momentum state

In the following discussion, we focus on the preparation of an angular momentum state with $2\hbar$ quanta of angular momentum per particle. For that, we choose a LG_{02}

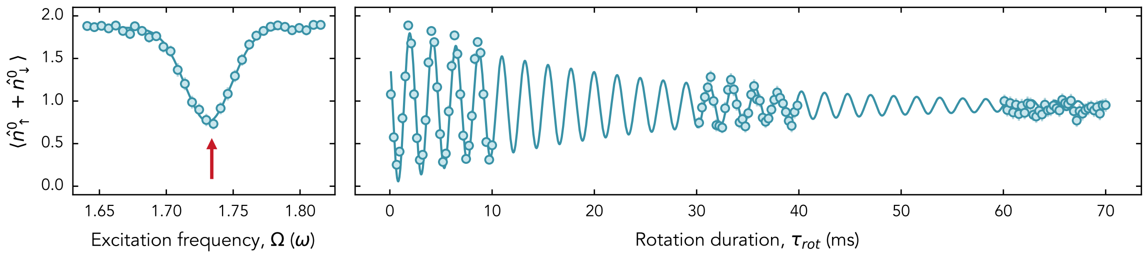

Figure 5.4: Excitation to the angular momentum state. Excitation spectrum by counting the remaining atoms in the single-particle ground state $\langle \hat{n}^0_\uparrow + \hat{n}^0_\downarrow \rangle$ after applying the rotating perturbation for $\tau_{\mathrm{rot}} = 350\,\mu\mathrm{s}$; on the left. Rabi oscillations on the resonance $\Omega_{\mathrm{res}} \approx 1.73\omega$ (red arrow) driven with a Rabi rate $\Omega_{\mathrm{rabi}}/2\pi \approx 0.44\,\mathrm{kHz}$. The coherence time is $\tau^{\text{non-int}}_{\mathrm{coh}} = 23(1)\,\mathrm{ms}$; on the right.

mode which tunes the radially symmetric trap to an elliptical shape, provided that the intensity of the LG_{02} mode is significantly smaller than the main tweezer. The perturbation then reads

$$V_{\mathrm{p}}(t) = \epsilon_{\mathrm{p}} \left(z^2 e^{-i\Omega t} + h.c \right), \tag{5.3}$$

where $z = x + iy$ is the complex coordinate in the radial plane, ϵ_{p} is the strength of the perturbation and Ω the excitation frequency. Given the perturbation, we couple states with angular momentum $\Delta m = \pm 2$ and energy $\hbar\Omega = \pm 2\hbar\omega$. Since we start from the ground state $|0\rangle$ the next available state is $|2\rangle$. In addition to the conservation of angular momentum, the correct excitation frequency Ω needs to be chosen which is set by the harmonic oscillator frequency ω. Coupling to the next higher lying state $|4\rangle$ is suppressed due to the anharmonicity of the trap levels, effectively rendering the ground state $|0\rangle$ and the state $|2\rangle$ a two-level system.

In Fig. 5.4, we measure the single-particle occupation number in the ground state $\langle \hat{n}^0_\uparrow + \hat{n}^0_\downarrow \rangle$ after applying a rotating perturbation for $\tau_{\mathrm{rot}} = 350\,\mu\mathrm{s}$. The resonance frequency of the transition (indicated by the red arrow) is lowered to $\Omega_{\mathrm{res}} \approx 1.73\omega$, compared to the expected frequency at 2ω in a harmonic potential due to the anharmonicity of the optical trap. On resonance, we drive Rabi oscillations between the ground state $|0\rangle$ and the $|2\rangle$ state. In order to treat the $|0\rangle$ and $|2\rangle$ as an effective two level system, the Rabi rate $\Omega_{\mathrm{rabi}} \approx 0.44\,\mathrm{kHz}$ must be be smaller than the energy shift to the next level $|4\rangle$ due to the anharmonicity. The long coherence time $\tau_{\mathrm{coh}} = 23(1)\,\mathrm{ms}$ suggests that this approximation is valid. Furthermore, the coherence time needs to be longer than the inverse Rabi rate $1/\Omega_{\mathrm{rabi}} \approx 2.3\,\mathrm{ms}$ which is well satisfied in our system.

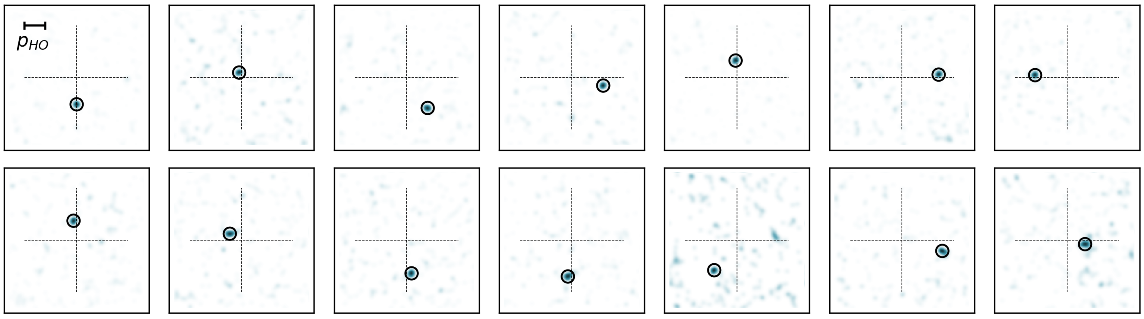

Figure 5.5: Randomly selected images of an angular momentum state. Random selection of snapshots of the wavefunction for a spin down fermion in the angular momentum state $|2\rangle$. We apply a post-selection of images where a single atom is detected. The dotted cross indicates the center of the images.

Finally, we transfer the ground state population to the state $|2\rangle$ via a $\pi-$pulse.

5.2 Detection of angular momentum states

After we prepare the desired angular momentum state $|m\rangle$ in the LLL we utilize our fluorescence imaging technique, discussed in detail in chapter 4. The main trap is switched off instantaneously letting the atoms expand in all three dimensions. In order to keep the atoms in the depth of focus of the objective, we suppress the expansion in the vertical direction by quenching on a 2D lattice yielding a vertical confinement on the same order as the tweezer. The 2D lattice is only turned on during the time-of-flight expansion. The atoms expand radially in the remaining harmonic confinement of the 2D lattice $\omega_{\mathrm{r,2D}} \approx 47.2\,\mathrm{Hz}$ which is roughly a factor 600 smaller than ω. On the camera we record the final position of the atoms after the time-of-flight expansion. Since the expansion of the atoms is self-similar, given that we prepare an eigenstate of the harmonic oscillator, we map the final position of the atoms to their initial momentum. Here, we compensate the slight radial confinement of the 2D lattice. In each experimental realization we obtain an image corresponding to the momentum of the spin down fermion in the prepared state. We binarize and apply a low-pass filter to the image. Afterwards, we use a peak-detection algorithm based on a simple threshold function to identify the atoms' position. If the number of peaks in the image coincide with the prepared atom number (in this case a single atom), the peak positions are saved. All other images with the incorrect atom number are disregarded. Since the

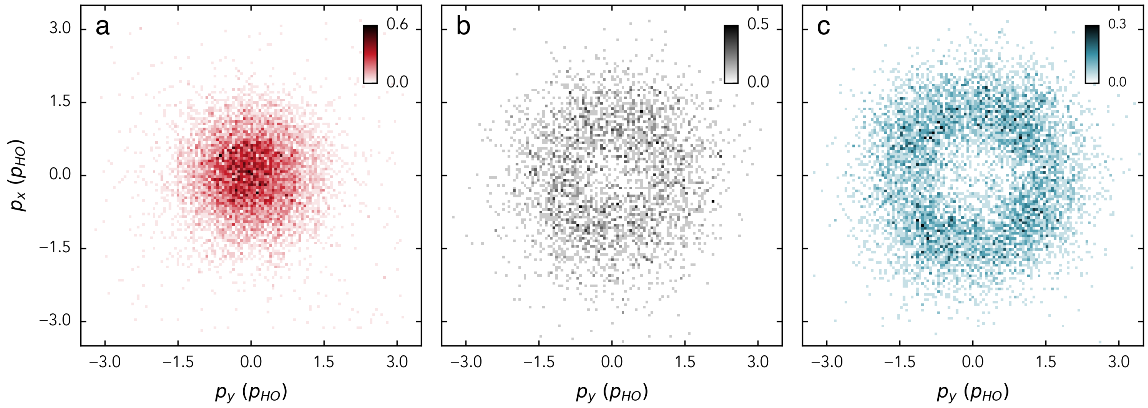

Figure 5.6: Normalized 2D momentum space density of states in the LLL. **a**, the ground state $|0\rangle$ shows a Gaussian distribution. **b**, the state $|1\rangle$ shows a vortex distribution in the density indicating the imprint of angular momentum on the wavefunction. **c**, the state $|2\rangle$ shows a similar distribution as $|1\rangle$, however the vortex size increases due to a larger angular momentum.

preparation and the imaging are independent of one each other, the post-selection procedure has no systematic effect on the measurement of the wavefunction. In Fig. 5.5, we show randomly selected images of atoms prepared in the angular momentum state $|2\rangle$, after post-selecting on the correct atom number. The black circle highlights the detected position of the atom. Hence, in each experimental realization, we project the wavefunction on the momentum of the single atom. Preparing the exact same quantum state in multiple experimental realizations yields a list of momenta which allows us to reconstruct the momentum density of the wavefunction.

In Fig. 5.6, we show the density of the first three angular momentum states in the LLL. The ground state (red) is naturally obtained by our state preparation. The states $|1\rangle$ (black) and $|2\rangle$ (blue) are obtained by imprinting an LG_{01} or LG_{02} mode on the SLM, respectively. This is followed by measuring the resonance frequency of the transition and driving rabi oscillations on resonance. Subsequently, we pulse the ground state to the respective angular momentum state. Both states $|1\rangle, |2\rangle$ show the striking feature of non-zero angular momentum states - a radially symmetric density depletion in the center of the wavefunction. As the angular momentum of the state increases, so does the size of the wavefunction visible in the density that peaks at a distance $\sqrt{m}p_{\mathrm{HO}}$.

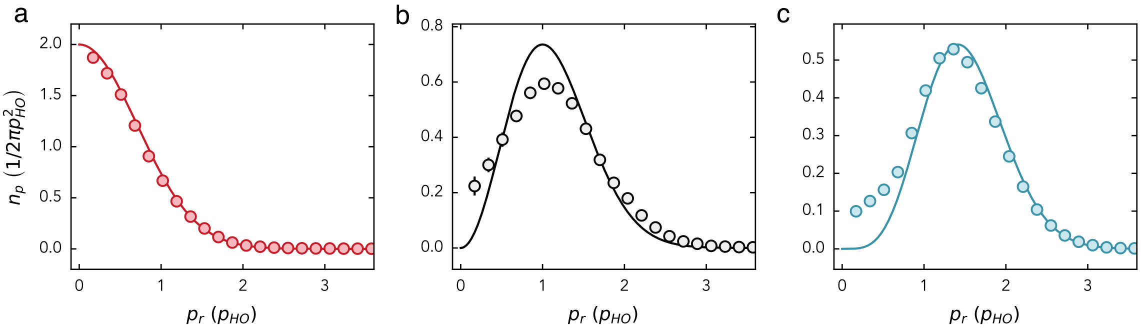

Figure 5.7: Radial densities of states in the LLL. The 2D densities are azimuthally averaged. The radial densities are quantitatively compared to the theoretically expected density of the harmonic oscillator in the ground state $|0\rangle$ (**a**), the state $|1\rangle$ (**b**) and the state $|2\rangle$ (**c**).

In order to compare the experimental data to the theoretically expected density distributions we azimuthally average the 2D densities. We use a kernel density estimation (KDE) to obtain the appropriately normalized radial density n_p from the 2D densities. The two free parameters of KDE are the kernel and the bandwidth. We choose a *tophat* kernel to avoid strong smoothing of the data and thus the suppression of small scale structures. Furthermore, the bandwidth is chosen to $0.17p_\mathrm{HO}$ which is slightly smaller than the average of the effective resolution of both spin states (see chapter 4). The KDE normalizes the density $\int_0^\infty \tilde{n}_\mathrm{p}\mathrm{d}p_\mathrm{r} = 1$, which makes it necessary to divide by the radius p_r to obtain $\int_0^\infty p_\mathrm{r} n_\mathrm{p}\mathrm{d}p_\mathrm{r} = 1$, with $\tilde{n}_\mathrm{p} = p_\mathrm{r} n_\mathrm{p}$. Therefore, the data point at $p_\mathrm{r} = 0$ is neglected.

The radial densities n_p in momentum space are shown in Fig. 5.7. The solid lines are the theoretical expectations without free parameters, solely based on the radial trap frequency ω obtained from the model of the optical trap. All distributions show qualitative agreement with the parameter-free theoretical curve. The largest deviation of the angular momentum states $|1\rangle$, $|2\rangle$ from theory arises at small momenta. This is most dominantly caused by an imperfect Rabi pulse such that a part of the population remains in the ground state (which peaks at zero momentum).

5.3 Sense of rotation

So far, we have shown that the density distribution of the angular momentum states $|1\rangle$, $|2\rangle$ contain a density depletion in the center suggesting the imprint of a phase winding, and thus the incorporation of angular momentum. However, playing the devils advocate it is possible to construct a density with exactly the same density depletion in the center, which we have considered so far as the smoking gun of a rotating atom, but with zero angular momentum. To illustrate this argument, we focus on the density of the state $|2\rangle$ in the following of this section.

Consider two examples, first, an equal superposition of the ground state $|0\rangle$ and the state $|20\rangle$ (see in Fig. 5.3). Neither of the states contains angular momentum, however the density distribution of the superposition $|0\rangle - |20\rangle$ is not distinguishable from the density in Fig. 5.6c. Furthermore in the second example, consider a superposition of the clockwise $|2\rangle$ and counter-clockwise rotating states $|{-2}\rangle$, that is $|\pm\rangle = 1/\sqrt{2}(|2\rangle \pm |{-2}\rangle)$. Neither of the superposition states $|\pm\rangle$ contains any angular momentum, however, if we were to sample from a balanced incoherent mixture of these states, the obtained density would resemble the density distribution shown in Fig. 5.6c. How can we distinguish between these examples and the case of an angular momentum state?

To this end, we investigate the time evolution of the wavefunction in a slightly anisotropic trap, illustrated in Fig. 5.8. In a symmetric potential the angular momentum states are eigenstates of the Hamiltonian and therefore stationary. However, we make use of a small anisotropy of the optical potential which we attribute to a slight ellipticity of the trap. This breaks the rotational symmetry and couples states with angular momentum $\Delta m = \pm 2$. Specifically, we can include the ellipticity of the form $x^2 - y^2$ in the optical potential in Eq. 5.1 and approximate to the lowest order in the ellipticity

$$V_\mathrm{p} \propto \frac{2}{w_0^2} r^2 - \frac{2}{w_0^4} r^4 + \frac{2\epsilon_\mathrm{e}}{w_0^2} r^2 (\cos^2\phi - \sin^2\phi), \tag{5.4}$$

where ϵ_e corresponds to the strength of the ellipticity, and where we have expressed the ellipticity in polar coordinates.

Due to the ellipticity of the trap the angular momentum states are not eigenstates anymore, instead the superposition states $|\pm\rangle = 1/\sqrt{2}(|2\rangle \pm |{-2}\rangle)$ form the new eigenstates of the system, with an energy difference given by the anisotropy $\delta\omega$, assuming that the anharmonicity suppresses coupling to the state $|20\rangle$. Effectively, we can consider the $|\pm\rangle$ as a two-level system which span the basis states of the Bloch sphere, sketched in Fig. 5.8a. Coupling to states in different L_z manifolds is suppressed due to the large spectroscopic gap of the harmonic oscillator frequency ω. Preparing the angular momentum state $|2\rangle$ then leads to a characteristic time evolution on the equator of the Bloch sphere given by the energy difference $\delta\omega$ of the eigenstates $|\pm\rangle$.

We perform Ramsey spectroscopy on the state $|2\rangle$ and observe coherent oscillations with a frequency given by the anisotropy $\delta\omega$. The conceptual protocol is sketched in Fig. 5.8b, and the measured Ramsey spectrum is shown in Fig. 5.8c. We use a

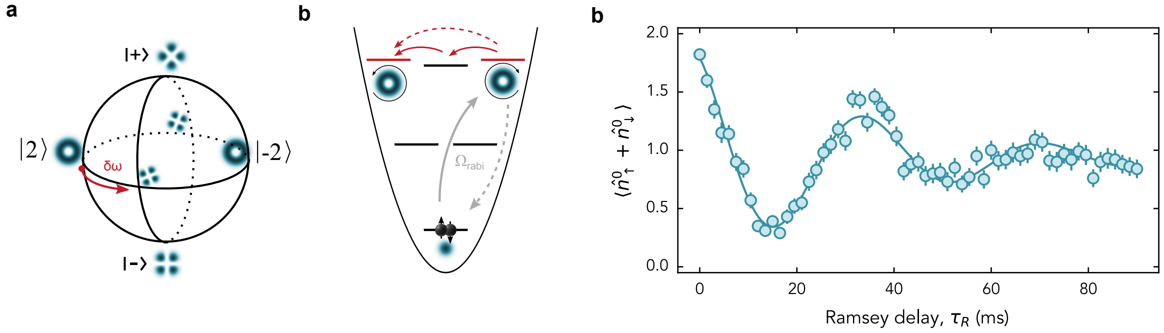

Figure 5.8: Ramsey spectroscopy of two non-interacting rotating fermions. **a**, The angular momentum eigenstates are not a good basis anymore in an anisotropic harmonic oscillator. Instead, the superposition states $|\pm\rangle = 1/\sqrt{2}(|2\rangle \pm |-2\rangle)$ constitute the new eigenstates of the system with an energy difference given by the anisotropy $\delta\omega$. The state $|2\rangle$ is an equal superposition of the eigenstates $|+\rangle, |-\rangle$. Hence, it evolves over a duration of time τ_R on the equator of the Bloch sphere. **b**, The anisotropy introduces a coupling of the clockwise and counter-clockwise rotating states $|2\rangle$ and $|-2\rangle$, respectively. We makes use of this effect to conduct Ramsey spectroscopy on the $|2\rangle$ state. After preparing it via a $\pi-$pulse, we wait for a delay time τ_R. Subsequently, we use a second $\pi-$pulse to de-excite the atoms to the ground state. The overlap with the ground state oscillates, depending on the contribution of the $|-2\rangle$ state. **c**, Ramsey spectrum of two non-interacting fermionic atoms in an anisotropic optical potential.

$\pi-$pulse to prepare the clockwise rotating state $|2\rangle$ (grey solid arrow). Subsequently, we let the system evolve for a Ramsey delay time τ_R (red arrows), after which we use a second $\pi-$pulse to de-excite the evolved state to the ground state (gray dashed arrow) and measure the single-particle occupation number in the ground state $\langle \hat{n}^0_\uparrow + \hat{n}^0_\downarrow \rangle$. The number of atoms in the ground state oscillate depending on the contribution of the state $|-2\rangle$. It is worthwhile to point out that at long times the occupation number in the ground state after long Ramsey delay times $\tau_\mathrm{R} > 80\,\mathrm{ms}$ reaches a constant value of roughly 1 which indicates that the we indeed end up with a balanced incoherent mixture of the states $|\pm\rangle$.

We further measure the 2D densities during the time evolution to directly reveal the sense of rotation, shown in Fig. 5.9, at times $\tau_\mathrm{R} = 0\,\mathrm{ms}, 7.5\,\mathrm{ms}, 15\,\mathrm{ms}, 22.5\,\mathrm{ms}$. These correspond to multiples of quarter times of the periodicity of the oscillation.

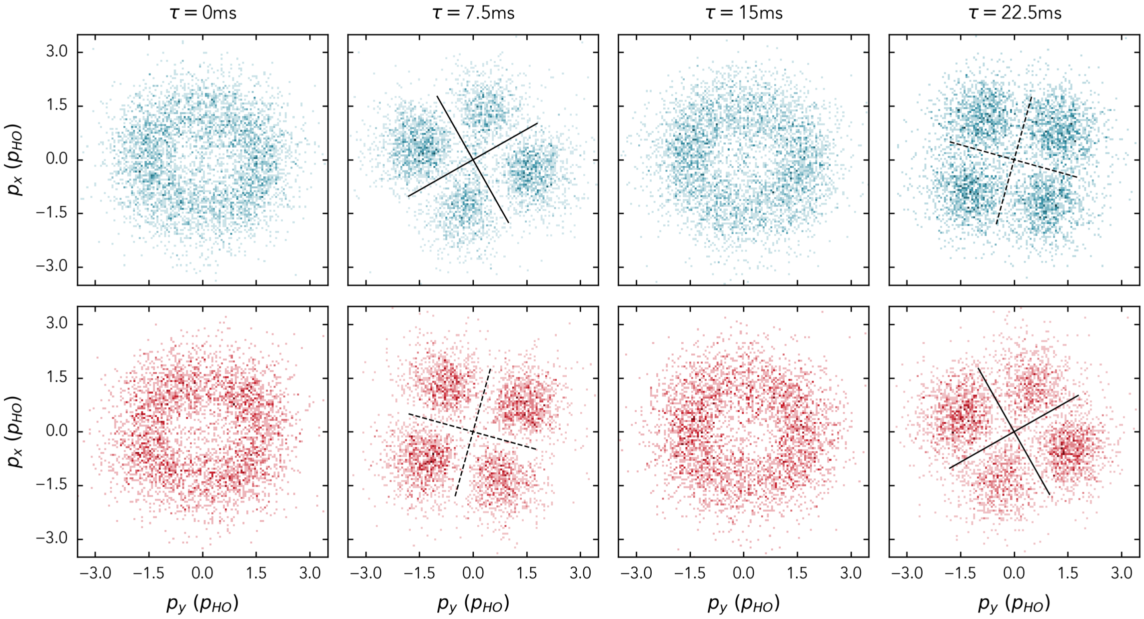

Figure 5.9: Sense of rotation. Solid and dashed lines are orthogonal among each other, and tilted by 45° with respect to each other. **upper row**, clockwise rotation on the Bloch sphere. **lower row**, counter-clockwise rotation on the Bloch sphere.

On the SLM we can imprint both a clockwise (upper row, blue) and counter-clockwise (lower row, red) phase winding resulting in the opposite rotation direction on the Bloch sphere (see Fig. 5.8a). In both cases, we observe the expected time evolution of the wavefunction determined by the rotation direction. The black solid and dashed lines indicate the orientation of the superposition states tilted by an angle of 45° with respect to each other.

5.4 Two non-interacting rotating fermions

Since the particles are non-interacting it is sufficient to only detect a single spin component and treat the other one as an identical copy. However, our imaging technique allows us to detect both spin states in a single experimental realization, as detailed in section 4.4. In each experimental realization we obtain two images corresponding to the spin up and spin down fermion of the prepared state after a time-of-flight expansion. If the number of atoms in both images coincide with the correct atom number

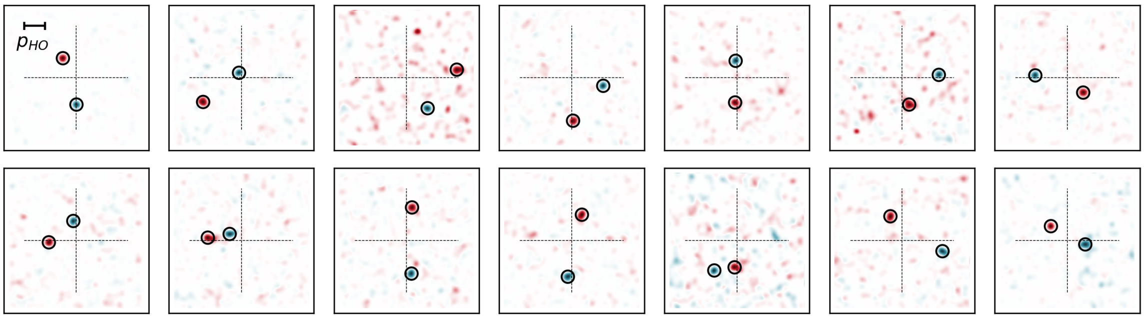

Figure 5.10: Spin-resolved sampling of the two-particle wavefunction. Randomly chosen images after post-selection for the correct atom number in each state for atoms in state $|2\rangle$. The spin down state is shown in blue, spin up state in red.

in both images (one atom per spin state), the peak position are saved. All other images with the incorrect atom number are discarded. We then use the same method as above to determine the momentum of each spin state and express it in units of the harmonic oscillator momentum p_{HO}. Randomly selected images of the projection of the two-particle wavefunction in state $|2\rangle$ are shown in Fig. 5.10.

Sampling the wavefunction of both spin states allows us to perform a transformation to center-of-mass and relative coordinates. In each experimental realization we measure the momentum $\mathbf{p} = (p_{\mathrm{x}}, p_{\mathrm{y}})$ of the spin up and spin down fermion, denoted as $\mathbf{p}_{\uparrow}$ and $\mathbf{p}_{\downarrow}$, respectively. We then calculate the center-of-mass $\mathbf{p}_{\mathrm{com}} = 1/\sqrt{2}(\mathbf{p}_{\uparrow} + \mathbf{p}_{\downarrow})$ and relative $\mathbf{p}_{\mathrm{rel}} = 1/\sqrt{2}(\mathbf{p}_{\uparrow} - \mathbf{p}_{\downarrow})$ momentum in each snapshot of the wavefunction. Multiple realizations of the same initial wavefunction allow us to reconstruct the 2D momentum space density in center-of-mass and relative coordinates.

5.4.1 Center-of-mass and relative coordinates

In Fig. 5.11, we show the normalized 2D densities of the non-interacting rotating fermions excited to the state $|2\rangle$ in both the single-particle basis (**a**) and the center-of-mass and relative basis (**b**). Besides experimental imperfections, most dominantly due to the off-resonant scattering of the spin up state which leads to broadening of the vortex distribution (see section 4.4 for details), both spin states are identical in the single-particle basis. They show a vortex distribution due to insertion of $2\hbar$ quanta of angular momentum per spin state. In the center-of-mass and relative basis, both densities look identical as well since the particles are non-interacting. The density

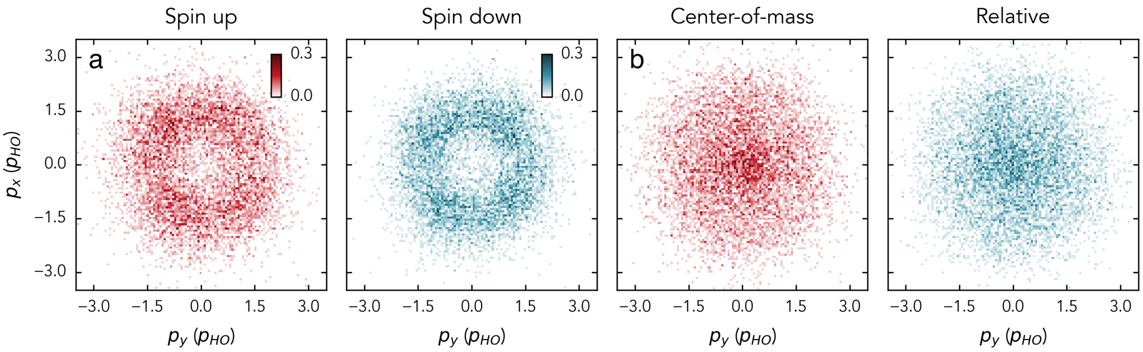

Figure 5.11: Density of two non-interacting, rotating fermions. a, Normalized density of the spin up and spin down states. Both densities show a vortex distribution. **b,** Normalized density in center-of-mass coordinates $\mathbf{p}_{\rm com} = 1/\sqrt{2}(\mathbf{p}_\uparrow + \mathbf{p}_\downarrow)$ and in relative coordinates $\mathbf{p}_{\rm rel} = 1/\sqrt{2}(\mathbf{p}_\uparrow - \mathbf{p}_\downarrow)$. The center-of-mass and relative distribution are identical since the particles are non-interacting. The same colorbars are used for **a** and **b**.

depletion at small momenta is not visible, on the contrary the density distribution exhibits a peak.

In order to understand the shape of the particles' wavefunction in the center-of-mass and relative coordinates it is instructive to consider the following arguments in the harmonic potential. In total, we insert $4\hbar$ quanta of angular momentum into the system via the LG_{02} perturbation since our perturbation is symmetric both in the single-particle basis and the center-of-mass and relative basis

$$V_{\rm p}(t) = \epsilon_{\rm p}\left(z_\uparrow^2 e^{-i\Omega t} + z_\downarrow^2 e^{-i\Omega t} + h.c\right) \tag{5.5a}$$

$$= \epsilon_{\rm p}\left(z_{\rm com}^2 e^{-i\Omega t} + z_{\rm rel}^2 e^{-i\Omega t} + h.c\right), \tag{5.5b}$$

where $\epsilon_{\rm p}$ corresponds to the strength of the perturbation, and the arrows denote the respective spin state. We couple the ground state $|0\rangle_\uparrow |0\rangle_\downarrow$ to a state with a total angular momentum of $2 \times 2\hbar$. The state to which we couple lives in the $4\hbar$ quanta of angular momentum manifold and equally distributes the angular momentum among the spin components, as they are non-interacting. The state takes the form

$$|2\rangle_\uparrow |2\rangle_\downarrow \simeq z_\uparrow^2 z_\downarrow^2, \tag{5.6}$$

where we have expressed the 2D harmonic oscillators states in real space coordinates. Inserting the definition of center-of-mass and relative coordinates $z_{\rm com} = 1/\sqrt{2}(z_\uparrow + z_\downarrow)$ and $z_{\rm rel} = 1/\sqrt{2}(z_\uparrow - z_\downarrow)$, respectively, allows then to identify the harmonic oscillator

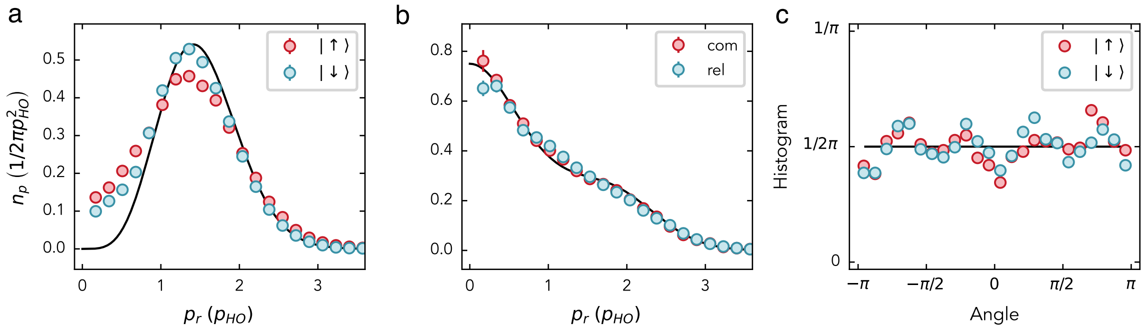

Figure 5.12: Azimuthally averaged densities of two non-interacting, rotating fermions. **a**, Normalized radial density of the spin up and spin down states. The solid line corresponds to the state $|2\rangle$. **b**, Normalized radial density in center-of-mass coordinates $\mathbf{p}_{\text{com}} = 1/\sqrt{2}(\mathbf{p}_\uparrow + \mathbf{p}_\downarrow)$ and in relative coordinates $\mathbf{p}_{\text{rel}} = 1/\sqrt{2}(\mathbf{p}_\uparrow - \mathbf{p}_\downarrow)$. The solid line corresponds to the density according to Eq. (5.7). **c**, Azimuthal distribution of both spin states in the single-particle basis.

states in the center-of-mass and relative basis. Taking care of the normalization factors, we arrive at

$$|2\rangle_\uparrow |2\rangle_\downarrow = \sqrt{\frac{3}{8}}\Big(|4\rangle_{\text{com}} |0\rangle_{\text{rel}} + |0\rangle_{\text{com}} |4\rangle_{\text{rel}} \Big) - \frac{1}{2} |2\rangle_{\text{com}} |2\rangle_{\text{rel}} \,, \tag{5.7}$$

where on the left side it is expressed in the single-particle basis, and on the right side the center-of-mass and relative basis is chosen. In the latter basis, the state is a superposition of states where either the center-of-mass motion incorporates the total of $4\hbar$ quanta of angular momentum and the relative motion remains in the ground state or vice versa, or $2\hbar$ quanta of angular momentum are shared.

In Fig. 5.12a,b, we show the radial densities of the spin up and spin down state in the single-particle basis (**a**) and in the center-of-mass and relative basis (**b**). Qualitatively, we observe reasonable agreement between theory and experiment in both bases. In the single-particle basis, both spin up and spin down distributions follow the distribution of the state $|2\rangle$. Most noticeable is the difference of theory and experiment at low momenta $p_{\text{r}} \to 0$, where the experimental data doesn't reach zero, in both cases of the spin up and spin down state. This might be a residual effect of the finite probability of transferring the ground state to the excited state. In the center-of-mass and relative basis, both densities are identical following the theoretically expected curve of Eq. (5.7).

In addition to azimuthally averaging, we determine the normalized histogram of the azimuthal distribution by integrating out the radial direction, shown in Fig. 5.12c. The homogeneity of the azimuthal distribution indicates (in addition to the observed Rabi oscillations) that we indeed prepare an angular momentum eigenstate. However, we also observe a small oscillation with a frequency 4φ suggesting a contribution of the counter clockwise rotating state $|-2\rangle$ which results in an interference pattern, discussed in the previous section.

Conclusion

We have demonstrated motional control of angular momentum states in the lowest Landau level of a single fermion in an optical potential. To this end, we interfere the rotationally symmetric tweezer with a Laguerre-Gaussian mode of lth order to imprint $l\hbar$ quanta of angular momentum on a single atom. Furthermore, we made use of a slight anisotropy of the optical potential to confirm the sense of rotation of the particle. This is not only a precise experimental tool to determine the anisotropy, but it also allows us to tune the anisotropy with the SLM.

The experimental tools we have developed in this chapter are the foundations for the following work, where we introduce interactions among the fermions to realize exotic quantum states reminiscent of FQH states.

6

Realization of a Laughlin state

Topologically ordered phases of matter emerge in the context of the fractional quantum Hall (FQH) effect, arising from the interplay of strong magnetic fields and interactions among the electrons [Tsu82; Wen07]. The magnetic field constrains the electrons to move on fast rotating cyclotron orbits which quenches their kinetic energy[1]. This leads to the formation of highly degenerate Landau levels which are separated by the high cyclotron frequency. The properties of these states are characterized by the filling factor ν defined as the ratio of electrons and the number of available states per Landau level [Giu12]. It was Laughlin's ingenious idea to postulate a wavefunction where the electrons minimize their Coulomb interaction energy by incorporating relative angular momentum with respect to each and every electron. This qualitatively describes the ground state of the $\nu = 1/m$ filling factor [Lau83], with m being an odd integer for fermions. His variational ansatz is nowadays famously known as Laughlin's wavefunction, see Eq. (2.18).

In the limit of rapidly rotating ultracold atomic gases, strongly correlated phases are predicted analogous to FQH states [Coo08; Coo01; Ho01; Reg03; Pop04]. Here, the Coriolis force takes on the role of the Lorentz force as they are mathematically equivalent. This opens up an intriguing approach to study FQH states in these engineered systems as they offer an unprecedented level of microscopic control of individual constituents and tunability of the system parameters [Blo08; Dal16].

Reaching the deconfinement limit of the rapidly rotating potential $\Omega \to \omega$, where Ω is the rotation frequency and ω is the radial trap frequency, is experimentally challenging as it requires to overcome two central aspects. First, on the technical side, any trap imperfection (such as the ellipticity, roughness, etc. of the trap) leads to a static perturbation in the laboratory frame which couples the ground state to higher lying or degenerate states, and therefore results in *heating*. Second, the *energy gap* of the

---

[1] The notion of quenching the kinetic energy refers to its significant increase with respect to the interaction energy. Thus, in the low-energy sector the only dominant energy scale is given by the interactions and the kinetic energy can be neglected.

FQH state to excited states tends to be fragile. It is given by the only relevant energy scale in the 2D LLL, the zeroth order Haldane pseudopotential [Coo08] $\mathcal{V}_0 \simeq \hbar\omega a_\mathrm{s}/a_\|$ (introduced in chapter 2), with the scattering length a_s and the vertical harmonic oscillator length $a_\|$. In typical experiments of rotating bosonic systems [Muk22], the pseudopotential is on the order of $\mathcal{V}_0 \sim 200\,\mathrm{mHz}$ which demands exceedingly slow preparation times to achieve adiabatic ground state preparation and furthermore poses a challenge on the robustness of the Laughlin state with respect to excitations from heating. To increase $\mathcal{V}_0$, the radial trap frequency ω and the vertical length scale $a_\|$ can be increased by using tighter optical traps in the respective dimension, and the scattering length can be manipulated via a Feshbach resonance in many atomic species [Tie10; Geh03]

Slowly rotating ultacold atomic gases corresponding to $\nu \gg 1$ have been used early on to study the properties of superfluidity [Fet03]. In this limit, quantized flux vortices form above a critical rotation frequency [Mad00] which then arrange in a triangular Abrikosov lattice [Abo01; Zwi05], similar to superfluid liquid helium-3 [Don91] and type-II superconductors [Til19]. Spinning up the gas further has been realized with ultracold Bose gases, signalled by the softening of the Abrikosov lattice [Bre04; Sch04] and more recently, by geometric squeezing into the LLL, thereby distilling a single Landau gauge wavefunction [Fle21; Muk22; Yao23]. First signatures of entering the regime $\nu \sim 1$ were detected with few bosonic atoms in a rotating optical lattice [Gem10], and lately an unambiguous observation of a Laughlin state with two bosons in a driven optical lattice [Léo23] has been realized. It is worth noting that Laughlin states consisting of two photons were also observed in photonic platforms [Cla20; Wan24]. However, ultracold Fermi gases in the regime $\nu \lesssim 1$ are so far unexplored experimentally since, additionally to the aforementioned reasons, it is notoriously hard to transfer all fermions from the non-rotating ground state to the LLL, given the Pauli exclusion principle.

Here, we exploit the experimental tools developed in the previous chapter to realize the $\nu = 1/2$ Laughlin state with two spinful fermions by rapidly rotating the optical potential. We spectroscopically characterize the Laughlin state and demonstrate the suppression of inter-particle interactions within the model of the optical potential. Furthermore, we make use of our single atom and spin resolved imaging technique to sample the Laughlin wavefunction. This reveals its remarkable features including the incorporation of angular momentum in the relative motion of the particles, while the center-of-mass motion remains in the ground state. These measurements give direct access to the microscopic details of the Laughlin wavefunction determined via the pair and angle correlations. We can now enter the playground to assemble FQH states with rotating ultracold atomic gases. Most of the results presented in this chapter are based on the publication [Lun24].

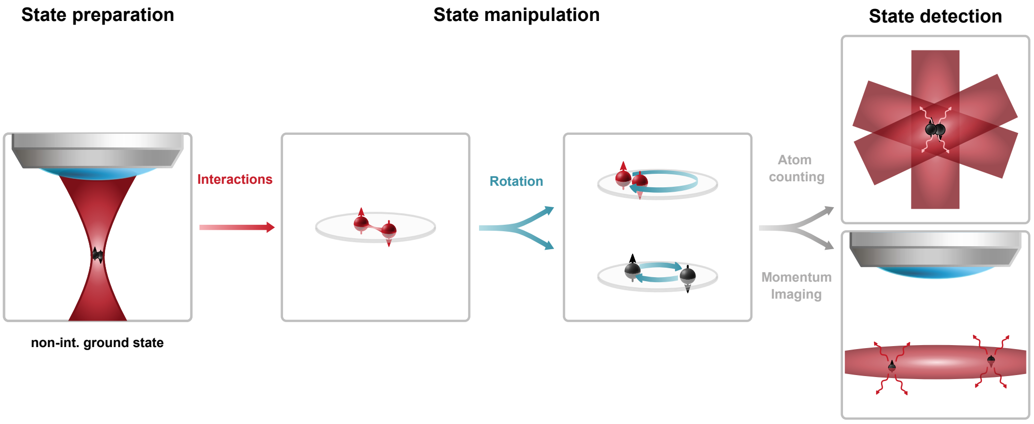

Figure 6.1: Experimental sequence for realizing a Laughlin state. First, a non-interacting spin up and spin down fermion (black particles) is prepared in the ground state of the optical tweezer focused through the objective. Interactions are tuned to break the symmetry between the center-of-mass and relative degree of freedom, since interactions only couple to the relative part of the wavefunction. The center-of-mass and relative rotating states tune differently in energy with the scattering length which allows for selective addressing. After the state manipulation, we detect the Laughlin state either by counting the number of atoms occupying the non-rotating ground state (upper box) or by measuring the momentum of each particle after a time-of-flight expansion (lower box).

6.1 Preparation of a Laughlin state

Conceptually, the realization of the Laughlin state requires two ingredients, interactions between the constituents and a strong synthetic magnetic field. In the absence of interactions, as discussed in the previous chapter, the particles simply rotate independently of each other. In this scenario, both the distributions in the single-particle basis and the center-of-mass and relative basis are identical. Interactions however, break the symmetry between the particles' center-of-mass and relative motion as they only couple to the relative degree of freedom. In the context of contact interactions, a state where the rotation is only present in the center-of-mass motion is still interacting, in contrast to a state where the rotation appears in the relative motion. Hence, the energy of the two states tune differently with the interaction strength and thus can selectively be addressed spectroscopically.

Our approach to prepare and detect a Laughlin state of two rapidly rotating fermions consists of three main steps, illustrated in Fig. 6.1. We start by preparing a non-interacting spin up and spin down fermion in the ground state of the optical potential. In the next step, state manipulation takes place by tuning the interactions of the fermions via a Feshbach resonance. Thereafter, we insert angular momentum into the system by tuning the trap to an elliptical shape that rotates. For sufficiently large interactions the center-of-mass and relative rotation decouple, which allows for selective addressing of the relative rotation corresponding to the Laughlin state. Finally, we exploit two methods available in our experiment to detect the Laughlin state. Either we characterize the system spectroscopically by measuring the remaining number of atoms occupying the ground state in the non-rotating frame or we let the system expand during a time-of-flight to detect the momentum of each particle. In the latter case, each experimental realization yields a snapshot of the Laughlin wavefunction in momentum space which allows to re-construct the density after many experimental cycles and to access correlations of the two particles.

The spatial part of the $N = 2$ particle Laughlin wavefunction in real space reads

$$\psi_{1/m}(z_\uparrow, z_\downarrow) \simeq (z_\uparrow - z_\downarrow)^m e^{-1/2(|z_\uparrow|^2+|z_\downarrow|^2)}, \tag{6.1}$$

where $z_\uparrow, z_\downarrow$ correspond to the complex coordinate of the spin up and spin down fermion in the radial plane, respectively. They are expressed in units of the harmonic oscillator length l_{HO} which is the natural unit in our harmonic oscillator potential. The angular momentum is given by $m\hbar$ which is incorporated in the relative coordinates of the spin up and spin down fermion $(z_\uparrow - z_\downarrow)$, and the filling factor is given by $\nu = 1/m$. In our case of two contact-interacting particles, the Laughlin wavefunction is the true ground state in the rotating frame at total angular momentum $M = N(N-1)m/2$ [Wil98] and is normalized to the given number of particles $N = 2$.

The total wavefunction is composed of a spin part and a spatial part and needs to be anti-symmetric due to the fermionic nature of the constituents. Since we work with a spin singlet (which is anti-symmetric), the spatial part of the wavefunction needs to be symmetric, restricting the angular momentum to even numbers. Therefore, the lowest accessible Laughlin state is the $\nu = 1/2$ state. Curiously, due to the symmetry of the spatial wavefunction it is a bosonic $\nu = 1/2$ Laughlin state made out of two spinful fermions.

A time-of-flight expansion of a many-body wavefunction in the LLL, for which interactions are negligible, corresponds to a magnification of the initial real space wavefunction that is rotated by $\pi/2$ within the plane of expansion [Rea03]. For a Laughlin wavefunction, which is a strongly correlated but non-interacting state in the context of contact-interactions living in the LLL, these assumptions are save to assume. In the specific case of $N = 2$ particles, the invariance of the $\nu = 1/2$ Laughlin state after a

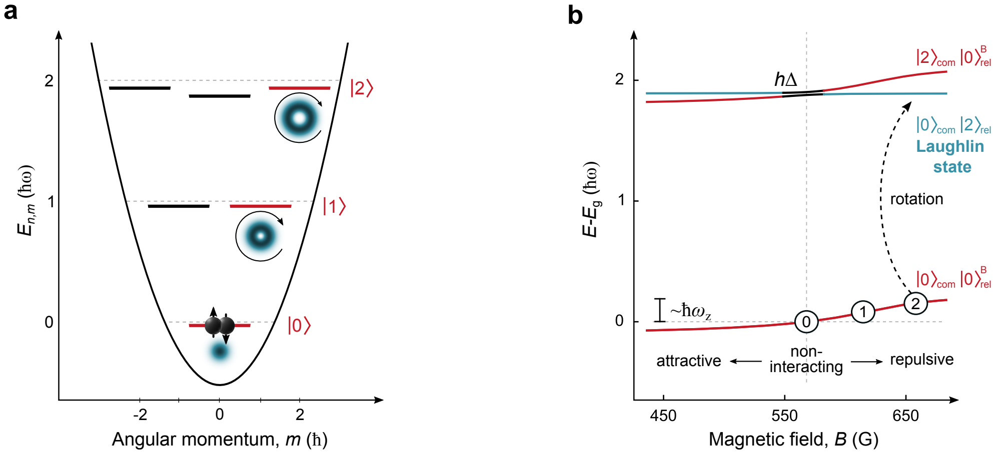

Figure 6.2: Preparing the $\nu = 1/2$ Laughlin state. **a**, We prepare two non-interacting spinful fermions in the ground state of the optical potential. In the horizontal plane, the potential is described by a 2D harmonic oscillator with anharmonic corrections. States $|m\rangle$ in the LLL are marked red and carry angular momentum $L_z = m\hbar$ along the axial direction. **b**, We show the energy spectrum of two interacting fermions in a cigar-shaped harmonic trap in the $L_z = 0\hbar, 2\hbar$ angular momentum manifolds, where we include an anharmonicity Δ (highlighted in black). States in the relative ground state $|0\rangle^B_{\mathrm{rel}}$ tune with the magnetic field resulting in an energy shift compared to the the non-interacting ground state energy E_g. The interaction energy shift E_{int} is on the order of the axial trap frequency ω_z. The states $|2\rangle_{\mathrm{com}}|0\rangle_{\mathrm{rel}}$ and $|0\rangle_{\mathrm{com}}|2\rangle_{\mathrm{rel}}$ in the $L_z = 2\hbar$ manifold decouple in the limit $E_{\mathrm{int}} \gg \Delta$. In that limit, the Laughlin state is $|\psi_{1/2}\rangle = |0\rangle_{\mathrm{com}}|2\rangle_{\mathrm{rel}}$.

time-of-flight expansion also follows from the fact that it is an eigenstate of the harmonic oscillator. The wavefunction we detect in momentum space is therefore identical to the real space wavefunction.

6.1.1 Spectroscopy of two interacting fermions

The approach to realize the two particle $\nu = 1/2$ Laughlin state is illustrated in Fig. 6.2. We start with two non-interacting fermions in the ground state of the optical potential which can be approximated by a harmonic trap with a radial trap frequency of $\omega/2\pi \approx 56.1\,\mathrm{kHz}$ and an axial trap frequency of $\omega_z/2\pi \approx 7.9\,\mathrm{kHz}$. Since the rotation couples only to the radial degree of freedom we treat the system as a 2D harmonic oscillator with anharmonic corrections (see in **a**). To realize the $\nu = 1/2$ Laughlin state, we interfere the optical potential with a LG_{02} mode which deforms the trap elliptical in the limit of small perturbation strengths ϵ_p. The perturbation is symmetric in center-of-mass and relative coordinates and reads

$$V_\mathrm{p}(t) = \epsilon_\mathrm{p}\left(z_\mathrm{com}^2 e^{-i\Omega t} + z_\mathrm{rel}^2 e^{-i\Omega t} + h.c\right). \tag{6.2a}$$

The Laughlin wavefunction (see Eq. (6.1) contains angular momentum only in the relative motion of the two particles. It is therefore necessary to tune the interaction energy between the particles in order to break the symmetry in the center-of-mass and relative degree of freedom. We depict the energy spectrum of two contact-interacting fermions trapped in cigar-shaped optical trap (see in Fig. 6.2b), highlighting the relevant energy levels within the $L_\mathrm{z} = 0\hbar, 2\hbar$ manifold. Any axially excited states and different angular momentum manifolds are excluded.

In a harmonic potential, the center-of-mass and relative motion decouple. However, anharmonic corrections $\Delta \approx 1.4\,\mathrm{kHz}$ stemming from quartic contributions $\sim r^4$ of the anharmonic potential lead to coupling between the center-of-mass and relative coordinates, illustrated by the avoided crossing in Fig. 6.2b (black). In the limit of large interaction energy shifts $E_\mathrm{int} \gg \Delta$ this coupling can be neglected and the Laughlin state is a plain rotation in relative coordinates. Note that in general the energy shift is approximately on the order of the axial trap frequency, however the exact energy shift depends on the trap geometry.

The normalized spatial wavefunction of the two particle Laughlin state $|\psi_{1/2}\rangle$ can be expressed in harmonic oscillator eigenstates

$$|\psi_{1/2}\rangle = |0\rangle_\mathrm{com}|2\rangle_\mathrm{rel} \tag{6.3a}$$

$$= (|0\rangle_\uparrow|2\rangle_\downarrow + |2\rangle_\uparrow|0\rangle_\downarrow)/2 - |1\rangle_\uparrow|1\rangle_\downarrow/\sqrt{2}, \tag{6.3b}$$

in the center-of-mass and relative basis (Eq. 6.3a) and the single particle basis (Eq. 6.3b). In the center-of-mass basis, the Laughlin state $|\psi_{1/2}\rangle$ carries $0\hbar$ angular momentum in the center-of-mass motion, thus remaining in the ground state, while incorporating $2\hbar$ quanta of angular momentum in the relative motion. In the single-particle basis, on the other hand, $|\psi_{1/2}\rangle$ can be viewed as a superposition of either one fermion carrying $2\hbar$ of angular momentum while the other one remains in the ground state, or both sharing $1\hbar$ of angular momentum. Note that the subscripts $\uparrow, \downarrow$ directly relate each particle to its spin value. Therefore, this notation describes the spatial part of the wavefunction after the measurement process where the the total wavefunction is projected on $|\uparrow\downarrow\rangle$.

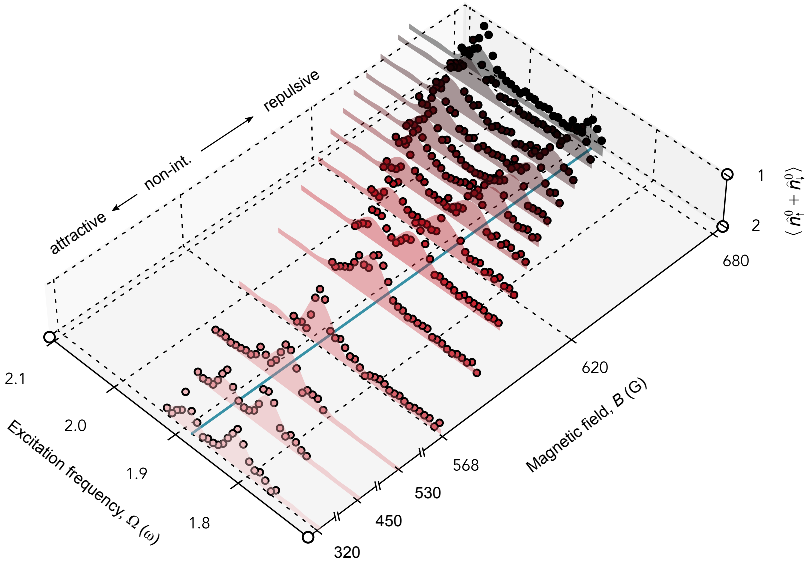

Figure 6.3: Excitation spectrum. Excitation spectrum of two fermions for various magnetic fields in the $L_z = 2\hbar$ manifold. The experimentally measured excitation frequencies are shifted by the numerically calculated ground state energy at the respective magnetic field. For visibility, the z-axis is inverted, hence a peak corresponds to atom loss. For increasing interactions the separation of the center-of-mass and relative excitation becomes more pronounced. The relative excitation stays approximately constant at $\Omega_{\text{rel}} \approx 1.9\omega$ indicated by the blue line. The magnetic field tunes the interactions strength from attractive (left side) to repulsive (right side). Note, the magnetic field is plotted with a non-linear scale to increase the visibility of the data.

We characterize the two fermions in the anharmonic potential spectroscopically by applying a rotating perturbation for $\tau = 350\,\mu\text{s}$ at different interactions strengths. The measured single-particle occupation number in the unperturbed ground state $\langle \hat{n}_\uparrow^0 + \hat{n}_\downarrow^0 \rangle$ is shown in Fig. 6.3. Experimentally, we measure the excitation frequency relative to the ground state energy which shifts with the magnetic field (see dashed arrow in Fig. 6.2b). To compare the excitation spectrum to the energy levels, we shift the experimentally measured excitation frequencies by the numerically calculated energy shift of the ground state as depicted in Fig. 6.2b. In the case of non-interacting particles at 568 G we observe a single resonance. However, tuning the interactions to be either repulsive ($> 568\,\text{G}$) or attractive ($< 568\,\text{G}$) results in a splitting to two resonances. In the limit of large interaction energies $E_{\text{int}} \gg \Delta$, these correspond to the center-of-mass $|2\rangle_{\text{com}}|0\rangle_{\text{rel}}$ and relative rotation $|0\rangle_{\text{com}}|2\rangle_{\text{rel}}$. The relative excitation does not tune with the interaction strength (within our model of the optical potential) highlighting the suppression of interactions, which is one of the defining properties of the Laughlin state. The resonance frequency is downshifted to $\Omega_{\text{rel}} \sim 1.9\omega$ due to the anharmonicity Δ compared to a harmonic potential where the resonance frequency is expected at 2ω. In contrast, the center-of-mass rotation tunes with the magnetic field from lower excitation frequencies $\Omega_{\text{com}} < \Omega_{\text{rel}}$ on the attractive side to larger excitation frequencies $\Omega_{\text{com}} > \Omega_{\text{rel}}$ on the repulsive branch. In order to prepare a clean Laughlin state $|0\rangle_{\text{com}}|2\rangle_{\text{rel}}$ it is required to separate the center-of-mass and relative excitations such that $|\Omega_{\text{com}}-\Omega_{\text{rel}}| \gg \Delta$. This condition is only achieved on the repulsive side at around 680 G where the scattering length of the hyperfine states $|F=1/2, m_{\text{F}}=1/2\rangle$ and $|F=3/2, m_{\text{F}}=3/2\rangle$ is $a_{\text{s}} \sim 20\,000 a_0$. In contrast, on the attractive side, the largest scattering length $a_{\text{s}} \sim -900 a_0$ is not large enough to fulfil the condition $|\Omega_{\text{com}}-\Omega_{\text{rel}}| \gg \Delta$. Let us remark that above the Feshbach resonance the attractive scattering length can take similarly large values as the repulsive scattering length below the Feshbach resonance.

We compare our experimental data to theory by computing the atom loss spectrum at various magnetic fields for a rotating perturbation of the LG_{02}-mode. In correspondence to the experiment, we calculate $\langle \hat{n}_\uparrow^0 + \hat{n}_\downarrow^0 \rangle$ after applying perturbation V_{p} for a duration time t_{p} in the frame rotating with half the excitation frequency. In the co-rotating frame, the time evolution of initial state is expressed as

$$|\psi(t)\rangle = e^{-i\left[H+V_p(0)-\frac{1}{2}\Omega L_z\right]\frac{t}{\hbar}}\,|0\rangle_{\text{com}}\,|0\rangle_{\text{rel}}^{B}\,, \tag{6.4}$$

where the angular momentum operator L_{z} appears. Here, $|0\rangle_{\text{rel}}^{B}$ relates to the interacting ground state which tunes with the magnetic field (see Fig. 6.2b). The numerical results are shown in Fig. 6.3 as shaded regions.

By ramping to a magnetic field of 680 G, we reach the limit $E_{\text{int}}/h \approx 9.9\,\text{kHz}$. In Fig. 6.4a we show the shifted excitation spectrum at 681 G where the red arrow indicates the resonance of the relative rotation. We drive Rabi oscillations at 680 G on the resonance $\Omega_{\text{rel}} \approx 1.9\omega$ with a Rabi rate $\Omega_{\text{rabi}}/2\pi \approx 0.42\,\text{kHz}$, shown in Fig. 6.4b. We transfer the repulsively interacting ground state to the Laughlin state via a $\pi-$pulse. Note that in contrast to the non-interacting fermions (see Fig. 5.4), the minimum of the Rabi oscillations reaches 0.5, following Eq. 6.3b. This is the first indication that the qualitiative nature of the rotating state changes compared to the non-interacting rotating fermions. From the Rabi oscillations, we can determine the coherence time $\tau_{\text{coh}} = 38(13)\,\text{ms}$ which exceeds the periodicity of the rabi oscillations $2\pi/\Omega_{\text{rabi}} \approx 2.4\,\text{ms}$ significantly. Furthermore, we infer an upper bound of the preparation fidelity through the single-particle occupation after half a Rabi cycle $F = 96(2)\,\%$. Here, we also take into account the preparation fidelity of two atoms in the ground state $F_{\text{gs}} = 95(3)\,\%$.

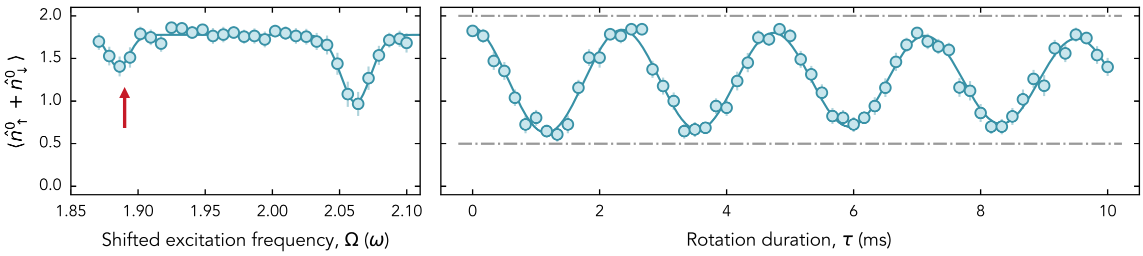

Figure 6.4: Rabi oscillations. a, Shifted excitation spectrum at 681 G. The separation of the relative rotation Ω_{rel} (red arrow) and the center-of-mass Ω_{com} are large compared to the anharmonicity Δ. **b**, Rabi oscillations between the repulsively interacting ground state and the Laughlin state at 680 G on the resonance $\Omega_{\text{rel}} \sim 1.9\omega$. We drive Rabi oscillations with a Rabi rate $\Omega_{\text{rabi}} \approx 0.42$ kHz. According to Eq. (6.3b) the Rabi oscillations occur between 2 and 0.5 (dashed lines).

.

The high preparation fidelity of the Laughlin state is rendered possible through the large separation of the relevant energy scales which follow the hierarchy

$$E_{\text{int}} \gg \Delta, \hbar\Omega_{\text{rabi}} \gg E_{\text{ani}}. \tag{6.5}$$

The interaction energy shift is required to be larger than the anharmonicity in order for the center-of-mass and relative coordinates to decouple. Furthermore, the Rabi rate needs to be smaller than energy shift to suppress coupling to the center-of-mass excitation. Lastly, the energy scales in Eq. (6.5) need to be larger than the anisotropy of the optical trap E_{ani} which breaks the rotational symmetry of the Hamiltonian. The effect of the anisotropy is discussed in more detail in section 6.3.

6.2 Observation of the Laughlin wavefunction

To measure the density of the $\nu = 1/2$ Laughlin wavefunction, we collect roughly 11 000 snapshots in momentum space after post-selection on the correct atom number (with an imaging fidelity $\sim 69\,\%$) to reconstruct the 2D density. Each snapshot is a projection of the wavefunction onto the momentum of the two particles. This enables us not only to measure the density of the Laughlin wavefunction through successive experimental realizations of the same quantum state but also to determine the wavefunction in the center-of-mass and relative coordinates. Furthermore, it allows us to study correlations

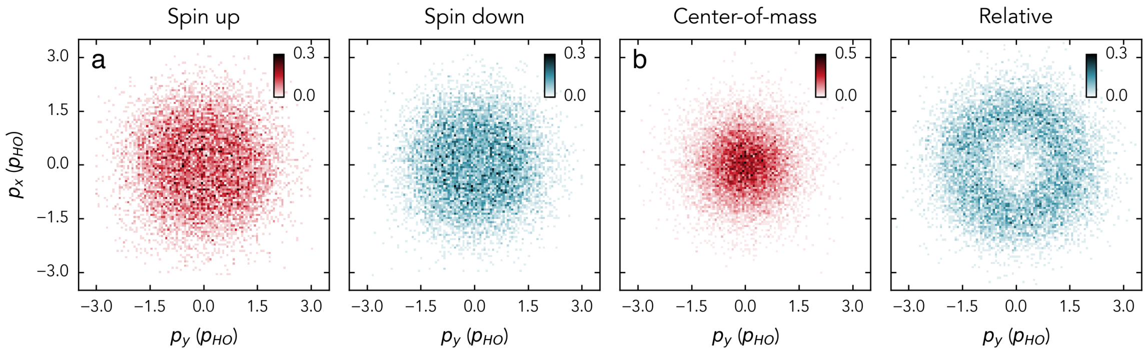

Figure 6.5: Observation of the Laughlin wavefunction. a, Normalized density of the spin up and spin down states. Both states exhibit a flattening of their density in the central region. **b,** Normalized density in the center-of-mass $\mathbf{p}_{\text{com}} = 1/\sqrt{2}(\mathbf{p}_\uparrow + \mathbf{p}_\downarrow)$ and relative basis $\mathbf{p}_{\text{rel}} = 1/\sqrt{2}(\mathbf{p}_\uparrow - \mathbf{p}_\downarrow)$. While in the center-of-mass coordinates, the density distribution exhibits a Gaussian shape, the incorporation of $2\hbar$ quanta of angular momentum in the relative motion manifests in a radially symmetric vortex distribution, which peaks at a radius of $\sqrt{2}p_{\text{HO}}$. At small relative momenta, a peak is visible corresponding to a $\sim 1\,\%$ admixture of a Feshbach molecule.

between the spin states. These observables reveal the striking microscopic features of the Laughlin wavefunction.

We sample the Laughlin wavefunction by deterministically preparing the same initial quantum state and subsequently initializing our atom- and spin-resolved momentum space imaging technique. To this end, we turn off the optical tweezer and let the system expand for a time-of-flight of 1.78 ms. During the expansion we quench on a 2D confinement which suppresses the expansion in the vertical direction. The atoms then expand in a combined potential of the 2D trap with a radial trap frequency of $\omega_{\text{r,2D}}/2\pi \approx 85\,\text{Hz}$ and the magnetic field saddle $\omega_{\text{r,M}} \approx 15\,\text{Hz}$. Similar to the previous chapter, we numerically solve the equation of motion of the particles in the combined potential. This yields the momentum of each spin state $\mathbf{p}_\uparrow, \mathbf{p}_\downarrow$ in each experimental realization. The calculation of the center-of-mass and relative momentum $\mathbf{p}_{\text{com}} = 1/\sqrt{2}(\mathbf{p}_\uparrow + \mathbf{p}_\downarrow)$ and $\mathbf{p}_{\text{rel}} = 1/\sqrt{2}(\mathbf{p}_\uparrow - \mathbf{p}_\downarrow)$, respectively, is then straightforward. If not mentioned otherwise, we express all momenta in units of the harmonic oscillator momentum $p_{\text{HO}} = \sqrt{\hbar m_{\text{Li}}\omega}$.

In Fig. 6.5, we show the normalized 2D density of the Laughlin wavefunction in the single-particle basis (**a**) and the center-of-mass and relative basis (**b**). In contrast to the non-interacting fermions, the 2D density in the single-particle basis does not exhibit a vortex distribution. On the contrary, the density profile flattens at the center. Furthermore, the density distribution of both spin states is identical up to experimental imperfections. These imperfections stem from off-resonant scattering of the spin up state during the prior imaging of the spin down state, resulting in a broadened density distribution.

The coordinate transformation to the center-of-mass and relative basis reveals the striking features of the Laughlin wavefunction. In the center-of-mass coordinates, the density exhibits a Gaussian shape, in stark contrast to the rotationally symmetric vortex distribution in the relative coordinates. The $\nu = 1/2$ Laughlin wavefunction incorporates $m = 2\hbar$ quanta of angular momentum leading to a peak of the vortex distribution at $\sqrt{m} p_{\mathrm{HO}} = \sqrt{2} p_{\mathrm{HO}}$, as a expected for a single-particle wavefunction in LLL. In addition, we also observe a small peak at zero momenta which stems from anharmonic coupling to molecular states with center-of-mass excitations during the magnetic field ramp from the non-interacting case at 568 G to repulsive interactions at 680 G (see also in the energy spectrum in Fig. 3.4).

6.3 Properties of the Laughlin state

Based on qualitative features, we have identified the observed state as the $\nu = 1/2$ Laughlin state. In the following section, we shift to a quantitative analysis of the experimental data, where we compare the radial densities with the theoretically expected Laughlin state densities. Furthermore, our imaging technique gives access to correlations between the particles which we utilize to analyze the pair and angle correlations of the Laughlin wavefunction. Last, we characterize the Laughlin state via Ramsey spectroscopy and compare its properties to the non-interacting rotating fermions and the center-of-mass rotating state.

6.3.1 Radial densities

To quantitatively compare the measured density of the Laughlin wavefunction with the theoretical prediction we azimuthally average the 2D densities in the single-particle basis and the center-of-mass and relative basis. We obtain the radial density n_{p} as a function of the radial momentum $p_{\mathrm{r}} = \sqrt{p_{\mathrm{x}}^2 + p_{\mathrm{y}}^2}$, shown in Fig. 6.6a,b. Note that the radial density n_{p} is normalized to $1/2\pi p_{\mathrm{HO}}^2$ due to the azimuthal average of the 2D density.

Similar to the previous chapter, we use a KDE to obtain the normalized radial density n_{p} from the 2D densities. We choose a *tophat* kernel with a bandwidth of $0.17 p_{\mathrm{HO}}$ slightly smaller than the average of the effective imaging resolution of both spin states.

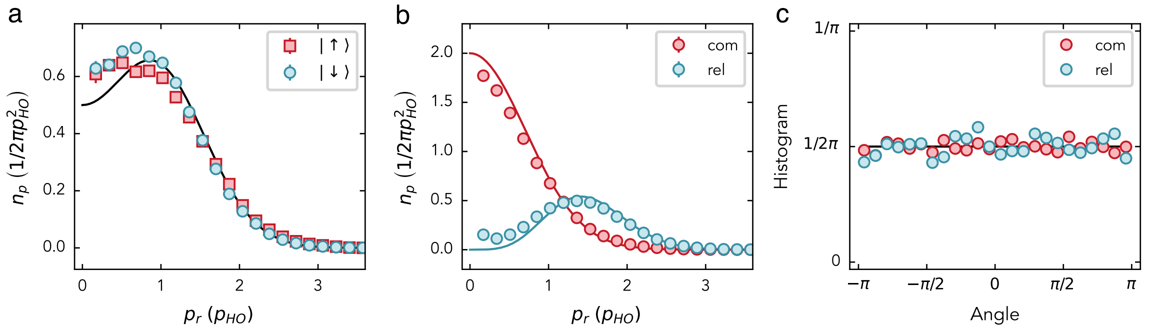

Figure 6.6: Azimuthally averaged radial densities. **a**, Radial densities of the spin up and spin down states. The black solid line is the prediction according to Eq. (6.3b). **b**, In the center-of-mass basis, the Laughlin state remains in the ground state $|0\rangle_{\text{com}}$, while it occupies the $|2\rangle_{\text{rel}}$ state in the relative basis, according to Eq. (6.3a). At small momenta, the relative density does not approach zero due to the Feshbach molecule.

Since the KDE normalizes $\int_0^\infty \tilde{n}_\text{p} \mathrm{d}p_\text{r} = 1$, we divide by the radial momentum p_r to obtain the radial density $n_\text{p} = \tilde{n}_\text{p}/p_\text{r}$ in momentum space, such that $\int_0^\infty p_\text{r} n_\text{p} \mathrm{d}p_\text{r} = 1$.

In the single-particle basis, the Laughlin state forms a superposition of states in the LLL, following Eq. 6.3b. The black solid line is the theoretical prediction for both spin states which only depends on the harmonic oscillator frequency ω, and agrees qualitatively with the data. A total amount of $2\hbar$ quanta of angular momentum is introduced into the system. Hence either, a single particle carries both quanta while the other one remains in the ground state or both particles share $1\hbar$ quantum of angular momentum. The flattening of the density profile is a result of the superposition of single-particle states in the LLL as the size of these states grows with increasing angular momentum $m\hbar$. The highest angular momentum state determines the cut-off at which the density decreases to zero. In particular in our case, the cut-off is set by $m = 2\hbar$ [Coo08], thus $n_\text{p}/2$ is reached at $\sqrt{2}p_\text{HO}$. The radial densities of the spin up and spin down fermion are identical, except for a broadening of the imaging resolution of the spin up state, already discussed above. This is most visible at small momenta, where a peak in the density is visible for the spin down state while this effect is barely discernible in the density of the spin up state.

In the center-of-mass basis, the Laughlin state stays in the ground state $|0\rangle_\text{com}$, while it incorporates $2\hbar$ quanta of angular momentum in the relative motion, thus occupying the $|2\rangle_\text{rel}$, in accordance with Eq. (6.3a). For $p_\text{r} \to 0$, the presence of a Feshbach molecule leads to an increase in density in contrast to the theoretically expected convergence to zero. Azimuthal inhomogeneities caused by a superposition with the counter-clockwise rotating state $|-2\rangle$ are not visible in the radial density. To reveal defects in the azimuthal distributions of both the center-of-mass and relative basis, we integrate the 2D density along the radial direction, shown in Fig. 6.6c. Both densities are flat along the azimuthal angle.

6.3.2 Emergence of fractional quantum Hall states

Exploring how the two-particle Laughlin state approaches the many-body limit is an intriguing question. In our case, we do not reach a Laughlin state in the many-body limit due to the fermionic spin, but rather a so-called Halperin state [Hal83b]. However, in the two-particle limit of spinful fermions, the Laughlin state and the Halperin state are identical. This section aims to assess the essential characteristics of the many-body Laughlin state that persist down to the few-particle limit.

In order to relate the two-particle Laughlin state to the many-body limit, we transform the momentum space units to real space and express the system in units of the magnetic length $l_B = \sqrt{\hbar / m_{\mathrm{Li}} 2\omega}$. This is possible since the two-particle Laughlin wavefunction is an eigenstate of the harmonic oscillator and therefore expands self-similar. Therefore, we calculate the two-particle density in real space defined as $\tilde{n}_{\mathrm{r}} = n_{\mathrm{r}\uparrow} + n_{\mathrm{r}\downarrow}$, shown in Fig. 6.7, where $n_{\mathrm{r}\uparrow}, n_{\mathrm{r}\downarrow}$ is the single-particle density in real space of the spin up and spin down state, respectively.

We determine the analytical expression of the single-particle density of an arbitrarily chosen particle within the N-particle system. More precisely, we integrate out the phase of all N particles and the radii of $N-1$ particles. In the special case of $N = 2$ the single-particle density then reads

$$\tilde{n}_{\mathrm{r}}(r_1) = \frac{1}{A} \int \mathrm{d}\varphi_1 \int \mathrm{d}r_2 \int \mathrm{d}\varphi_2 r_2 \left| \psi_{1/2} \left(r_1, \varphi_1, r_2, \varphi_2 \right) \right|^2 \tag{6.6a}$$

$$= \frac{8 + 8r_1^2 + r_1^4}{16} e^{-r_1^2/2}, \tag{6.6b}$$

where A is the normalization constant. This terms grows quite fast with increasing atom number and is therefore not displayed for more particles. Instead, we plot the analytical solution of the single-particle density in Fig. 6.7, up to 4 particles. Eq. (6.6b) consists of a product of two terms, a sum of polynomials and a Gaussian envelope. The latter term corresponds to the edge which falls off to zero on a length scale given by the magnetic length l_{B}, independent of the particle number. The former term is a sum of even polynomials, up to the order of the maximum angular momentum $2M$ in the system, while only even polynomials contribute due to the absolute square of the

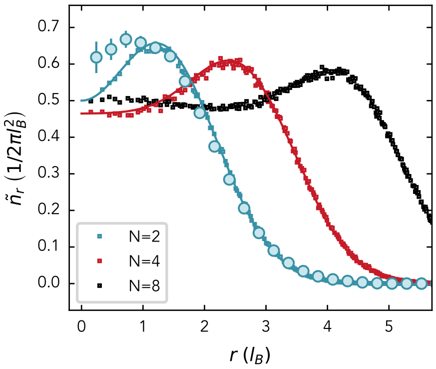

Figure 6.7: Emergence of the many-body Laughlin state. Comparison of the measured two-particle density $\tilde{n}_{\mathrm{r}}$ in real space (blue circles) with the analytical prediction (blue and red solid lines for $N = 2, 4$) and the MC simulation [Tom18] (squares) for $N = 2, 4, 8$ particles. For increasing particles, the separation of the bulk density and the edge of the FQH droplet manifests. The slope of the edge stays constant for all particle numbers.

wavefunction. The number of terms in the sum scales quadratically with the particle number and causes the flat central density.

In addition to the analytical solution, we calculate the single-particle densities by means of MC simulation [Tom18] for up to 8 particles, shown in Fig. 6.7. Both theoretical predictions lie on top of each other and are in qualitative agreement with the experimental data of $N = 2$ particles.

One of the most prominent properties of the many-body Laughlin wavefunction is the incompressibility of the bulk density [Lau83]. Strikingly, the bulk density of the many-body Laughlin wavefunction $\psi_{1/m}$ is flat at a value $1/m$, when expressed in the natural units of l_{B}, and extends up to a radius $2\sqrt{N-1}l_{\mathrm{B}}$ [Coo08]. Following the narrative from above, the flat central density at $1/m$ persists for small atom numbers, in particular in the case of $N = 2$, our measured value of $2\pi l_{\mathrm{B}}^2 \tilde{n}_r(r \to 0) \approx 0.6$ is close to the expected value of $1/2$. Increasing the atom number numerically by means of MC simulation [Tom18] shows that the bulk density remains at approximately $1/2$ while the edge extends to larger radii. Therefore, a flat bulk in the single-particle density of an increasing number of atoms confined in a harmonic potential is an indication of a FQH state.

In the region of the edge, the density first increases before it falls off to zero at a length scale of the magnetic length. This effect persists down to the two particle case, visible in the experimental data. In the many-body limit, this indicates the onset of compressibility of the edge [Wen04]. In general, the separation of the bulk and edge is subtle in the few-particle limit, and only with increasing particle number this distinction becomes more pronounced.

6.3.3 Pair correlations

The excitation spectrum of FQH states consists of density waves which exhibit a collective excitation gap at zero and a magneto-roton minimum at finite momenta [Gir89]. In a series of papers [Gir84; Gir85; Gir86], Girvin et al. demonstrated that the low momentum properties of the static structure factor $s(k)$ in the LLL are intimately related to the finite excitation gap. In particular, a suppression of the quadratic term in the structure factor, leading to

$$s(k) \propto k^4, \tag{6.7}$$

provides a necessary condition for the existence of a finite gap. In the case where no low-lying single-particle excitations are present, which is reasonable to assume due to the kinetic energy being quenched by the magnetic field, Eq. (6.7) becomes a sufficient condition. In a physical picture, the structure factor corresponds to the amplitude of a density wave with wave vector k. The suppression of density waves at long wavelengths $k \to 0$ causes the incompressibility of the fluid and is the origin of the collective excitation gap of the FQH states. Considering the preceding discussion, we pose the question of whether our observables grant us access to the structure factor, and consequently infer a statement on the incompressibility of our two-particle Laughlin state.

The structure factor is a natural observable in the context of solid state systems as it is accessible via neutron scattering [Pap22]. In ultracold atomic systems, the detection of real space correlation function $g^{(2)}(\boldsymbol{r})$ is well established [Föl14], which is related by a Fourier transformation to [Giu12]

$$s(k) = 1 + n \int \left[g(\boldsymbol{r}) - 1\right] e^{-i\boldsymbol{k}\cdot\boldsymbol{r}} \mathrm{d}^2 r, \tag{6.8}$$

where n is the particle density. By sampling the Laughlin wavefunction, we access correlations between the particles, subtly demonstrated in the previous section by the transformation of the single particle density to center-of-mass and relative coordinates. Here, we determine the pair correlation function $g^{(2)}(z_\uparrow, z_\downarrow)$ by measuring the relative distance of the two particles in each experimental realization and normalize it by the single-particle densities $\langle n_\uparrow \rangle \langle n_\downarrow \rangle$. Integrating out the center-of-mass coordinate and utilizing the azimuthal symmetry of the system, we can reduce the pair correlation function from a four- to a one-dimensional object, which then only depends on the

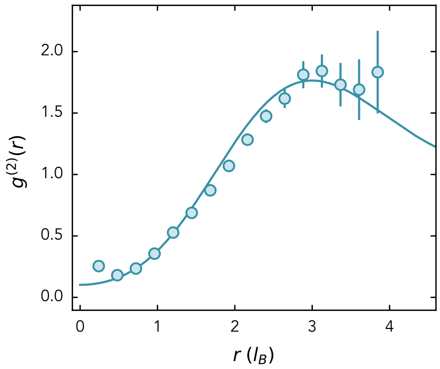

Figure 6.8: Pair correlations. Pair correlations of the $\nu = 1/2$ Laughlin state consisting of two particles. The solid lines is a fit according to Eq. (6.10) restricted to the two lowest Haldane amplitudes A_0, A_2.

relative radius r of the two particles

$$g^{(2)}(r) = \frac{\langle n_\uparrow(0) n_\downarrow(r)\rangle}{\langle n_\uparrow\rangle \langle n_\downarrow\rangle}, \tag{6.9}$$

where the position of the spin up fermion is fixed at $r = 0$. Similar to the previous section, we express the quantities in real space and in units of the magnetic length l_B.

In a translational and rotational invariant system in the LLL, the pair correlation function can be expressed as a sum of single particle densities in the LLL $\propto r^{2m} e^{-r^2/4l_\mathrm{B}^2}$ weighted by the Haldane pair amplitudes A_m [Hal87], which yields [Gir84; Hof23]

$$g^{(2)}(r) = 1 + e^{-r^2/2l_\mathrm{B}^2} + \frac{1}{\nu^2} \sum_{m \in \mathrm{even}} \frac{2}{m!} \left(\frac{r}{2l_\mathrm{B}}\right)^{2m} e^{-r^2/4l_\mathrm{B}^2} \left(A_m - \nu^2\right), \tag{6.10}$$

for particles with a symmetric spatial wavefunction (bosons, or in our case two spinful fermions in the spin singlet state). The Haldane amplitudes relate to the number of particle pairs with relative angular momentum m, are independent of the center-of-mass angular momentum, and determine the strength of the mth single particle density. Furthermore, the above expression guarantees that $g^{(2)}(r \to \infty) = 1$, since $A_m \to \nu^2$ for $m \gg 1$ [Hal87].

The Eq. (6.10) allows us to determine the Haldane amplitudes from the measured pair correlations. Due to the small system size we restrict the series expansion to the two lowest values A_0 and A_2. This is justified since the single particle densities localize at a radius $r = \sqrt{4m} l_\mathrm{B}$ and their contribution falls of rapidly for $m \geq 4$.

In Fig. 6.8, we show the experimentally measured pair correlations and the fit of the theoretical prediction that lead to the Haldane amplitudes $A_0 = 0.013(7)$ and $A_2 = 0.65(2)$. Here, A_0 is close to the theoretically expected value $A_0^{\mathrm{th}} = 0$ of the many-body $\nu = 1/2$ Laughlin state. Hence, no pairs with angular momentum $m = 0$ are expected to enter the Laughlin state. However, taking into account only the lowest amplitudes is not sufficient to make a sophisticated statement about the incompressibility. Measuring the pair correlations for large particle numbers and large radii yields access to higher-order Haldane amplitudes and thus the low momentum limit of the structure factor $s(k)$ in Eq. (6.7). We conclude that the lowest Haldane amplitude A_0 is in agreement with theoretical expectation of the Laughlin wavefunction, however these concepts become more relevant when approaching the many-body limit, which allows us then to identify an observable which demonstrates the incompressibility of the FQH state.

6.3.4 Angle correlations

The particles described by the Laughlin wavefunction are a prime example of motionally entangled states [Pop04]. The particles are entangled in real space in contrast to many other atomic platforms where the states are entangled in internal space. In our case of the two-particle wavefunction $\psi_{1/m}$, the correlations that arise are quantified by the normalized angle correlation function $g_{1/m}$ where the radii $r_\uparrow, r_\downarrow$ of the spin states are integrated out. Specifically, the unnormalized angle correlation function is defined as

$$\begin{aligned} G_{1/m}(\varphi) \equiv \int \mathrm{d}r_\uparrow \int \mathrm{d}\phi_\uparrow \int \mathrm{d}r_\downarrow \\ r_\uparrow r_\downarrow \, |\psi_{1/m}(r_\uparrow, \phi_\uparrow, r_\downarrow, \phi_\uparrow - \varphi)|^2, \end{aligned} \tag{6.11}$$

where we integrate out $r_\uparrow$ and $r_\downarrow$, as well as the angle of the spin up fermion $\phi_\uparrow$. The relative angle φ between the two spin states characterizes the correlations. This yields

$$\begin{aligned} G_{1/m}(\varphi) &= 2\pi \int \mathrm{d}r_\uparrow \int \mathrm{d}r_\downarrow \\ &\quad r_\uparrow r_\downarrow \, (r_\uparrow^2 + r_\downarrow^2 - 2 r_\uparrow r_\downarrow \cos\varphi)^m e^{-(r_\uparrow^2 + r_\downarrow^2)} \\ &= \frac{\pi}{2} \sum_{k=0}^{m} \sum_{q=0}^{m-k} \binom{m}{k} \binom{m-k}{q} \\ &\quad (-2\cos\varphi)^k \Gamma\left(1 - \frac{k}{2} + m - q\right) \Gamma\left(1 + \frac{k}{2} + q\right). \end{aligned}$$

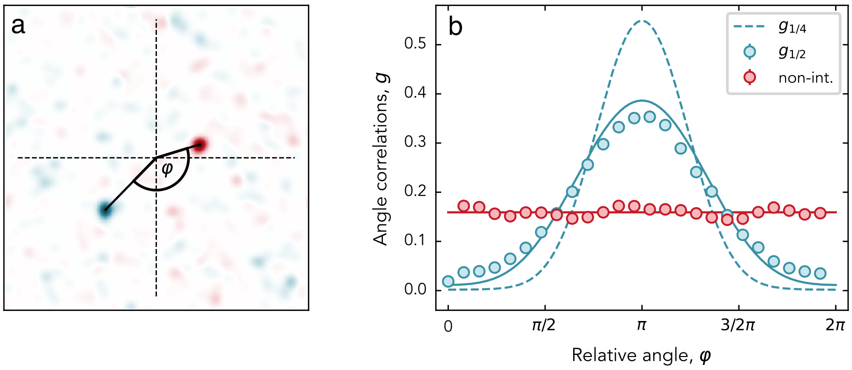

Figure 6.9: Angle correlations. a, Example snapshot of the Laughlin wavefunction where the relative angle φ is shown. **b**, Normalized histogram of relative angle correlations of the Laughlin wavefunction (blue) between the spin up and spin down state. The solid line (dashed line) is the theoretical angle correlation function $g_{1/2}(\varphi)$ $(g_{1/4}(\varphi))$, see text. As a reference, the angle correlations of the non-interacting rotating fermions are shown (red). As expected, we find a flat distribution.

We make sure that the correlation function $g_{1/m}(\varphi)$ is normalized such that

$$g_{1/m}(\varphi) = \frac{G_{1/m}(\varphi)}{\int \mathrm{d}\varphi \; G_{1/m}(\varphi)}.$$

In our case of $m = 2$, we arrive at the relative angle correlation function

$$g_{1/2}(\varphi) = \frac{6 - 3\pi\cos(\varphi) + 4\cos^2(\varphi)}{16\pi}. \tag{6.12}$$

Our free-space imaging technique allows us to extract the relative angle correlations between the spin up and spin down fermions. For that, we determine the relative angle between the two particles in each experimental realization, illustrated in Fig. 6.9a, where an exemplary snapshot of the Laughlin wavefunction is chosen. In Fig. 6.9b, we show the normalized angle distribution of the Laughlin wavefunction $\psi_{1/2}$ calculated with a KDE. The theoretically expected distribution is represented by the blue solid line without any free-parameters. To illustrate that the two-particle Laughlin wavefunction $\psi_{1/m}$ genuinely exhibits a distinctive peak at a relative angle $\varphi = \pi$, we additionally show the case $m = 4$ (blue dashed line) which becomes narrower the larger the angular momentum in the system. Geometrically, the particles tend to increase the relative distance while the center-of-mass distribution remains the same. Hence, the angle correlations become narrower.

As reference, we show the angle correlations of the non-interacting rotating fermions (red) which is a flat line, as expected. Ironically, in the context of our zero-range interactions both states are non-interacting. However, the Laughlin state distinguishes itself dramatically from a trivial non-interacting state. Only due to incorporation of angular momentum in the particles' relative degree of freedom the interaction energy of the state becomes zero, however strong correlations, that were absent in the case of the initially non-interacting fermions, emerge in the motional degree of freedom.

6.3.5 Ramsey spectroscopy

We have shown that the density of the Laughlin wavefunction remains in the ground state in the center-of-mass frame, while it shows a characteristic vortex distribution in relative coordinates, suggesting the imprint of a phase winding in the relative degree of freedom. However, similar arguments as in section 5.3 apply, that is the density distribution alone does not directly indicate rotation. To show that the prepared state is indeed the Laughlin state we investigate its time evolution.

We use the same protocol as in section 5.3. In a nutshell, we pulse to the Laughlin state and let it evolve in a slightly anisotropic trap after which we de-excite the state to the ground state. The anisotropy is incorporated into the model of the optical potential by introducing a term $2\epsilon(x^2 - y^2)/w_0^2$, where w_0 is the waist of the tweezer and ϵ is the strength of the perturbation. This term breaks the radial symmetry of the optical potential and couples angular momentum states $\Delta m = \pm 2$ to first order in ϵ by a strength δ_2. To second order in ϵ, it couples angular momentum states $\Delta m = \pm 4$ with a strength δ_4. Therefore, states in the $L_\mathrm{z} = 2\hbar$ manifold which carry $2\hbar$ quanta of angular momentum (both clockwise and counter-clockwise rotating) couple to states with $0\hbar$ quanta of angular momentum. The $|+2\rangle$ state only couples to the $|-2\rangle$ state to second order in ϵ. This process is sketched in Fig. 6.10a. We define the anisotropy by

$$\delta\omega = 2\delta_4 - 2\frac{\delta_2^2}{\Delta'}, \tag{6.13}$$

where Δ' corresponds to the detuning to the $0\hbar$ angular momentum state. Interactions tune the energy levels with $0\hbar$ quanta of angular momentum with respect to states with non-zero quanta of angular momentum. If the detuning is large enough, the effective coupling in primarily given by δ_4 and therefore solely between the degenerate $|0\rangle_\mathrm{com} |\pm 2\rangle_\mathrm{rel}$ states. In that scenario, the new eigenstates of the two level system are formed by the states $|\pm\rangle = |0\rangle_\mathrm{com} (|2\rangle_\mathrm{rel} \pm |2\rangle_\mathrm{rel})$ which can be depicted on a Bloch

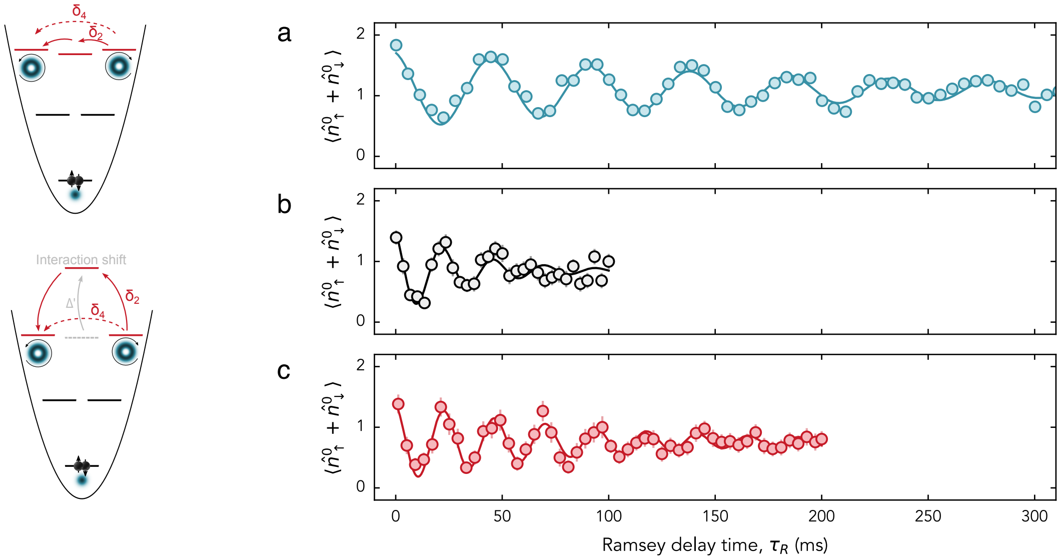

Figure 6.10: Ramsey spectra. On the left, sketch of the coupling of the anisotropy without (upper panel) and with an interactions shift (lower panel). **a**, Ramsey spectrum of the Laughlin state. We measure an anisotropy of $\delta\omega/2\pi = 21.4(1)\,\mathrm{Hz}$ at a trap frequency $\omega/2\pi \approx 56.1\,\mathrm{kHz}$ yielding a relative anisotropy $\delta\omega/\omega = 4 \times 10^{-4}$. The coherence time is $\tau_{\mathrm{coh}} = 191(21)\,\mathrm{ms}$, corresponding to 21 430 coherent oscillations. **b**, Ramsey spectrum of two non-interacting particles at 568 G. We measure an oscillation frequency of $\delta\omega^{(\text{non-int})}/2\pi = 42(1)\,\mathrm{Hz}$. The coherence time is $\tau_{\mathrm{coh}}^{(\text{non-int})} = 33(8)\,\mathrm{ms}$. **c**, Ramsey spectrum of the center-of-mass excitation $|2\rangle_{\mathrm{com}}|0\rangle_{\mathrm{rel}}$ at 680 G. We measure an oscillation frequency of $\delta\omega^{(\mathrm{com})}/2\pi = 42.0(2)\,\mathrm{Hz}$. The coherence time is $\tau_{\mathrm{coh}}^{(\mathrm{com})} = 87(12)\,\mathrm{ms}$.

sphere. It is worth highlighting that the described protocol only works if the duration of the $\pi-$pulse is much shorter than the time scale set by the anisotropic coupling of the different states.

We apply the Ramsey protocol to three different cases, the Laughlin state (blue), the non-interacting rotating fermions (black) and the center-of-mass rotating state $|2\rangle_{\mathrm{com}}\,|0\rangle_{\mathrm{rel}}$ at 680 G (red), shown in Fig. 6.10a-c, respectively. In all three cases we observe coherent oscillations confirming that we prepare states with non-zero angular momentum. Let us first highlight the properties of the Laughlin state, which can be better appreciated when placed in the context of the other two scenarios. We measure an anisotropy of $\delta\omega/2\pi = 21(4)\,\mathrm{Hz}$ at a trap frequency $\omega/2\pi \approx 56.1\,\mathrm{kHz}$. This yields a

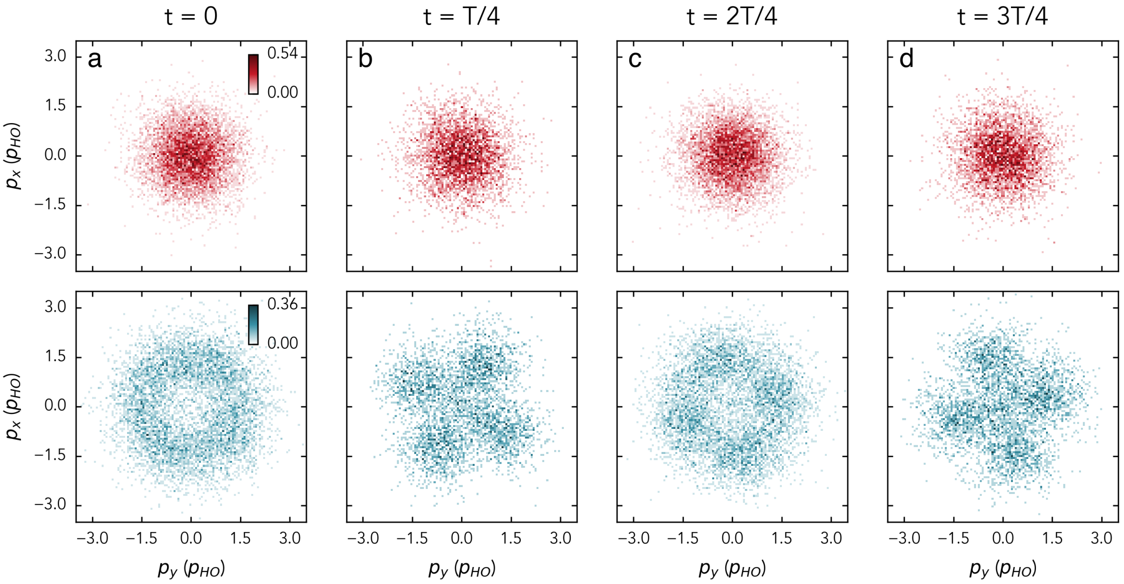

Figure 6.11: Time evolution of the Laughlin wavefunction. Density distribution in center-of-mass (red) and relative (blue) basis at different times. In the center-of-mass basis, the ground state remains stationary. In the relative basis, the density evolves according a state prepared on the eq to a two-level system formed by the states $|\pm\rangle$.

relative anisotropy of $\delta\omega/\omega = 4 \times 10^{-4}$. The oscillation frequency of the non-interacting rotating fermions is $\delta\omega^{\text{non-int}}/2\pi = 42(1)\,\text{Hz}$, similar to the center-of-mass excitation $|2\rangle_{\text{com}}\,|0\rangle_{\text{rel}}$ which is $\delta\omega^{\text{com}}/2\pi = 42.0(2)\,\text{Hz}$. As outlined above, the reduction in the oscillation frequency of the Laughlin state is due to the energy shift of the non-zero angular momentum state $|2, 0\rangle$ which suppresses the coupling from the state $|2\rangle$ to $|{-2}\rangle$.

Even more remarkable is the coherence time of the Laughlin state $\tau_{\text{coh}} = 191(2)\,\text{ms}$ corresponding to 21 400 coherent rotations of the particles around each other. This demonstrates that already the two-particle Laughlin state is well isolated from environmental noise sources. We also determine the coherence time of the non-interacting rotating fermions $\tau_{\text{coh}}^{(\text{non-int})} = 33(8)\,\text{ms}$ and of the center-of-mass excitation $\tau_{\text{coh}}^{(\text{com})} = 87(12)\,\text{ms}$. Intriguingly, the coherence time of Laughlin state exceeds both other states by at least a factor of 2. The Laughlin state is a non-interacting state since its energy level is flat as a function of the magnetic field, as shown in Fig. 6.3. In contrast to the other two states which show a magnetic field dependence. This highlights that the two-particle Laughlin state lives in a decoherence-free subspace, i.e. a subspace which is insensitive to linear shifts of the magnetic field [Mam20; Har22].

In addition to the spectroscopic tool for the characterization of the Laughlin state, we measure the time evolution of the Laughlin wavefunction at Ramsey delay times $\tau_\mathrm{R} = nT/4$, with $n \in \{0, 1, 2, 3\}$ and $T = 2\pi/\delta\omega$. In Fig. 6.11, we show the density of the Laughlin wavefunction in the center-of-mass (red) and relative (blue) basis. As expected, the center-of-mass motion remains stationary in time. The relative part however is oscillating according to the sketch in Fig. 6.10.

Conclusion

We have realized the $\nu = 1/2$ Laughlin state with two spinful fermions rapidly rotating in an optical tweezer. Our single particle and spin resolved imaging technique allowed us to directly observe microscopic correlations of the Laughlin wavefunction. We have demonstrated multiple key properties, including the ground state distribution in center-of-mass coordinates, the incorporation of angular momentum in the relative motion of the particles, as well as the resulting suppression of interacting energy and its strongly correlated nature in the motional degree of freedom.

These measurements demonstrate the first realization of a Laughlin state in a rotating ultracold quantum gas, with access to microscopic observables of the underlying system. They lay the foundation for the realization of fractional quantum Hall states in ultracold atoms with deterministic control of the particle number, as well as the precise tunability of the interaction strength.

7

Summary and Outlook

The realization of a Laughlin state with two spinful fermionic atoms, demonstrated in this thesis, establishes the groundwork for future studies on strongly-correlated many-body fractional quantum Hall states with rotating ultracold atomic gases. Access to the microscopic details was achieved by directly probing the Laughlin wavefunction with single atom and spin resolution. This revealed its pair and angle correlations (see chapter 6), thereby yielding novel observables for fractional quantum Hall states with the potential to unravel currently unanswered questions of the quantum Hall effect [Pap22; Ma24].

Two key technological developments made the realization of the Laughlin state in our experiment possible. First, it was necessary to determine the optical aberrations by using the *quantum gas as a wavefront sensor*. To achieve this, we implemented a phase shift interferometry algorithm from which we retrieved a phase map of the light propagating through the optical elements up to the position of the atoms (see chapter 4). Most critical was the ellipticity of the optical potential set by the anisotropy of the trap frequencies in the horizontal plane and which required further reduction. To this end, we used Ramsey interferometry which allowed us to measure and reduce the ellipticity down to a relative anisotropy of $\sim 10^{-4}$ (see chapter 5 and 6). Second, we demonstrated the *motional control of the angular momentum eigenstate* of a single atom in a tightly focused optical tweezer. We implemented a novel technique which relies on the interference of Laguerre-Gaussian beams, to transfer angular momentum from the light field to the atoms (see chapter 4 and 5). This technique grants us full control over the strength of the rotating perturbation, as well as the rotation frequency and the order of the Laguerre-Gaussian beam, that is the amount of angular momentum inserted into the system.

In the following, we present a selection of applications which are either directly in reach or require minor modifications to the current experimental setup.

7.1 Quasihole excitations

The quasiparticle excitations of FQH states, also referred to as anyons [Wil82; Aro84; Hal84], obey fractional exchange statistics when two of them are interchanged, which was recently measured experimentally in solid state systems [Bar20; Nak20]. Ultracold atomic gases, on the other hand, might offer the required control to deterministically prepare a certain number of quasiholes and to not only measure their fractional phase by braiding them [Par01] but also to exploit their properties for quantum information applications [Kit03; Fre02]. Here, we outline a procedure to deterministically prepare a single quasihole excitation in the two-particle Laughlin state.

Recall that a central quasihole excitation on the $\nu = 1/2$ two-particle Laughlin state $\psi_{1/2}$ is described by the wavefunction

$$\begin{aligned} \psi_{1/2}^{(\mathrm{hole})}(z_1, z_2) &= z_1 z_2 (z_1 - z_2)^2 e^{-1/2(|z_1|^2+|z_2|^2)} && (7.1)\\ &\propto z_1^3 z_2 + z_1 z_2^3 - 2 z_1^2 z_2^2, && (7.2)\end{aligned}$$

where in the second line, we factored out the terms in the brackets and omitted the Gaussian envelope. Rewriting this state in center-of-mass and relative coordinates as defined in section 6.2 allows us to identify the quasihole wavefunction with states of the 2D harmonic oscillator in the LLL

$$\begin{aligned} \psi_{1/2}^{(\mathrm{hole})}(z_{\mathrm{com}}, z_{\mathrm{rel}}) &\propto z_{\mathrm{com}}^2 z_{\mathrm{rel}}^2 - \sqrt{6} z_{\mathrm{rel}}^4 && (7.3)\\ &\simeq |2\rangle_{\mathrm{com}} |2\rangle_{\mathrm{rel}} - \sqrt{6}\, |0\rangle_{\mathrm{com}} |4\rangle_{\mathrm{rel}} . && (7.4)\end{aligned}$$

Hence, the quasihole is a superposition of two states of the 2D harmonic oscillator in the $4\hbar$ angular momentum manifold. Since both states contain relative angular momentum the quasihole is non-interacting and in the case of a harmonic trap these states are degenerate.

In contrast to the Laughlin state, which exhibits a flat density for small radii in the single particle basis, the quasihole excitation exhibits a density depletion, as shown in Fig. 7.1, where we compare the radial densities of the two particle Laughlin wavefunction $\psi_{1/2}$ and the quasihole excitation $\psi_{1/2}^{(\mathrm{hole})}$. Furthermore, the center-of-mass density does not remain in the ground state and the additional angular momentum manifests in a shift of the relative density to higher radii.

In order to prepare the state, it is required to additionally insert $2\hbar$ quanta of angular momentum on top of the Laughlin state. In principle, this can be achieved with a second π-pulse to the $4\hbar$ manifold which can be resolved spectroscopically as the rotation frequency from the Laughlin state to the quasihole differs from the de-excitation to the ground state (for clarification, see Fig. 3.4b). While observing a single quasihole

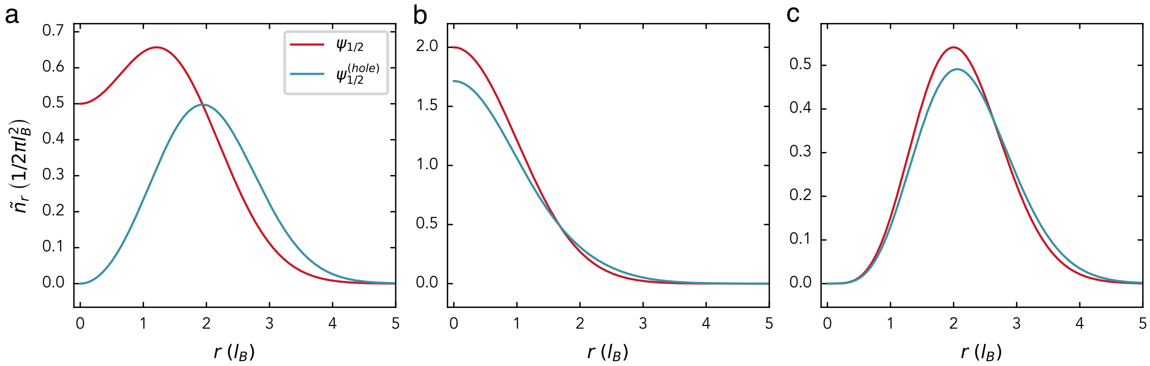

Figure 7.1: Quasihole excitation. Comparing the radial density of the two particle Laughlin state $\psi_{1/2}$ (red) to a quasihole excitation $\psi_{1/2}^{(\text{hole})}$ (blue) in **a**, single particle coordinates **b**, the center-of-mass coordinates and **c**, relative coordinates. At the position of the quasihole $r = 0$, the single particle density exhibits a depletion in contrast to the Laughlin state which reaches a density given by the filling factor.

excitation in the two-particle Laughlin state sets the foundation for exploring its exotic properties, preparing multiple quasiholes requires a larger number of particles to distribute them across the bulk density of the Laughlin state.

7.2 Increasing the particle number

Some properties of the many-body FQH states persist even down to two particles. These include that the single particle density approaches for small radii the value of the filling factor $\nu = 1/2$, in units of the magnetic length, or the incorporation of angular momentum in the relative motion of the particles. However, in order to observe thermodynamic properties such as the quantized Hall conductance or the excitation spectrum, large particle numbers on the order ten are required [Hal85]. We outline the required technical advances in our experiment to prepare a many-body FQH state and provide an overview of various applications on our platform.

Quasi-2D regime From a technical point of view, it is necessary to reach a quasi-2D trap geometry. In the current setup, we use a single, tightly focused optical tweezer with an aspect ratio $\omega/\omega_z \approx 7$ of the radial to axial trap frequency. In the case of two spinful fermions the assumption that the atoms remain in the axial ground state is justified as the rotation couples only to the in-plane motion. However, when adding another particle by using our spilling technique, the system is not in the axial ground state anymore. Therefore, it is necessary to implement an additional confinement in the axial direction to invert the aspect ratio such that $\omega \ll \omega_\mathrm{z}$. Such an optical potential was already built in our experiment [Kle21]. It has been shown on another machine in our group that it is possible to prepare stable ground states in 2D [Bay20a] up to 20 atoms with such a potential geometry.

Spin polarized Fermi gases Once we reach the quasi-2D regime in our experiment, there is a variety of possible future directions. The simplest is to start from a closed shell configuration of the 2D harmonic oscillator with spin polarized fermions corresponding to $1, 3, 6, 10, ...$ atoms in the ground state and to transfer all of the atoms to the LLL. This coincides with an incompressible IQH state as the filling factor is $\nu = 1$. The density displays a flat profile reflecting the occupation of the single particle states in the LLL [Ho00]. Even though this might be a trivial state to start with, it is helpful for benchmarking adiabatic protocols to prepare many fermions in the LLL.

Spinfull fractional quantum Hall states The addition of the second spin state allows for introducing repulsive interactions among the different spin components. A balanced mixture of $N_\uparrow$ spin up and $N_\downarrow$ spin down particles with relative angular momentum among each and every particle correspond to states observed in the spinful FQH effect, which are described by the Halperin wavefunction (see chapter 2). In particular, in reference [Pal20] they propose a scheme to adiabatically transfer a system of $N_\uparrow + N_\downarrow$ particles to the so-called skyrmion ground state which exhibits local ferromagnetic order and long-range reversed spin order.

BEC-BCS crossover in the LLL In a non-rotating system, the BCS state consisting of weakly bound pairs of fermions is smoothly connected to a BEC of diatomic molecules [Joc03; Gre03; Zwi03]. However, if all fermions occupy the LLL it is predicted that the evolution from the BCS to BEC side involves a topological quantum phase transition, rather than a crossover [Möl07; Yan08; Ho16; Rep17]. Here, the transition is expected from a $\nu = 1/2$ Laughlin state of molecules on the BEC side to a fermionic integer quantum Hall state with a filling factor $\nu_\uparrow = \nu_\downarrow = 1$ for each spin state on the BCS.

7.3 Superfluidity in finite systems

So far, we have focused on the rapidly rotating limit at which strongly-correlated states analogous to FQH states are anticipated [Coo08]. In the non-rotating limit and for large particles numbers, the system is expected to exhibit a superfluid ground state in the BCS-BEC crossover [Zwi05; Ket08]. Investigating the response of a mesoscopic system to a slowly rotating perturbation allows to explore the emergence of superfluidity from the single particle limit.

A superfluid does not rotate like an ordinary fluid. If the rotation frequency Ω of the confining potential remains below a critical rotation frequency $\Omega < \omega_c$, the superfluid stays at rest. However, if the rotation frequency exceeds ω_c, quantized vortices nucleate on top of the superfluid. This state state is infinitely long lived since it constitutes the new ground state in the rotating frame. The conditions on the critical rotation frequency and the lifetime are known as Landau's criteria of superfluidity [Pit16].

Intriguingly, these criteria also hold for a single atom in the ground state which is transferred to an angular momentum eigenstate of a radially symmetric harmonic oscillator, similar to chapter 5 and 6. The atom remains in the ground state of the system if the rotation frequency of the perturbation remains below the trap frequency ω, thus corresponding to ω_c. Furthermore, the angular momentum eigenstate carries quantized amount of angular momentum and is infinitely long lived as it corresponds to an eigenstate of the harmonic oscillator.

The beautiful experiments carried out with Bose Einstein condensates [Mad00; Abo01] and strongly interacting Fermi gases [Zwi05; Rie10] with large number of particles can provide inspiration and incentives to discriminate between single particle and superfluid effects. In particular, in two-component strongly interacting Fermi gases a series of important measurements hinted towards superfluidity [OHa02; Reg04; Zwi04; Bar04; Kin04; Chi04] but do not provide an unambiguous proof. A *smoking gun* for superfluidity, on the other hand, is the manifestation of a long lived Abrikosov lattice, the arrangement of many quantized flux vortices in a triangular lattice, observed in a BEC [Abo01] and in a Fermi gas [Zwi05]. Another evident observable for superfluidity is the reduction of the moment of inertia with respect to the classical rigid body below the nucleation frequency of vortices [Rie10], closely related to measurements in nuclear systems [Str18]. Given that our system in the thermodynamic limit is expected to constitute a superfluid the question arises whether these observables persist in the few-particle regime at temperatures close to zero.

Inspired by the measurements in [Rie10], in which they use the precession of the quadrupole mode to measure the inserted angular momentum L in the system and from that determine the moment of inertia defined as $I = L/\Omega$, we conducted first experiments on the excitation of a radial quadrupole mode in a system of few-fermions

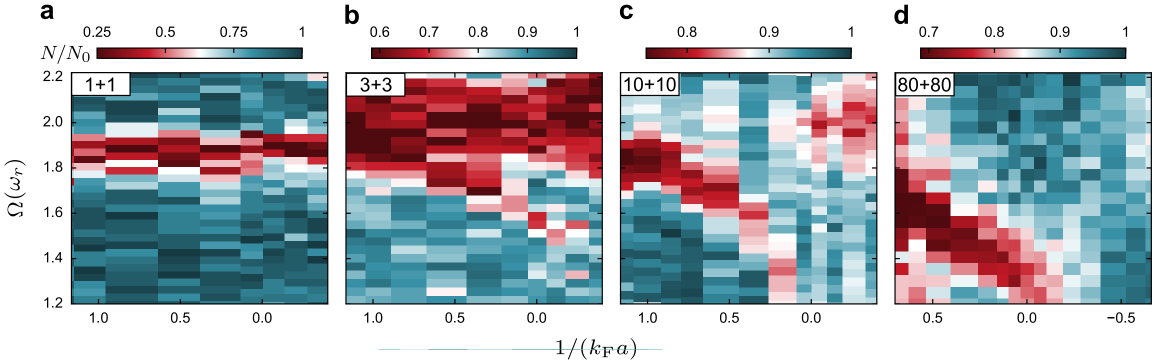

Figure 7.2: Emergence of the quadrupole mode. Excitation spectrum of the radial quadrupole mode in the BEC-BCS crossover for varying atom numbers by using atom loss spectroscopy. The excitation frequency Ω is expressed in units of the radial trap frequency ω, while the scattering length a is normalized to the Fermi momentum k_{F}. As the atom number is increased (left to right) the quadrupole mode reveals the qualitative change of the system's response from collective to single particle behaviour indicated by the sudden transition of the resonance frequency, adapted from [Rei23].

in the BEC-BCS crossover, shown in Fig. 7.2. Here, we use atom loss spectroscopy to measure the resonance frequency of the quadrupole mode, indicated by a loss of atoms (in red). The excitation scheme is similar as in [Bay20a]. We observe a qualitative change of the system's response with increasing atom number in the BEC-BCS crossover, indicated by a sudden transition of the resonance frequency.

In particular, the single particle limit of $1 + 1$ atoms exhibits no dependence on the interactions expressed in terms of the fermi momentum k_{F} of the non-interacting system and the scattering length a_{s}. With increasing particle number two branches emerge. On the BEC side, an interaction dependent branch associated to the quadrupole mode appears at excitation frequencies $\Omega < 2\omega$ which is absent in the single particle limit. At weaker interactions towards the BCS side, we observe a discontinuity of the quadrupole mode at which the resonance frequency suddenly transitions to $\Omega \approx 2\omega$, reminiscent of the single particle excitations in the $1+1$ case. This qualitative change in the response of the system suggests the transition from a collective behaviour on the BEC side to single particle excitations on the weakly interacting BCS side.

Measurements of the collective excitations [Bar04; Alt07; Tey13] hint towards superfluid behaviour, however as outlined above, are not a smoking gun. These experiments provide us with a reference in terms of particle numbers and interaction strengths at which we might expect to observe either a reduction of the moment of inertia due to the superfluid properties of these small systems or even an Abrikosov lattice of a few vortices.

Appendix A

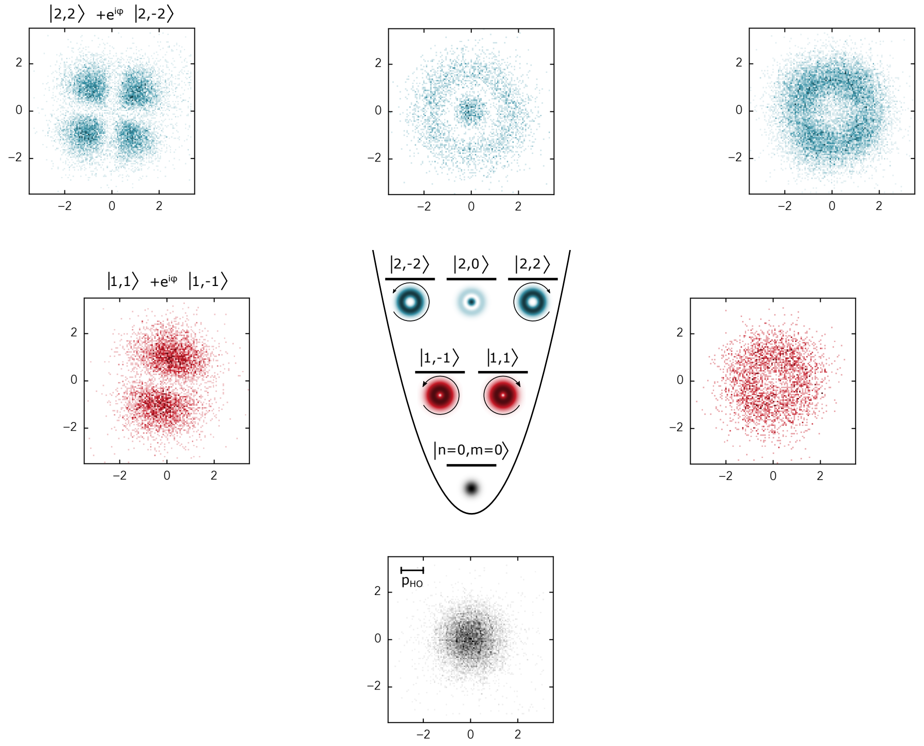

Figure A.1: Quantum control of 2D harmonic oscillator states. We showcase the quantum control of a single atom in a 2D harmonic oscillator. Starting point is a single atom in the ground state $|i\rangle = |00\rangle$ of the optical potential. We engineer various perturbations $\hat{V}_{\text{pert}}$ via the SLM to couple the ground state to the desired final stated $\langle i|\hat{V}_{\text{pert}}|f\rangle$, which we then image via our fluorescene imaging technique in momentum space. The units for all densities are in p_{HO}. The colours mark the shell quantum numbers – black $n = 0$, red $n = 1$ and blue $n = 2$.

Bibliography

[Abo01] J. R. Abo-Shaeer, C. Raman, J. M. Vogels, and W. Ketterle. *Observation of Vortex Lattices in Bose-Einstein Condensates*. *Science* 292.5516 (2001), pp. 476–479.

[Aha59] Y. Aharonov and D. Bohm. *Significance of Electromagnetic Potentials in the Quantum Theory*. *Phys. Rev.* 115 (3 1959), pp. 485–491.

[Aid13a] M. Aidelsburger, M. Atala, M. Lohse, J. T. Barreiro, B. Paredes, and I. Bloch. *Realization of the Hofstadter Hamiltonian with Ultracold Atoms in Optical Lattices*. *Physical Review Letters* 111.18 (2013).

[Aid11] M. Aidelsburger, M. Atala, S. Nascimbène, S. Trotzky, Y.-A. Chen, and I. Bloch. *Experimental Realization of Strong Effective Magnetic Fields in an Optical Lattice*. *Phys. Rev. Lett.* 107 (25 2011), p. 255301.

[Aid13b] M. Aidelsburger, M. Atala, S. Nascimbène, S. Trotzky, Y.-A. Chen, and I. Bloch. *Experimental realization of strong effective magnetic fields in optical superlattice potentials*. *Applied Physics B* 113.1 (2013), pp. 1–11.

[Aid14] M. Aidelsburger, M. Lohse, C. Schweizer, M. Atala, J. T. Barreiro, S. Nascimbène, N. R. Cooper, I. Bloch, and N. Goldman. *Measuring the Chern number of Hofstadter bands with ultracold bosonic atoms*. *Nature Physics* 11.2 (2014), pp. 162–166.

[Aid18] M. Aidelsburger, S. Nascimbene, and N. Goldman. *Artificial gauge fields in materials and engineered systems*. *Comptes Rendus. Physique* 19.6 (2018), pp. 394–432.

[Alt04] E. Altman, E. Demler, and M. D. Lukin. *Probing many-body states of ultracold atoms via noise correlations*. *Physical Review A* 70.1 (2004), p. 013603.

[Alt07] A. Altmeyer, S. Riedl, M. J. Wright, C. Kohstall, J. H. Denschlag, and R. Grimm. *Dynamics of a strongly interacting Fermi gas: The radial quadrupole mode*. *Phys. Rev. A* 76 (3 2007), p. 033610.

[And72] P. W. Andersen. *More is different*. *Science* 177.4047 (1972), pp. 393–396.

[And95] M. H. Anderson, J. R. Ensher, M. R. Matthews, C. E. Wieman, and E. A. Cornell. *Observation of Bose-Einstein condensation in a dilute atomic vapor*. *Science* 269.5221 (1995), pp. 198–201.

[Aro84] D. Arovas, J. R. Schrieffer, and F. Wilczek. *Fractional Statistics and the Quantum Hall Effect*. *Phys. Rev. Lett.* 53 (7 1984), pp. 722–723.

[Ast19] L. Asteria, D. T. Tran, T. Ozawa, M. Tarnowski, B. S. Rem, N. Fläschner, K. Sengstock, N. Goldman, and C. Weitenberg. *Measuring quantized circular dichroism in ultracold topological matter*. *Nature Physics* 15.5 (2019), pp. 449–454.

[Bal10] L. Balents. *Spin liquids in frustrated magnets*. *Nature* 464.7286 (2010), pp. 199–208.

[Bar12] M. A. Baranov, M. Dalmonte, G. Pupillo, and P. Zoller. *Condensed Matter Theory of Dipolar Quantum Gases*. *Chemical Reviews* 112.9 (2012), pp. 5012–5061.

[Bar04] M. Bartenstein, A. Altmeyer, S. Riedl, S. Jochim, C. Chin, J. H. Denschlag, and R. Grimm. *Collective excitations of a degenerate gas at the BEC-BCS crossover*. *Physical Review Letters* 92.20 (2004).

[Bar20] H. Bartolomei et al. *Fractional statistics in anyon collisions*. *Science* 368.6487 (2020), pp. 173–177.

[Bau80] M. Baus and J.-P. Hansen. *Statistical mechanics of simple coulomb systems*. *Physics Reports* 59.1 (1980), pp. 1–94.

[Bay20a] L. Bayha, M. Holten, R. Klemt, K. Subramanian, J. Bjerlin, S. M. Reimann, G. M. Bruun, P. M. Preiss, and S. Jochim. *Observing the emergence of a quantum phase transition shell by shell*. *Nature* 587.7835 (2020), pp. 583–587.

[Bay20b] L. X. Bayha. *Emergence of Many-Body Physics in Two-Dimensional Few-Fermion Systems*. PhD thesis. University of Heidelberg, 2020.

[Bay04] G. Baym. *Vortex lattices in rapidly rotating Bose-Einstein condensates: Modes and correlation functions*. *Phys. Rev. A* 69 (4 2004), p. 043618.

[Bec20a] J. H. Becher, E. Sindici, R. Klemt, S. Jochim, A. J. Daley, and P. M. Preiss. *Measurement of Identical Particle Entanglement and the Influence of Antisymmetrization*. *Phys. Rev. Lett.* 125 (18 2020), p. 180402.

[Bec20b] J. H. W. Becher. *Characterizing Few-Fermion Systems with Momentum Correlations*. PhD thesis. University of Heidelberg, 2020.

[Ber03] T. Bergeman, M. G. Moore, and M. Olshanii. *Atom-Atom Scattering under Cylindrical Harmonic Confinement: Numerical and Analytic Studies of the Confinement Induced Resonance*. *Phys. Rev. Lett.* 91 (16 2003), p. 163201.

[Ber17] A. Bergschneider. *Strong correlations in few-fermion systems*. PhD thesis. University of Heidelberg, 2017.

[Ber19] A. Bergschneider, V. M. Klinkhamer, J. H. Becher, R. Klemt, L. Palm, G. Zürn, S. Jochim, and P. M. Preiss. *Experimental characterization of two-particle entanglement through position and momentum correlations*. *Nature Physics* 15.7 (2019), pp. 640–644.

[Ber18] A. Bergschneider, V. M. Klinkhamer, J. H. Becher, R. Klemt, G. Zürn, P. M. Preiss, and S. Jochim. *Spin-resolved single-atom imaging of ^{6}Li in free space*. *Physical Review A* 97.6 (2018), p. 063613.

[Ber84] M. V. Berry. *Quantal phase factors accompanying adiabatic changes*. *Proceedings of the Royal Society of London. A. Mathematical and Physical Sciences* 392.1802 (1984), pp. 45–57.

[Bij13] R. M. W. Bijnen van. *Quantum engineering with ultracold atoms*. PhD thesis. Eindhoven University of Technology, 2013.

[Blo12] I. Bloch, J. Dalibard, and S. Nascimbène. *Quantum simulations with ultracold quantum gases*. *Nature Physics* 8.4 (2012), pp. 267–276.

[Blo08] I. Bloch, J. Dalibard, and W. Zwerger. *Many-body physics with ultracold gases*. *Reviews of Modern Physics* 80.3 (2008), pp. 885–964.

[Bra23] S. Brandstetter et al. *Emergent hydrodynamic behaviour of few strongly interacting fermions*. 2023.

[Bre04] V. Bretin, S. Stock, Y. Seurin, and J. Dalibard. *Fast Rotation of a Bose-Einstein Condensate*. *Phys. Rev. Lett.* 92 (5 2004), p. 050403.

[Bro20] A. Browaeys and T. Lahaye. *Many-body physics with individually controlled Rydberg atoms*. *Nature Physics* 16.2 (2020), pp. 132–142.

[Bru74] J. H. Bruning, D. R. Herriott, J. E. Gallagher, D. P. Rosenfeld, A. D. White, and D. J. Brangaccio. *Digital Wavefront Measuring Interferometer for Testing Optical Surfaces and Lenses*. *Appl. Opt.* 13.11 (1974), pp. 2693–2703.

[Bus98] T. Busch, B. G. Englert, K. Rzazewski, and M. Wilkens. *Two Cold Atoms in a Harmonic Trap*. *Foundations of Physics* 28.4 (1998), pp. 549–559.

[Cha20] T. Chalopin, T. Satoor, A. Evrard, V. Makhalov, J. Dalibard, R. Lopes, and S. Nascimbene. *Probing chiral edge dynamics and bulk topology of a synthetic Hall system*. *Nature Physics* 16.10 (2020), pp. 1017–1021.

[Che10] X. Chen, Z.-C. Gu, and X.-G. Wen. *Local unitary transformation, long-range quantum entanglement, wave function renormalization, and topological order*. *Phys. Rev. B* 82 (15 2010), p. 155138.

[Chi15] C.-C. Chien, S. Peotta, and M. Di Ventra. *Quantum transport in ultracold atoms*. *Nature Physics* 11.12 (2015), pp. 998–1004.

[Chi04] C. Chin, M. Bartenstein, A. Altmeyer, S. Riedl, S. Jochim, H. H. Denschlag, and R. Grimm. *Observation of the pairing gap in a strongly interacting Fermi gas*. *Science* (2004).

[Chi10] C. Chin, R. Grimm, P. Julienne, and E. Tiesinga. *Feshbach resonances in ultracold gases*. *Reviews of Modern Physics* 82.2 (2010), pp. 1225–1286.

[Cho22] L. Chomaz, I. Ferrier-Barbut, F. Ferlaino, B. Laburthe-Tolra, B. L. Lev, and T. Pfau. *Dipolar physics: a review of experiments with magnetic quantum gases*. *Reports on Progress in Physics* 86.2 (2022), p. 026401.

[Cla20] L. W. Clark, N. Schine, C. Baum, N. Jia, and J. Simon. *Observation of Laughlin states made of light*. *Nature* 582.7810 (2020), pp. 41–45.

[Coo20] N. Cooper. *Fractional Quantum Hall States of Bosons: Properties and Prospects for Experimental Realization*. In: *Fractional Quantum Hall effects – New Developments*. Ed. by B. I. Halperin and J. K. Jain. World Scientific, 2020, pp. 487–521.

[Coo19] N. R. Cooper, J. Dalibard, and I. B. Spielman. *Topological bands for ultracold atoms*. *Rev. Mod. Phys.* 91 (1 2019), p. 015005.

[Coo01] N. R. Cooper, N. K. Wilkin, and J. M. F. Gunn. *Quantum Phases of Vortices in Rotating Bose-Einstein Condensates*. *Phys. Rev. Lett.* 87 (12 2001), p. 120405.

[Coo08] N. Cooper. *Rapidly rotating atomic gases*. *Advances in Physics* 57.6 (2008), pp. 539–616.

[Dal16] J. Dalibard. *Introduction to the physics of artificial gauge fields*. In: *Quantum Matter at Ultralow Temperatures*. Ed. by M. Inguscio, W. Ketterle, S. Stringari, and G. Roati. Proceedings of the International School of Physics Enrico Fermi. IOS Press, 2016, pp. 1–61.

[Dal99] J. Dalibard. *Collisional dynamics of ultra-cold atomic gases*. In: *Proceedings of the International School of Physics - Enrico Fermi*. 1999, pp. 321–349.

[Dav95] K. B. Davis, M. O. Mewes, M. R. Andrews, N. J. Van Druten, D. S. Durfee, D. M. Kurn, and W. Ketterle. *Bose-Einstein condensation in a gas of sodium atoms*. *Physical Review Letters* 75.22 (1995), pp. 3969–3973.

[DeM99] B. DeMarco and D. S. Jin. *Onset of Fermi Degeneracy in a Trapped Atomic Gas*. *Science* 285.5434 (1999), pp. 1703–1706.

[Don91] R. J. Donnelly. *Quantized vortices in helium II*. Vol. 2. Cambridge University Press, 1991.

[Dru00] P. Drude. *Zur Elektronentheorie der Metalle*. *Annalen der Physik* 306.3 (1900), pp. 566–613.

[Dux] D. Dux. *Towards the construction of rapidly rotating optical dipole traps*. Bachelor Thesis. University of Heidelberg.

[Fan86] G. Fano, F. Ortolani, and E. Colombo. *Configuration-interaction calculations on the fractional quantum Hall effect*. *Phys. Rev. B* 34 (4 1986), pp. 2670–2680.

[Fet03] A. L. Fetter, J. D. Walecka, and L. P. Kadanoff. *Quantum Theory of Many Particle Systems*. Dover: Dover Publications, 2003. ISBN: 9780486134758.

[Fey72] R. P. Feynman. *Statistical Mechanics: a set of lectures*. Benjamin, Reading, Mass., 1972.

[Fle21] R. J. Fletcher, A. Shaffer, C. C. Wilson, P. B. Patel, Z. Yan, V. Crépel, B. Mukherjee, and M. W. Zwierlein. *Geometric squeezing into the lowest Landau level*. *Science* 372.6548 (2021), pp. 1318–1322.

[Föl14] S. Fölling. *Quantum Noise Correlation Experiments with Ultracold Atoms*. In: 2014, pp. 145–177.

[Fre02] M. H. Freedman, A. Kitaev, M. J. Larsen, and Z. Wang. *Topological Quantum Computation*. 2002.

[Gau13] A. L. Gaunt, T. F. Schmidutz, I. Gotlibovych, R. P. Smith, and Z. Hadzibabic. *Bose-Einstein Condensation of Atoms in a Uniform Potential*. *Physical Review Letters* 110.20 (2013).

[Geh03] M. E. Gehm. *Properties of ^{6}Li*. *Jetlab* (2003), pp. 1–33.

[Gem10] N. Gemelke, E. Sarajlic, and S. Chu. *Rotating Few-body Atomic Systems in the Fractional Quantum Hall Regime*. 2010.

[Geo14] I. M. Georgescu, S. Ashhab, and F. Nori. *Quantum simulation*. *Rev. Mod. Phys.* 86 (1 2014), pp. 153–185.

[Gin50] V. L. Ginzburg and L. D. Landau. *To the Theory of Superconductivity*. *Zh. Eksp. Teor. Fiz.* 20 (1950), p. 1064.

[Gir84] S. M. Girvin. *Anomalous quantum Hall effect and two-dimensional classical plasmas: Analytic approximations for correlation functions and ground-state energies*. *Phys. Rev. B* 30 (2 1984), pp. 558–560.

[Gir85] S. M. Girvin, A. H. MacDonald, and P. M. Platzman. *Collective-Excitation Gap in the Fractional Quantum Hall Effect*. *Phys. Rev. Lett.* 54 (6 1985), pp. 581–583.

[Gir86] S. M. Girvin, A. H. MacDonald, and P. M. Platzman. *Magneto-roton theory of collective excitations in the fractional quantum Hall effect*. *Phys. Rev. B* 33 (4 1986), pp. 2481–2494.

[Gir89] S. Girvin and R. Prange. *The Quantum Hall Effect*. New York: Springer New York, NY, 1989. ISBN: 978-0-387-97177-3.

[Giu12] G. Giuliani and G. Vignale. *Quantum Theory of the Electron Liquid*. Cambridge Univ. Press, 2012.

[Gol14] N. Goldman, G. Juzeliūnas, P. Öhberg, and I. B. Spielman. *Light-induced gauge fields for ultracold atoms*. *Reports on Progress in Physics* 77.12 (2014), p. 126401.

[Gol16] N. Goldman, J. C. Budich, and P. Zoller. *Topological quantum matter with ultracold gases in optical lattices*. *Nature Physics* 12.7 (2016), pp. 639–645.

[Gol62] J. Goldstone, A. Salam, and S. Weinberg. *Broken Symmetries*. *Physical Review* 127.3 (1962), pp. 965–970.

[Gou16] T. Gould and T. Bučko. *C6 Coefficients and Dipole Polarizabilities for All Atoms and Many Ions in Rows 1–6 of the Periodic Table*. *Journal of Chemical Theory and Computation* 12.8 (2016), pp. 3603–3613.

[Gre02] M. Greiner, O. Mandel, T. Esslinger, T. W. Hänsch, and I. Bloch. *Quantum phase transition from a superfluid to a Mott insulator in a gas of ultracold atoms*. *Nature* 415.6867 (2002), pp. 39–44.

[Gre03] M. Greiner, C. A. Regal, and D. S. Jin. *Emergence of a molecular Bose–Einstein condensate from a Fermi gas*. *Nature* 426.6966 (2003), pp. 537–540.

[Gri07] R. Grimm. *Ultracold Fermi gases in the BEC-BCS crossover: A review from the Innsbruck perspective*. In: *Ultra-cold Fermi Gases*. Ed. by C. S. M. Inguscio W. Ketterle. Proceedings of the International School of Physics Enrico Fermi. IOS Press, 2007, pp. 413–462.

[Gri99] R. Grimm, M. Weidemüller, and Y. B. Ovchinnikov. *Optical dipole traps for neutral atoms*. 1999.

[Gro21a] C. Gross and W. S. Bakr. *Quantum gas microscopy for single atom and spin detection*. *Nature Physics* 17.12 (2021), pp. 1316–1323.

[Gro21b] C. Gross and W. S. Bakr. *Quantum gas microscopy for single atom and spin detection*. *Nature Physics* 17.12 (2021), pp. 1316–1323.

[Hal87] D. Haldane. *The Hierarchy of Fractional States and Numerical Studies*. In: *The Quantum Hall Effect*. Ed. by R. E. Prange and S. Girvin. Springer, 1987, pp. 303–352.

[Hal83a] F. D. M. Haldane. *Fractional Quantization of the Hall Effect: A Hierarchy of Incompressible Quantum Fluid States*. *Phys. Rev. Lett.* 51 (7 1983), pp. 605–608.

[Hal85] F. D. M. Haldane and E. H. Rezayi. *Finite-Size Studies of the Incompressible State of the Fractionally Quantized Hall Effect and its Excitations*. *Phys. Rev. Lett.* 54 (3 1985), pp. 237–240.

[Hal88] F. D. M. Haldane and E. H. Rezayi. *Spin-singlet wave function for the half-integral quantum Hall effect*. *Phys. Rev. Lett.* 60 (10 1988), pp. 956–959.

[Hal17] F. D. M. Haldane. *Nobel Lecture: Topological quantum matter*. *Rev. Mod. Phys.* 89 (4 2017), p. 040502.

[Hal79] E. H. Hall. *On a New Action of the Magnet on Electric Currents*. *American Journal of Mathematics* 2.3 (1879), pp. 287–292.

[Hal82] B. I. Halperin. *Quantized Hall conductance, current-carrying edge states, and the existence of extended states in a two-dimensional disordered potential*. *Phys. Rev. B* 25 (4 1982), pp. 2185–2190.

[Hal83b] B. I. Halperin. *Theory of the quantized Hall conductance*. *Helv. Phys. Acta* 56 (1983), pp. 75–102.

[Hal84] B. I. Halperin. *Statistics of Quasiparticles and the Hierarchy of Fractional Quantized Hall States*. *Phys. Rev. Lett.* 52 (18 1984), pp. 1583–1586.

[Har22] T. Hartke, B. Oreg, N. Jia, and M. Zwierlein. *Quantum register of fermion pairs*. *Nature* 601.7894 (2022), pp. 537–541.

[Has10] M. Z. Hasan and C. L. Kane. *Colloquium: Topological insulators*. *Rev. Mod. Phys.* 82 (4 2010), pp. 3045–3067.

[Hil24] P. Hill, P. Lunt, J. Reiter, M. Gałka, and S. Jochim. *Optical Phase Aberration Correction with an Ultracold Quantum Gas*. *in preparation* (2024).

[Hil21] P. Hill. *Towards Physics of the Fractional Quantum Hall Effect in Rotating Few-Fermion Systems* . Master Thesis. University of Heidelberg, 2021.

[Ho01] T.-L. Ho. *Bose-Einstein Condensates with Large Number of Vortices*. *Phys. Rev. Lett.* 87 (6 2001), p. 060403.

[Ho16] T.-L. Ho. *Fusing Quantum Hall States in Cold Atoms*. 2016.

[Ho00] T.-L. Ho and C. V. Ciobanu. *Rapidly Rotating Fermi Gases*. *Phys. Rev. Lett.* 85 (22 2000), pp. 4648–4651.

[Hod01] E. Hodby, G. Hechenblaikner, S. A. Hopkins, O. M. Maragò, and C. J. Foot. *Vortex Nucleation in Bose-Einstein Condensates in an Oblate, Purely Magnetic Potential*. *Phys. Rev. Lett.* 88 (1 2001), p. 010405.

[Hof23] J. Hofmann and W. Zwerger. *Scale Invariance in the Lowest Landau Level*. *Comptes Rendus. Physique* 24.S3 (2023), pp. 1–18.

[Hol17] M. Holten. *Collective Modes and Turbulence in Two-Dimensional Fermi Gases*. Master Thesis. University of Heidelberg, 2017.

[Hol22] M. Holten. *From Pauli Blocking to Cooper Pairs: Emergence in a Mesoscopic 2D Fermi Gas*. PhD thesis. University of Heidelberg, 2022.

[Hol21] M. Holten, L. Bayha, K. Subramanian, S. Brandstetter, C. Heintze, P. Lunt, P. M. Preiss, and S. Jochim. *Observation of Cooper Pairs in a Mesoscopic 2D Fermi Gas*. *ArXiv Preprint* 2109.11511 (2021).

[Hub16] S. D. Huber. *Topological mechanics*. *Nature Physics* 12.7 (2016), pp. 621–623.

[Hue18] K. Hueck, N. Luick, L. Sobirey, J. Siegl, T. Lompe, and H. Moritz. *Two-Dimensional Homogeneous Fermi Gases*. *Physical Review Letters* (2018).

[Hum13] D. B. Hume, I. Stroescu, M. Joos, W. Muessel, H. Strobel, and M. K. Oberthaler. *Accurate Atom Counting in Mesoscopic Ensembles*. *Physical Review Letters* 111.25 (2013), p. 253001.

[Idz05] Z. Idziaszek and T. Calarco. *Two atoms in an anisotropic harmonic trap*. *Phys. Rev. A* 71 (5 2005), p. 050701.

[Idz06] Z. Idziaszek and T. Calarco. *Analytical solutions for the dynamics of two trapped interacting ultracold atoms*. *Physical Review A* 74.2 (2006), p. 022712.

[Jai89] J. K. Jain. *Composite-fermion approach for the fractional quantum Hall effect*. *Phys. Rev. Lett.* 63 (2 1989), pp. 199–202.

[Jak98] D. Jaksch, C. Bruder, J. I. Cirac, C. W. Gardiner, and P. Zoller. *Cold Bosonic Atoms in Optical Lattices*. *Phys. Rev. Lett.* 81 (15 1998), pp. 3108–3111.

[Jan16] Jan Hendrik Willibald Becher. *Towards Spin and Site-Resolved, Single-Atom Imaging of ^{6}Li Atoms in a Multiwell Potential*. Master Thesis. University of Heidelberg, 2016.

[Jas55] R. Jastrow. *Many-Body Problem with Strong Forces*. *Phys. Rev.* 98 (5 1955), pp. 1479–1484.

[Jim12] K. Jimenez-Garcia, L. J. LeBlanc, R. A. Williams, M. C. Beeler, A. R. Perry, and I. B. Spielman. *Peierls Substitution in an Engineered Lattice Potential*. *Phys. Rev. Lett.* 108 (22 2012), p. 225303.

[Joc03] S. Jochim, M. Bartenstein, A. Altmeyer, G. Hendl, S. Riedl, C. Chin, J. Hecker Denschlag, and R. Grimm. *Bose-Einstein Condensation of Molecules*. *Science* 302.5653 (2003), pp. 2101–2103.

[Jot14] G. Jotzu, M. Messer, R. Desbuquois, M. Lebrat, T. Uehlinger, D. Greif, and T. Esslinger. *Experimental realization of the topological Haldane model with ultracold fermions*. *Nature* 515.7526 (2014), pp. 237–240.

[Kau21] A. M. Kaufman and K.-K. Ni. *Quantum science with optical tweezer arrays of ultracold atoms and molecules*. *Nature Physics* 17.12 (2021), pp. 1324–1333.

[Ken15] C. J. Kennedy, W. C. Burton, W. C. Chung, and W. Ketterle. *Observation of Bose–Einstein condensation in a strong synthetic magnetic field*. *Nature Physics* 11.10 (2015), pp. 859–864.

[Ket99] W. Ketterle, D. S. Durfee, and D. M. Stamper-Kurn. *Making, probing and understanding Bose-Einstein condensates*. 1999.

[Ket08] W. Ketterle and M. W. Zwierlein. *Making, probing and understanding ultracold Fermi gases*. *Rivista del Nuovo Cimento* 31.5-6 (2008), pp. 247–422.

[Kin04] J. Kinast, S. L. Hemmer, M. E. Gehm, A. Turlapov, and J. E. Thomas. *Evidence for Superfluidity in a Resonantly Interacting Fermi Gas*. *Phys. Rev. Lett.* 92 (15 2004), p. 150402.

[Kit03] A. Kitaev. *Fault-tolerant quantum computation by anyons*. *Annals of Physics* 303.1 (2003), pp. 2–30.

[Kjø99] H. Kjønsberg and J. Myrheim. *Numerical study of charge and statistics of Laughlin quasiparticles*. *International Journal of Modern Physics A* 14.04 (1999), pp. 537–557.

[Kla22] L. Klaus, T. Bland, E. Poli, C. Politi, G. Lamporesi, E. Casotti, R. N. Bisset, M. J. Mark, and F. Ferlaino. *Observation of vortices and vortex stripes in a dipolar condensate*. *Nature Physics* 18.12 (2022), pp. 1453–1458.

[Kle21] R. Klemt. *Correlations from Microscopic to Macroscopic Quantum Systems: Interactions vs Indistinguishability*. PhD thesis. University of Heidelberg, 2021.

[Kli80] K. v. Klitzing, G. Dorda, and M. Pepper. *New Method for High-Accuracy Determination of the Fine-Structure Constant Based on Quantized Hall Resistance*. *Phys. Rev. Lett.* 45 (6 1980), pp. 494–497.

[Kli93] K. von Klitzing. *The Quantized Hall effect.* From Nobel Lectures, Physics 1981-1990, Editor-in-Charge Tore Frängsmyr, Editor Gösta Ekspong, World Scientific Publishing Co., Singapore (1993).

[Kli20] K. von Klitzing et al. *40 years of the quantum Hall effect*. *Nature Physics Reviews* 2.8 (2020), pp. 397–401.

[Kön07] M. König, S. Wiedmann, C. Brüne, A. Roth, H. Buhmann, L. W. Molenkamp, X.-L. Qi, and S.-C. Zhang. *Quantum Spin Hall Insulator State in HgTe Quantum Wells*. *Science* 318.5851 (2007), pp. 766–770.

[Lan36] L. Landau. *The theory of phase transitions*. *Nature* 138.3498 (1936), pp. 840–841.

[Lan37] L. Landau. *On the Theory of Phase Transitions*. *Zh. Eksp. Teor. Fiz.* 7 (1937), pp. 19–32.

[Lau83] R. B. Laughlin. *Anomalous quantum Hall effect: An incompressible quantum fluid with fractionally charged excitations*. *Physical Review Letters* 50.18 (1983), pp. 1395–1398.

[Lau00] R. B. Laughlin, D. Pines, J. Schmalian, B. P. Stojković, and P. Wolynes. *The middle way*. *Proceedings of the National Academy of Sciences of the United States of America* 97.1 (2000), pp. 32–37.

[Lee89] D.-H. Lee and M. P. A. Fisher. *Anyon superconductivity and the fractional quantum Hall effect*. *Phys. Rev. Lett.* 63 (8 1989), pp. 903–906.

[Lee09] M. Lee, W. Kang, Y. Onose, Y. Tokura, and N. P. Ong. *Unusual Hall Effect Anomaly in MnSi under Pressure*. *Physical Review Letters* 102.18 (2009).

[Léo23] J. Léonard, S. Kim, J. Kwan, P. Segura, F. Grusdt, C. Repellin, N. Goldman, and M. Greiner. *Realization of a fractional quantum Hall state with ultracold atoms*. *Nature* 619.7970 (2023), pp. 495–499.

[Lin09] Y.-J. Lin, R. L. Compton, K. Jiménez-García, J. V. Porto, and I. B. Spielman. *Synthetic magnetic fields for ultracold neutral atoms*. *Nature* 462.7273 (2009), pp. 628–632.

[Lin11] Y.-J. Lin, K. Jiménez-García, and I. B. Spielman. *Spin–orbit-coupled Bose–Einstein condensates*. *Nature* 471.7336 (2011), pp. 83–86.

[Llo96] S. Lloyd. *Universal Quantum Simulators*. *Science* 273.5278 (1996), pp. 1073–1078.

[Lu16] L. Lu, J. D. Joannopoulos, and M. Soljačić. *Topological states in photonic systems*. *Nature Physics* 12.7 (2016), pp. 626–629.

[Lun24] P. Lunt, P. Hill, J. Reiter, P. M. Preiss, M. Gałka, and S. Jochim. *Realization of a Laughlin state of two rapidly rotating fermions*. 2024.

[Ma24] K. K. Ma, M. R. Peterson, V. Scarola, and K. Yang. *Fractional quantum Hall effect at the filling factor $\nu = 5/2$*. In: *Encyclopedia of Condensed Matter Physics*. Elsevier, 2024, pp. 324–365. ISBN: 9780323914086.

[Mac94] A. H. MacDonald. *Introduction to the Physics of the Quantum Hall Regime*. 1994.

[Mac85] A. H. MacDonald and D. B. Murray. *Droplet wave functions for the fractional quantum Hall effect*. *Phys. Rev. B* 32 (4 1985), pp. 2707–2710.

[Mad00] K. W. Madison, F. Chevy, W. Wohlleben, and J. Dalibard. *Vortex Formation in a Stirred Bose-Einstein Condensate*. *Phys. Rev. Lett.* 84 (5 2000), pp. 806–809.

[Mam20] M. Mamaev, J. H. Thywissen, and A. M. Rey. *Quantum Computation Toolbox for Decoherence-Free Qubits Using Multi-Band Alkali Atoms*. *Advanced Quantum Technologies* 3.11 (2020).

[Man15] M. Mancini et al. *Observation of chiral edge states with neutral fermions in synthetic Hall ribbons*. *Science* 349.6255 (2015), pp. 1510–1513.

[McI19] J. W. McIver, B. Schulte, F.-U. Stein, T. Matsuyama, G. Jotzu, G. Meier, and A. Cavalleri. *Light-induced anomalous Hall effect in graphene*. *Nature Physics* 16.1 (2019), pp. 38–41.

[Miy13] H. Miyake, G. A. Siviloglou, C. J. Kennedy, W. C. Burton, and W. Ketterle. *Realizing the Harper Hamiltonian with Laser-Assisted Tunneling in Optical Lattices*. *Phys. Rev. Lett.* 111 (18 2013), p. 185302.

[Möl07] G. Möller and N. R. Cooper. *Density Waves and Supersolidity in Rapidly Rotating Atomic Fermi Gases*. *Phys. Rev. Lett.* 99 (19 2007), p. 190409.

[Mor86] R. Morf and B. I. Halperin. *Monte Carlo evaluation of trial wave functions for the fractional quantized Hall effect: Disk geometry*. *Phys. Rev. B* 33 (4 1986), pp. 2221–2246.

[Muk22] B. Mukherjee, A. Shaffer, P. B. Patel, Z. Yan, C. C. Wilson, V. Crépel, R. J. Fletcher, and M. Zwierlein. *Crystallization of bosonic quantum Hall states in a rotating quantum gas*. *Nature* 601.7891 (2022), pp. 58–62.

[Muk17] B. Mukherjee, Z. Yan, P. B. Patel, Z. Hadzibabic, T. Yefsah, J. Struck, and M. W. Zwierlein. *Homogeneous Atomic Fermi Gases*. *Physical Review Letters* 118.12 (2017).

[Nak20] J. Nakamura, S. Liang, G. C. Gardner, and M. J. Manfra. *Direct observation of anyonic braiding statistics*. *Nature Physics* 16.9 (2020), pp. 931–936.

[Nav21] N. Navon, R. P. Smith, and Z. Hadzibabic. *Quantum gases in optical boxes*. *Nature Physics* 17.12 (2021), pp. 1334–1341.

[OHa02] K. M. O'Hara, S. L. Hemmer, M. E. Gehm, S. R. Granade, and J. E. Thomas. *Observation of a Strongly Interacting Degenerate Fermi Gas of Atoms*. *Science* 298.5601 (2002), pp. 2179–2182.

[Ols98] M. Olshanii. *Atomic Scattering in the Presence of an External Confinement and a Gas of Impenetrable Bosons*. *Phys. Rev. Lett.* 81 (5 1998), pp. 938–941.

[Pal20] L. Palm, F. Grusdt, and P. M. Preiss. *Skyrmion ground states of rapidly rotating few-fermion systems*. *New Journal of Physics* 22.8 (2020), p. 083037.

[Pal18] L. Palm. *Exploring fractional quantum hall physics using ultracold fermions in rotating traps* . Master Thesis. University of Heidelberg, 2018.

[Pap22] Z. Papic and A. C. Balram. *Fractional quantum Hall effect in semiconductor systems*. 2022.

[Par01] B. Paredes, P. Fedichev, J. I. Cirac, and P. Zoller. $\frac{1}{2}$*-Anyons in Small Atomic Bose-Einstein Condensates*. *Phys. Rev. Lett.* 87 (1 2001), p. 010402.

[Pin97] P. W. H. Pinkse, A. Mosk, M. Weidemüller, M. W. Reynolds, T. W. Hijmans, and J. T. M. Walraven. *Adiabatically Changing the Phase-Space Density of a Trapped Bose Gas*. *Phys. Rev. Lett.* 78 (6 1997), pp. 990–993.

[Pit16] L. Pitaevskii and S. Stringari. *Bose-Einstein Condensation and Superfluidity*. Oxford University Press, 2016. ISBN: 9780198758884.

[Pop04] M. Popp, B. Paredes, and J. I. Cirac. *Adiabatic path to fractional quantum Hall states of a few bosonic atoms*. *Phys. Rev. A* 70 (5 2004), p. 053612.

[Qi11] X.-L. Qi and S.-C. Zhang. *Topological insulators and superconductors*. *Rev. Mod. Phys.* 83 (4 2011), pp. 1057–1110.

[Rea03] N. Read and N. R. Cooper. *Free expansion of lowest-Landau-level states of trapped atoms: A wave-function microscope*. *Physical Review A - Atomic, Molecular, and Optical Physics* 68.3 (2003), p. 4.

[Reg04] C. A. Regal, M. Greiner, and D. S. Jin. *Observation of Resonance Condensation of Fermionic Atom Pairs*. *Physical Review Letters* 92.4 (2004), p. 4.

[Reg03] N. Regnault and T. Jolicoeur. *Quantum Hall Fractions in Rotating Bose-Einstein Condensates*. *Phys. Rev. Lett.* 91 (3 2003), p. 030402.

[Rei23] J. Reiter. *Collective excitations in a mesoscopic Fermi system*. Master Thesis. University of Heidelberg, 2023.

[Rep17] C. Repellin, T. Yefsah, and A. Sterdyniak. *Creating a bosonic fractional quantum Hall state by pairing fermions*. *Phys. Rev. B* 96 (16 2017), p. 161111.

[Rie10] S. Riedl, E. R. S. Guajardo, C. Kohstall, J. H. Denschlag, and R. Grimm. *Superfluid Quenching of the Moment of Inertia in a Strongly Interacting Fermi Gas*. 2010.

[Sac08] S. Sachdev. *Quantum magnetism and criticality*. *Nature Physics* 4.3 (2008), pp. 173–185.

[Sac11] S. Sachdev. *Quantum Phase Transitions*. 2nd ed. Cambridge: Cambridge University Press, 2011, pp. 1–501. ISBN: 9780511973765.

[Sch04] V. Schweikhard, I. Coddington, P. Engels, V. P. Mogendorff, and E. A. Cornell. *Rapidly Rotating Bose-Einstein Condensates in and near the Lowest Landau Level*. *Phys. Rev. Lett.* 92 (4 2004), p. 040404.

[Sch83] J. Schwider, R. Burow, K.-E. Elssner, J. Grzanna, R. Spolaczyk, and K. Merkel. *Digital wave-front measuring interferometry: some systematic error sources*. *Appl. Opt.* 22.21 (1983), pp. 3421–3432.

[Ser20] M. Serlin, C. L. Tschirhart, H. Polshyn, Y. Zhang, J. Zhu, K. Watanabe, T. Taniguchi, L. Balents, and A. F. Young. *Intrinsic quantized anomalous Hall effect in a moiré heterostructure*. *Science* 367.6480 (2020), pp. 900–903.

[Ser11a] F. Serwane, G. Zürn, T. Lompe, T. B. Ottenstein, A. N. Wenz, and S. Jochim. *Deterministic preparation of a tunable few-fermion system*. *Science* 332.6027 (2011), pp. 336–338.

[Ser11b] F. Serwane. *Deterministic preparation of a tunable few-fermion system*. PhD thesis. University of Heidelberg, 2011.

[Sim07] S. H. Simon, E. H. Rezayi, and N. R. Cooper. *Pseudopotentials for multiparticle interactions in the quantum Hall regime*. *Phys. Rev. B* 75 (19 2007), p. 195306.

[Sin02] J. Sinova, C. B. Hanna, and A. H. MacDonald. *Quantum Melting and Absence of Bose-Einstein Condensation in Two-Dimensional Vortex Matter*. *Phys. Rev. Lett.* 89 (3 2002), p. 030403.

[Sta98] D. M. Stamper-Kurn, H.-J. Miesner, A. P. Chikkatur, S. Inouye, J. Stenger, and W. Ketterle. *Reversible Formation of a Bose-Einstein Condensate*. *Physical Review Letters* 81.11 (1998), pp. 2194–2197.

[Ste23] D. Steck. *Alkali D Line* (2023).

[Ste08] A. Stern. *Anyons and the quantum Hall effect—A pedagogical review*. *Annals of Physics* 323.1 (2008), pp. 204–249.

[Sto92] H. Stormer. *Two-dimensional electron correlation in high magnetic fields*. *Physica B: Condensed Matter* 177.1 (1992), pp. 401–408.

[Str18] G. C. Strinati, P. Pieri, G. Röpke, P. Schuck, and M. Urban. *The BCS–BEC crossover: From ultra-cold Fermi gases to nuclear systems*. *Physics Reports* 738 (2018), pp. 1–76.

[Str12] J. Struck, C. Ölschläger, M. Weinberg, P. Hauke, J. Simonet, A. Eckardt, M. Lewenstein, K. Sengstock, and P. Windpassinger. *Tunable Gauge Potential for Neutral and Spinless Particles in Driven Optical Lattices*. *Phys. Rev. Lett.* 108 (22 2012), p. 225304.

[Stu15] B. K. Stuhl, H.-I. Lu, L. M. Aycock, D. Genkina, and I. B. Spielman. *Visualizing edge states with an atomic Bose gas in the quantum Hall regime*. *Science* 349.6255 (2015), pp. 1514–1518.

[Sue92] Y. W. Suen, L. W. Engel, M. B. Santos, M. Shayegan, and D. C. Tsui. *Observation of a $\nu=1/2$ fractional quantum Hall state in a double-layer electron system*. *Phys. Rev. Lett.* 68 (9 1992), pp. 1379–1382.

[Tai17] M. E. Tai, A. Lukin, M. Rispoli, R. Schittko, T. Menke, D. Borgnia, P. M. Preiss, F. Grusdt, A. M. Kaufman, and M. Greiner. *Microscopy of the interacting Harper–Hofstadter model in the two-body limit*. *Nature* 546.7659 (2017), pp. 519–523.

[Tal06] A. Talmi and E. N. Ribak. *Wavefront reconstruction from its gradients*. *J. Opt. Soc. Am. A* 23.2 (2006), pp. 288–297.

[Tan19] F. Tang et al. *Three-dimensional quantum Hall effect and metal–insulator transition in ZrTe5*. *Nature* 569.7757 (2019), pp. 537–541.

[Tey13] M. K. Tey, L. A. Sidorenkov, E. R. S. Guajardo, R. Grimm, M. J. H. Ku, M. W. Zwierlein, Y.-H. Hou, L. Pitaevskii, and S. Stringari. *Collective Modes in a Unitary Fermi Gas across the Superfluid Phase Transition*. *Phys. Rev. Lett.* 110 (5 2013), p. 055303.

[Tho82] D. J. Thouless, M. Kohmoto, M. P. Nightingale, and M. den Nijs. *Quantized Hall Conductance in a Two-Dimensional Periodic Potential*. *Phys. Rev. Lett.* 49 (6 1982), pp. 405–408.

[Tie10] T. G. Tiecke. *Properties of Potassium* (2010).

[Til19] D. R. Tilley. *Superfluidity and superconductivity*. Routledge, 2019.

[Tom18] E. M. Tommaso Comparin. *tcompa/Laughlin-Metropolis: Laughlin-Metropolis*. 2018.

[Ton16] D. Tong. *Lectures on the Quantum Hall Effect*. 2016.

[Tsu82] D. C. Tsui, H. L. Stormer, and A. C. Gossard. *Two-dimensional magnetotransport in the extreme quantum limit*. *Physical Review Letters* 48.22 (1982), pp. 1559–1562.

[Tsu24] Y.-C. Tsui, M. He, Y. Hu, E. Lake, T. Wang, K. Watanabe, T. Taniguchi, M. P. Zaletel, and A. Yazdani. *Direct observation of a magnetic-field-induced Wigner crystal*. *Nature* 628.8007 (2024), pp. 287–292.

[Umu18] R. O. Umucal ılar, E. Macaluso, T. Comparin, and I. Carusotto. *Time-of-Flight Measurements as a Possible Method to Observe Anyonic Statistics*. *Phys. Rev. Lett.* 120 (23 2018), p. 230403.

[Val21] C. J. Vale and M. Zwierlein. *Spectroscopic probes of quantum gases*. *Nature Physics* 17.12 (2021), pp. 1305–1315.

[Vie22] C. Viermann et al. *Quantum field simulator for dynamics in curved spacetime*. *Nature* 611.7935 (2022), pp. 260–264.

[Wan24] C. Wang et al. *Realization of fractional quantum Hall state with interacting photons*. 2024.

[Wei21] C. Weitenberg and J. Simonet. *Tailoring quantum gases by Floquet engineering*. *Nature Physics* 17.12 (2021), pp. 1342–1348.

[Wen04] X.-G. Wen. *Quantum Field Theory of Many-Body Systems: From the Origin of Sound to an Origin of Light and Electrons*. Oxford: Oxford University Press, 2004.

[Wen95] X.-G. Wen. *Topological orders and edge excitations in fractional quantum Hall states*. *Advances in Physics* 44.5 (1995), pp. 405–473.

[Wen07] X.-G. Wen. *Quantum Field Theory of Many-Body Systems*. New York: Oxford University Press, 2007. ISBN: 9780199227259.

[Wig34] E. Wigner. *On the Interaction of Electrons in Metals*. *Physical Review* 46.11 (1934), pp. 1002–1011.

[Wil82] F. Wilczek. *Quantum Mechanics of Fractional-Spin Particles*. *Phys. Rev. Lett.* 49 (14 1982), pp. 957–959.

[Wil00] N. K. Wilkin and J. M. F. Gunn. *Condensation of Composite Bosons in a Rotating BEC*. *Phys. Rev. Lett.* 84 (1 2000), pp. 6–9.

[Wil98] N. K. Wilkin, J. M. F. Gunn, and R. A. Smith. *Do Attractive Bosons Condense?* *Phys. Rev. Lett.* 80 (11 1998), pp. 2265–2268.

[Win20] K. Wintersperger, C. Braun, F. N. Ünal, A. Eckardt, M. D. Liberto, N. Goldman, I. Bloch, and M. Aidelsburger. *Realization of an anomalous Floquet topological system with ultracold atoms*. *Nature Physics* 16.10 (2020), pp. 1058–1063.

[Wu75] T. T. Wu and C. N. Yang. *Concept of nonintegrable phase factors and global formulation of gauge fields*. *Phys. Rev. D* 12 (12 1975), pp. 3845–3857.

[Yan24] Z. Yan, P. B. Patel, B. Mukherjee, C. J. Vale, R. J. Fletcher, and M. W. Zwierlein. *Thermography of the superfluid transition in a strongly interacting Fermi gas*. *Science* 383.6683 (2024), pp. 629–633.

[Yan08] K. Yang and H. Zhai. *Quantum Hall Transition near a Fermion Feshbach Resonance in a Rotating Trap*. *Phys. Rev. Lett.* 100 (3 2008), p. 030404.

[Yao23] R. Yao, S. Chi, B. Mukherjee, A. Shaffer, M. Zwierlein, and R. J. Fletcher. *Observation of chiral edge transport in a rapidly-rotating quantum gas*. 2023.

[Yos98] D. Yoshioka. *The Quantum Hall Effect*. New York: Iwanami Shoten, Publishers, Tokyo 1998, 1998. ISBN: 978-3-642-07720-3.

[Yu10] R. Yu, W. Zhang, H.-J. Zhang, S.-C. Zhang, X. Dai, and Z. Fang. *Quantized Anomalous Hall Effect in Magnetic Topological Insulators*. *Science* 329.5987 (2010), pp. 61–64.

[Zho23] T.-W. Zhou et al. *Observation of universal Hall response in strongly interacting Fermions*. *Science* 381.6656 (2023), pp. 427–430.

[Zür12a] G. Zürn, T. Lompe, A. N. Wenz, S. Jochim, P. S. Julienne, and J. M. Hutson. *Precise characterization of ^{6}Li Feshbach resonances using trap-sideband resolved RF spectroscopy of weakly bound molecules*. *Physical Review Letters* 110.13 (2012), p. 135301.

[Zür12b] G. Zürn, F. Serwane, T. Lompe, A. N. Wenz, M. G. Ries, J. E. Bohn, and S. Jochim. *Fermionization of Two Distinguishable Fermions*. *Physical Review Letters* 108.7 (2012), p. 075303.

[Zür13] G. Zürn, A. N. Wenz, S. Murmann, A. Bergschneider, T. Lompe, and S. Jochim. *Pairing in Few-Fermion Systems with Attractive Interactions*. *Physical Review Letters* 111.17 (2013), p. 175302.

[Zwi05] M. W. Zwierlein, J. R. Abo-Shaeer, A. Schirotzek, C. H. Schunck, and W. Ketterle. *Vortices and superfluidity in a strongly interacting Fermi gas*. *Nature* 435.7045 (2005), pp. 1047–1051.

[Zwi03] M. W. Zwierlein, C. A. Stan, C. H. Schunck, S. M. F. Raupach, S. Gupta, Z. Hadzibabic, and W. Ketterle. *Observation of Bose-Einstein Condensation of Molecules*. *Physical Review Letters* 91.25 (2003), p. 250401.

[Zwi04] M. W. Zwierlein, C. A. Stan, C. H. Schunck, S. M. Raupach, A. J. Kerman, and W. Ketterle. *Condensation of pairs of fermionic atoms near a Feshbach resonance*. *Physical Review Letters* 92.12 (2004).